ABSTRACT

$^{14}N(P,P')$ AT 29.8, 36.6, AND 40.0 MEV
AND THE STRENGTH OF THE TENSOR FORCE
IN NUCLEAR REACTIONS

By

Stanley Haim Fox

Measurements of the angular distribution of the $^{14}N(p,p')^{14}N^*$ (2.31 MeV), $(1^+;0) \longrightarrow (0^+;1)$, reaction were made at higher energies (29.8, 36.6, and 40.0 MeV) and with better precision than before and information about the strength of the tensor force in nuclear reactions was extracted.

Protons from the MSU Sector-Focused Cyclotron were scattered from gas and evaporated melamine ^{14}N targets and detected either with lithium drifted silicon detectors in a 40" scattering chamber or with position sensitive detectors in an Enge split-pole spectrograph. Angular distributions for elastic scattering and the excitation of

the 2.31 ($0^+;1$) and 3.94 ($1^+;0$) MeV states were obtained at all the energies. In addition, the angular distributions for the excitation of the ten known states in ^{14}N between 4.91 and 8.49 MeV were obtained for 29.8 MeV incident protons.

Optical model fits to elastic data between 24.8 and 40.0 MeV were obtained using an average set of optical model geometry parameters. Microscopic model DWBA calculations with exchange were made for the 2.31 MeV reaction including central, L·S, and (most importantly) tensor forces in the two body interaction. The interaction that best fit the shape of the inelastic scattering to the 2.31 MeV state at 24.8, 29.8, 36.6, and 40.0 MeV was a Serber central force plus the Hamada-Johnston spin-orbit potential and OPEP with a 25% increase in strength. Results for microscopic model DWBA calculations with exchange are also reported for the reactions to the 3.94 ($1^+;0$) and 7.03 ($2^+;0$) MeV states.

$^{14}N(P,P')$ AT 29.8, 36.6, AND 40.0 MEV AND THE STRENGTH OF THE TENSOR FORCE IN NUCLEAR REACTIONS

By

Stanley Haim Fox

A THESIS

Submitted to
Michigan State University
in partial fulfillment of the requirements
for the degree of

DOCTOR OF PHILOSOPHY

Department of Physics

1972

Urlicht (Primal Light)

from Das Knaben Wunderhorn
as quoted by Gustav Mahler in Symphony #2
"Ressurrection"

O Röschen roth
Der Mensch liegt in grösster Noth!
Der Mensch liegt in grösster Pein!
Lieger möcht' ich Himmel sein.
Da kam ich auf einem breiten Weg;
Da kam ein Engelein und wollt' mich abweisen;
Ach nein! Ich liess mich nicht abweisen.
Ich bin von Gott und will wieder zu Gott!
Der liebe Gott wird mir ein Lichtchen geben,
Wird leuchten mir bis in das ewig selig Leben!

O Rosebud red
Here man lies in greatest need!
Here man lies in greatest woe!
If only I could to heaven go.
Then came I upon a broad fair way;
There came an angel and he would reject me;
Ah no, I would not be rejected.
I am of God and will home, back to God!
Beloved God a candle light will lend me,
And onward to eternal blissful life will send me!

ACKNOWLEDGMENTS

There are a number of people without whose help this work would never have been completed. First of all there is Dr. Sam M. Austin who formulated the problem and who always seemed to have useful suggestions. I would like to thank Dr. Duane Larson who helped me take the data and whose understanding of proton inelastic scattering was crucial. I am greatly in debt to all the staff members of the Cyclotron Laboratory, but especially to Norvel Mercer and his shop staff and to Richard Au and the keepers of the E-7. Bob Matson was very helpful in preparing the many graphs in this work. I am also thankful for the good humor of my other friends in room 161, Dr. Lolo M. Panggabean and Dr. Helmut Laumer.

The one to whom I am most indebted is my wife, Janet.

TABLE OF CONTENTS

LIST OF TABLES		viii
LIST OF FIGURES		xi
1.	INTRODUCTION	1
2.	EXPERIMENTAL	2
	2.1 General Discussion	2
	2.1.1 Experimental Layout	2
	2.1.2 Proton Beam Energy	2
	2.1.3 Beam Alignment	8
	2.1.4 Beam Current	8
	2.2 Measurements Made with Gas Targets	10
	2.2.1 Gas Target Construction	10
	2.2.2 Gas Cell Diameter and Scattering Angle Range	10
	2.2.3 Effective Target Thickness	13
	2.2.4 Gas Pressure Measurements	14
	2.2.5 Gas Temperature Measurements	14
	2.2.6 Scattered Particle Collimation Units	15
	2.2.7 Angular Measurements	19
	2.2.8 Beam Current Measurements	19
	2.2.9 E/ΔE Detector Telescope	20
	2.2.10 E/ΔE Signal Processing	22
	2.2.11 Monitor Detector	22

2.2.12 Degrader-Detector Combination for 36.6 and 40.0 Absolute Normalization Measurements 26

2.3 Measurements Made with the Enge Split-Pole Spectrograph 27

2.3.1 The Spectrograph vs. the Scattering Chamber 27

2.3.2 Melamine Targets 30

2.3.3 Target Spinner 32

2.3.4 Silicon, Surface Barrier, Position Sensitive Detector 34

2.3.5 Particle Identification 34

2.3.6 Signal Processing Electronics 35

2.3.7 Computer Data Handling 35

2.3.8 Monitor Detector 36

3. DATA 40

3.1 General Description of the Data 40

3.2 Reduction of the Gas Target Data 42

3.2.1 2.31 MeV State Data; Gas Target Data 42

3.2.2 Inelastic Gas Target Data Other than the 2.31 MeV State Data 43

3.2.3 A Test of SAMPO 45

3.2.4 Reactions in the Detector and the 6.44 MeV State Angular Distribution 47

3.2.5 Normalization of the Gas Target Data 48

3.3 Reduction of the Position-Sensitive Detector Data 49
3.3.1 Description of Difficulties 49
3.3.2 Background Subtraction 50
3.3.3 Point to Point Normalization 51
3.3.4 Absolute Normalization 51
3.4 Summary of Error Determination 52
3.4.1 29.8 MeV Gas Cell Data 52
3.4.2 Position-Sensitive Detector Data 53
3.5 Plots and Tables of the Angular Distributions 53
4. OPTICAL MODEL ANALYSIS 96
4.1 Purpose 96
4.2 Elastic Scattering Data 97
4.3 Optical Model Searches 98
4.4 Spin-Orbit Form Factor 102
4.5 Variation of Well Strengths with Energy 114
5. MICROSCOPIC MODEL CALCULATIONS 117
5.1 D.W.B.A 70A 117
5.2 Wave Functions 118
5.2.1 ^{1}P Shell Wave Functions 119
5.2.2 ^{12}C Core Plus sd Shell Wave Functions 122
5.3 Coupled Channels Calculations 123
5.4 Two-Step Processes 124
5.5 Nuclear Forces 125
5.5.1 Fitting Central Interactions to the

		Yukawa Radial Form	125
	5.5.2	Serber Central Potential (S)	126
	5.5.3	Even State Hamada-Johnston Central Potential (HJ)	126
	5.5.4	Even State Hamada-Johnston Central Potential Plus ^{1}P State Gaussian Potential (HJ-G)	126
	5.5.5	Blatt-Jackson Central Potential (BJ)	128
	5.5.6	Average Effective Central Potential (SMA)	128
	5.5.8	Spin-Orbit Potential	130
	5.5.9	"Complete" Hamada-Johnston Force	131
	5.5.10	Central Potential for Inelastic Scattering to States Other than the 2.31 MeV State	133
6.	RESULTS		134
	6.1	Results For Calculations of Inelastic Scattering to the 2.31 MeV State	134
	6.2	Results for Calculations of Inelastic Scattering to States Other than the 2.31 MeV State	153
7.	CONCLUSION		158
8.	SUMMARY		162
	LIST OF REFERENCES		163
	APPENDIX 1		167
	APPENDIX 2		170

LIST OF TABLES

Table		Page
1.	Collimation units' dimensions, forward angle limits, and G-factors.	11
2.	Dimensions of spectrograph apertures.	29
3.	$^{14}N(p,p)^{14}N$ elastic scattering, E_p = 29.8 MeV.	73
4.	$^{14}N(p,p')^{14}N^*$ (2.31,(0^+;1)), E_p = 29.8 MeV.	74
5.	$^{14}N(p,p')^{14}N^*$ (3.94,(1^+;0)), E_p = 29.8 MeV.	75
6.	$^{14}N(p,p')^{14}N^*$ (4.91,(0^-;0)), E_p = 29.8 MeV.	76
7.	$^{14}N(p,p')^{14}N^*$ (5.11,(2^-;0)), E_p = 29.8 MeV.	77
8.	$^{14}N(p,p')^{14}N^*$ (5.69,(1^-;0)), E_p = 29.8 MeV.	78
9.	$^{14}N(p,p')^{14}N^*$ (5.83,(3^-;0)), E_p = 29.8 MeV.	79
10.	$^{14}N(p,p')^{14}N^*$ (6.20,(1^+;0)), E_p = 29.8 MeV.	80
11.	$^{14}N(p,p')^{14}N^*$ (6.44,(3^+;0)), E_p = 29.8 MeV.	81
12.	$^{14}N(p,p')^{14}N^*$ (7.03,(2^+;0)), E_p = 29.8 MeV.	82
13.	$^{14}N(p,p')^{14}N^*$ (7.97,(2^-;0)), E_p = 29.8 MeV.	83

Table		Page
14.	$^{14}N(p,p')^{14}N^*(8.06,(1^-;1))$, E_p = 29.8 MeV.	84
15.	$^{14}N(p,p')^{14}N^*(8.49,(4^-;0))$, E_p = 29.8 MeV.	85
16.	$^{14}N(p,p)^{14}N$ elastic scattering for E_p = 36.6 MeV	86
17.	$^{14}N(p,p')^{14}N^*(2.31,(0^+;1))$, E_p = 36.6 MeV.	87
18.	$^{14}N(p,p')^{14}N^*(3.94,(1^+;0))$, E_p = 36.6 MeV.	88
19.	$^{14}N(p,p)^{14}N$ elastic scattering for E_p = 40.0 MeV.	89
20.	$^{14}N(p,p')^{14}N^*(2.31,(0^+;1))$, E_p = 40.0 MeV.	90
21.	$^{14}N(p,p')^{14}N^*(3.94,(1^+;0))$, E_p = 40.0 MeV.	91
22.	$^{14}N(p,p')^{14}N^*$(2.31 MeV) plotted against momentum transfer for E_p = 24.8 MeV (Cr 70).	92
23.	$^{14}N(p,p')^{14}N^*$(2.31 MeV) plotted against momentum transfer for E_p = 29.8 MeV.	93
24.	$^{14}N(p,p')^{14}N^*$ (2.31 MeV) plotted against momentum transfer for E_p = 36.6 MeV.	94
25.	$^{14}N(p,p')^{14}N^*$(2.31 MeV) plotted against momentum transfer for E_p = 40.0 MeV.	95
26.	$^{14}N(p,p)^{14}N$ elastic scattering for E_p = 24.8 and 29.8 MeV with the errors used	

Table		Page
	during optical model searches.	99
27.	$^{14}N(p,p)^{14}N$ elastic scattering for E_p = 36.6 and 40.0 MeV with the errors used during optical model searches.	100
28.	^{14}N optical model parameters found in this work	103
29.	^{14}N optical model parameters from Watson et al. (Wa 69)	109
30.	^{14}N optical model results for free spin-orbit geometry parameters.	112
31.	^{14}N wave functions.	120
32.	Central and tensor forces.	127
33.	Values of the spin-orbit force.	132
34.	Comparison of central forces.	138
35.	Calculation normalization factors	152
36.	Values of the tensor force.	159

LIST OF FIGURES

Figure		Page
1.	Layout of the cyclotron experimental area as of August, 1972	7
2.	Energy levels of ^{14}N up to 8.62 MeV.	9
3.	Definition of the line source target in a gas cell by the collimator's slits.	12
4.	A schematic drawing of one of the collimating units.	17
5.	Two detector telescope summing circuit.	21
6.	Signal processing electronics.	23
7.	Two dimensional TOOTSIE display.	24
8.	A proton spectrum taken with the E/ΔE detector package and gas target.	25
9.	Kinematic compensation in the split-pole spectrograph.	31
10.	A schematic drawing of the target spinner.	33

Figure		Page
11.	Spectrum taken in the spectrograph.	37
12.	40.0 MeV monitor spectrum from an evaporated melamine target. The detector angle is 150^{o}.	38
13.	Pseudo spectra of the type used to test SAMPO. Arrows indicate centroids as assigned by SAMPO.	46
14.	$^{14}N(p,p)^{14}N$ angular distribution for E_p = 29.8 MeV.	54
15.	$^{14}N(p,p')^{14}N^*$ (2.31 MeV,$(0^+;1)$) angular distribution for E_p = 29.8 MeV.	55
16.	$^{14}N(p,p')^{14}N^*$ (3.94 MeV,$(1^+;0)$) angular distribution for E_p = 29.8 MeV.	56
17.	$^{14}N(p,p')^{14}N^*$ (4.91 MeV,$(0^-;0)$) angular distribution for E_p = 29.8 MeV.	57
18.	$^{14}N(p,p')^{14}N^*$ (5.11 MeV,$(2^-;0)$) angular distribution for E_p = 29.8 MeV.	58
19.	$^{14}N(p,p')^{14}N^*$ (5.69 MeV,$(1^-;0)$) angular distribution for E_p = 29.8 MeV.	59
20.	$^{14}N(p,p')^{14}N^*$ (5.83 MeV,$(3^-;0)$) angular distribution for E_p = 29.8 MeV.	60

Figure		Page
21	$^{14}N(p,p')^{14}N^*$ (6.20 MeV, $(1^+;0)$) angular distribution for E_p = 29.8 MeV.	61
22.	$^{14}N(p,p')^{14}N^*$ (6.44 MeV, $(3^+;0)$) angular distribution for E_p = 29.8 MeV.	62
23.	$^{14}N(p,p')^{14}N^*$ (7.02 MeV, $(2^+;0)$) angular distribution for E_p = 29.8 MeV.	63
24.	$^{14}N(p,p')^{14}N^*$ (7.97 MeV, $(2^-;0)$) angular distribution for E_p = 29.8 MeV.	64
25.	$^{14}N(p,p')^{14}N^*$ (8.06 MeV, $(1^-;1)$) angular distribution for E_p = 29.8 MeV	65
26.	$^{14}N(p,p')^{14}N^*$ (8.49 MeV, $(4^-;0)$) angular distribution for E_p = 29.8 MeV.	66
27.	$^{14}N(p,p)^{14}N$ angular distribution for E_p = 36.6 MeV.	67
28.	$^{14}N(p,p')^{14}N^*$ (2.31 MeV, $(0^+;1)$) angular distribution for E_p = 36.6 MeV.	68
29.	$^{14}N(p,p')^{14}N^*$ (3.94 MeV, $(1^+;0)$) angular distribution for E_p = 36.6 MeV.	69
30.	$^{14}N(p,p')^{14}N$ angular distribution for E_p = 40.0 MeV.	70
31.	$^{14}N(p,p')^{14}N^*$ (2.31 MeV, $(0^+;1)$) angular distribution for E_p = 40.0 MeV.	71

Figure		Page
32.	$^{14}N(p,p')^{14}N^*$ (3.94 MeV, $(1^+;0)$) angular distribution for E_p = 40.0 MeV.	72
33.	The differential cross sections for the $^{14}N(p,p')^{14}N^*$ (2.31 MeV) reaction analyzed in this work plotted against momentum transfer.	72a
34.	Optical model fits to the 24.8 MeV and 29.8 MeV ^{14}N elastic scattering for the optical model potential determined by this work with $r_{SO} = r_R$ and $a_{SO} = a_R$.	104
35.	Optical model fits to the 36.6 and 40.0 MeV ^{14}N elastic scattering for the optical model of this work with $r_{SO} = r_R$ and $a_{SO} = a_R$.	105
36.	Radial dependence of the Thomas form of the spin-orbit potential and of the Thomas form as modified by Watson et al. (Wa 69) for A = 14.	107
37.	Optical model fits to the 24.8 and 29.8 MeV ^{14}N elastic scattering for the geometry and parameters from the work of Watson et al. (Wa 69).	110
38.	Optical model fits to the 36.6 and 40.0 MeV ^{14}N elastic scattering for the geometry and parameters from the work of Watson et al. (Wa 69).	111

Figure		Page
39.	Optical model fits to the 24.8 and 29.8 MeV ^{14}N elastic scattering. The spin-orbit potential has the Thomas form with parameters varied to best fit the data.	113
40.	Variation of the strengths of the optical model potential found in this work as a function of energy.	115
41.	$^{14}N(p,p')^{14}N^*$ (2.31 MeV) calculations with OPEP alone.	135
42.	$^{14}N(p,p')^{14}N^*$ (2.31 MeV) calculations with: OPEP and HJ-T alone at 40.0 MeV (A); V-F and C-K wave functions with S + OPEP at 29.8 MeV (B); and optical model parameters of Cr 70 and this work with S + OPEP at 29.8 MeV (C) and 40.0 MeV (D).	137
43.	$^{14}N(p,p')^{14}N^*$ (2.31 MeV) calculations for HJ central plus HJ-T.	140
44.	$^{14}N(p,p')^{14}N^*$ (2.31 MeV) calculations for HJ-G central plus HJ-T.	141
45.	$^{14}N(p,p')^{14}N^*$ (2.31 MeV) calculations for BJ central plus OPEP.	142
46.	$^{14}N(p,p')^{14}N^*$ (2.31 MeV) calculations for SMA central plus OPEP.	144

Figure		Page
47.	$^{14}N(p,p')^{14}N^*$ (2.31 MeV) calculations for S central plus OPEP and S central alone.	145
48.	$^{14}N(p,p')^{14}N^*$ (2.31 MeV) calculations for S central plus HJ-LS and OPEP.	146
49.	$^{14}N(p,p')^{14}N^*$ (2.31 MeV) calculations for the complete Hamada-Johnston potential as put into Yukawa from by Escudie et al. (Es 72).	148
50.	$^{14}N(p,p')^{14}N^*$ (2.31 MeV) calculations for S central plus HJ-LS plus OPEP. Calculations are normalized to best fit the data at forward angles.	149
51.	$^{14}N(p,p')^{14}N^*$ (2.31 MeV) calculations for S central plus HJ-LS and 1.25 X OPEP. Calculations are normalized to best fit the data at forward angles.	150
52.	$^{14}N(p,p')^{14}N^*$ (2.31 MeV) calculations for S central plus HJ-LS and 1.4 X OPEP. Calculations are normalized to best fit the data at forward angles.	151
53.	$^{14}N(p,p')^{14}N^*$ (2.31 MeV) calculations for S central plus HJ-LS and OPEP plotted as a function of momentum transfer. The symbols are for identification only.	154

Figure		Page
54.	$^{14}N(p,p')^{14}N^*$ (3.94 MeV) calculations for S central and C-K wave functions normalized by the experimental to calculated E2 transition ratio.	156
55.	$^{14}N(p,p')^{14}N^*$ (7.03 MeV) calculation for S central and C-K wave functions normalized by the experimental to calculated E2 transition ratio.	157
A1.	Collimation slits defining the line source at 90° in the Lab.	169

1. INTRODUCTION

The inelastic scattering of protons from the 2.31 MeV first excited state in ^{14}N is germane to the study of the nucleon-nucleon interaction in inelastic scattering as well as to aspects of the reaction mechanism itself. Earlier studies of inelastic scattering at 24.9 MeV by Crawley *et al.* (Cr 70) and at 17 MeV by Rogers (Ro 71) and of the analogous reaction ^{14}C (p,n) ^{14}N (Wo 67, Wo 71) at proton energies between 6 and 14 MeV show that for microscopic model analysis, not including the knockout exchange amplitudes, a central interaction alone is not sufficient to explain the experimental data and that including a tensor component in the nuclear force results in greatly improved agreement.

This outcome was not unexpected. In the distorted wave Born approximation (DWBA), neglecting exchange, the cross section for a reaction A (a, b) B is proportional to the square of the transition amplitude.

$T_{ba} = \int \chi_b^{(-)} \langle \Psi_f \mid V_{eff} \mid \Psi_i \rangle \chi_a^{(+)} d\vec{r}$, where $\chi_a^{(+)}$ and $\chi_b^{(-)}$ are the incoming and outgoing distorted waves and Ψ_i and Ψ_f are the initial and final projectile-target states. In the microscopic approach to proton inelastic scattering it is assumed that V_{eff} can be written as the sum of the two-body interactions between the projectile

"p" and the target nucleons "i ". Thus:

$$V_{eff} = \sum V_{ip}$$

the sum being over the valence target nucleons. If only the central part of the nucleon-nucleon force is used V_{ip} can be expressed as:

$$V_{ip}(r) = V_{00}(r) + V_{10}(r)\ \vec{\sigma}_i \cdot \vec{\sigma}_p + V_{01}(r)\ \vec{\tau}_i \cdot \vec{\tau}_p + V_{11}(r)\ (\vec{\sigma}_i \cdot \vec{\sigma}_p)\ (\vec{\tau}_i \cdot \vec{\tau}_p)$$

where the subscripts on the V_{ST} are the spin and isospin transferred in the reaction. The selection rules for the direct (non-exchange) process are (Sa 66):

$$\vec{J} = \vec{J}_f - \vec{J}_i \qquad \vec{T} = \vec{T}_f - \vec{T}_i$$

$$\vec{S} = \vec{S}_i - \vec{S}_f \qquad \pi_i\ \pi_f = (-1)^L$$

$$\vec{L} = \vec{J} - \vec{S}$$

where $\vec{J}$, $\vec{S}$, and $\vec{L}$ are the total angular momentum, spin, and orbital angular momentum transferred in the reaction and $\vec{T}$ is the transferred isospin. For $^{14}N\ (p,p')^{*}$ (2.31 MeV) (J_i, π_i, T_i) are (1, +, 0) and (J_f, π_f, T_f) are (0, +, 1) and for $^{14}C\ (p,n)\ ^{14}N$ we have (0, +, 1) $\longrightarrow$ (1, +, 0). Both of these interactions select out the V_{11} part of the central force and for both, only L = 0 and L = 2 are allowed in the direct process. For $\vec{L} = 0$ and $V = V_{11}$ $(\vec{\sigma}_i \cdot \vec{\sigma}_p)\ (\vec{\tau}_i \cdot \vec{\tau}_p)$ the inelastic scattering matrix element has been shown (Wo 67) to be nearly proportional to that for the Gamow-Teller beta decay of ^{14}C. This decay is found to be strongly inhibited (Ba 66), and so the normally

dominant $\vec{L} = 0$ contribution to the cross sections for the inelastic scattering and charge exchange interactions are also supressed.

The orbital angular momentum selection rules that apply when a tensor term, which is always an $\vec{S} = 1$ term, is added to the central force in a direct calculation are:

$$L = \lambda \quad \text{or} \quad L = \lambda \pm 2$$

where $\vec{L}$ is the orbital angular momentum transferred to the projectile and $\vec{\lambda}$ the orbital angular momentum transferred to the target nucleon. For central forces $\lambda = L$. The $\lambda = 0$ and $L = 0$ amplitude for a tensor force is suppressed just as is the $L = 0$ amplitude for a central force, but the $\lambda = 2$ amplitudes ($L = 0$ and $L = 2$) are not (Wo 71). Inclusion of a tensor force thus allows an $L = 0$ amplitude which turns out to dominate the $L = 2$ amplitude of the central force.

When the microscopic DWBA formalism is modified to include the effect of exchange the selection rules change somewhat with the result that the unnatural parity $L = 1$ transition is allowed for both a central or a central plus tensor effective interaction.

For central forces the selection rules are the same as for the direct amplitudes with the exception that the angular momenta transferred need not satisfy the $\pi_i \ \pi_f = (-1)^L$ condition (Lo 70). In all cases studied to date the amplitudes for these so-called unnatural parity L transfers are small (At 70) for small L transfers. For central

forces that act only in even (Serber forces for example) or odd relative orbital angular momentum states, the same components of the force contribute to the direct and exchange amplitudes. In the limit of zero range even state forces there is constructive interference between the direct and exchange terms. The selection rules that govern the tensor exchange amplitudes are found in reference 48. Here $\Delta \pi$ need be neither $(-1)^L$ or $(-1)^\lambda$, and unnatural $\vec{L}$ transfers are also allowed. Calculations by Love et al. (Lo 70a) ($^{14}N(p,n)^{14}O,(gs)$ the analogue of $^{14}N(p,p')^{14}N^*(2.31\ MeV)$), and Satchler (Lo 70b) (data of Crawley et al.) and Escudie et al. (Es 70) ($^{14}N\ [p,p']\ ^{14}N^*\ [2.31\ MeV]$ at 24 MeV) show that inclusion of exchange does not eliminate the need for inclusion of the tensor force.

In summary, all calculations for the inelastic scattering to the 2.31 MeV state in ^{14}N with central forces produce an L = 2 shape, a rather broad shape, while the observed angular distributions are forward peaked, Direct calculations of $\sigma(\theta)$ at 24.9 MeV which include the tensor force, reproduce this forward peaking see (see Figure (47)).

The major purpose of this project was to measure cross sections for the $^{14}N\ (p,p')\ ^{14}N^*$ (E_x = 2.31 MeV, 0 +, 1) reaction at higher energies (29.8, 36.6, and 40.0 MeV) and with better precision than before, and so to extract information about the tensor force in nuclear reactions. The reason for going to higher energies is to avoid compound

nuclear effects. Even at 24.9 MeV, there is evidence of compound nuclear effects. Extending the energy range at which this inelastic scattering has been measured also allows one to look for energy dependencies in the effective interaction.

There are very few angular distributions available for ^{14}N inelastic scattering to the states above the 3.94 MeV state for proton energies above 15 MeV. For this reason, angular distributions to the first 12 excited states of ^{14}N were measured at 29.8 MeV. At 36.6 MeV and 40.0 MeV the 3.94 MeV angular distribution was measured. These angular distributions were compared with calculations using the microscopic DWBA formalism and available wave functions.

2. EXPERIMENTAL

2.1 General Discussion

2.1.1 Experimental Layout

Figure (1) is a schematic of the beam handling and analyzing system at the M.S.U. Cyclotron Laboratroy where all of the experimental work for this thesis was done. Measurements with bombarding protons of 29.8, 36.6, and 40.0 MeV on melamine targets were made with the Enge split-pole spectrograph while the 29.8 MeV gas target data was taken in a 35 in. diameter scattering chamber located about where the 40 in. scattering chamber is now placed. Normalization measurements for the 36.6 and 40.0 MeV elastic cross sections were made with a gas target in the 40 in. diameter scattering chamber.

2.1.2 Proton Beam Energy

The M.S.U. beam handling and analyzing system has been described by G. H. MacKenzie et al. (Ma 67). In this experiment, the slits at boxes 3 and 5 were 0.10" wide. Thus the energy resolution of the beam was about 1 part in

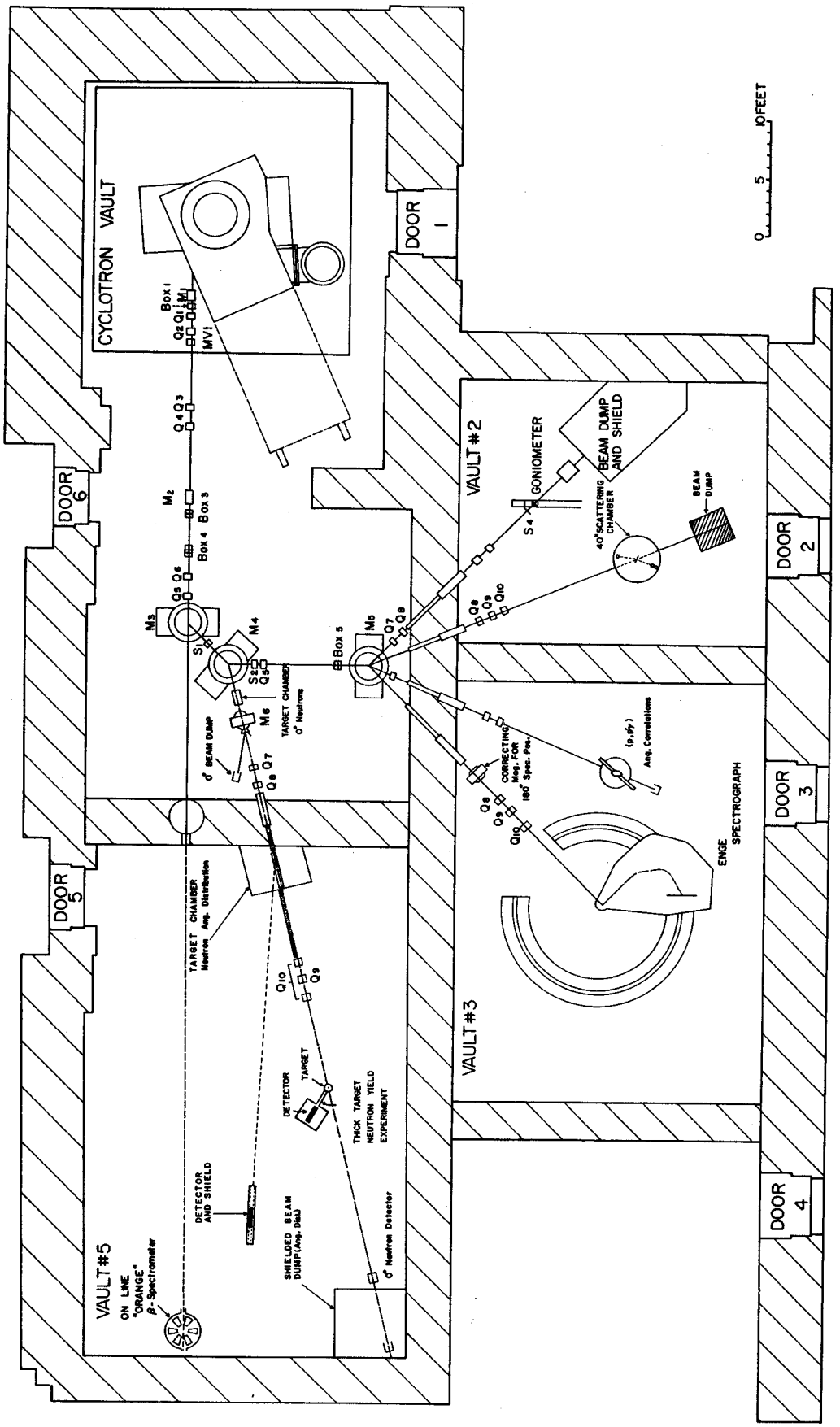

FIGURE 1. Layout of the cyclotron experimental area as of August, 1972.

1500. The fields in the two 45^{o} bending magnets, M3 and M4, were set using nuclear magnetic resonance probes. The beam energy calibration is accurate to 1 part in 10^{3}. In practice the bombarding energy was measured and when necessary reproduced to the nearest 0.1 MeV.

2.1.3 Beam Alignment

The beam was centered on the target either visually, using a wire target on a quartz scintillator and remote T.V. monitor or by balancing the beam on pairs of vertical and horizontal slits placed just before the spectrograph scattering chamber and just after the 40" scattering chamber. These slits were withdrawn after the beam was aligned. The beam spot was about 0.05" to 0.10" wide and about 0.1" high on gas targets and about 0.07" high on the solid melamine targets.

2.1.4 Beam Current

The beam on the melamine target was kept below 300 nanoamps and on the gas targets, below 800 nanoamps to avoid target or gas cell window deterioration.

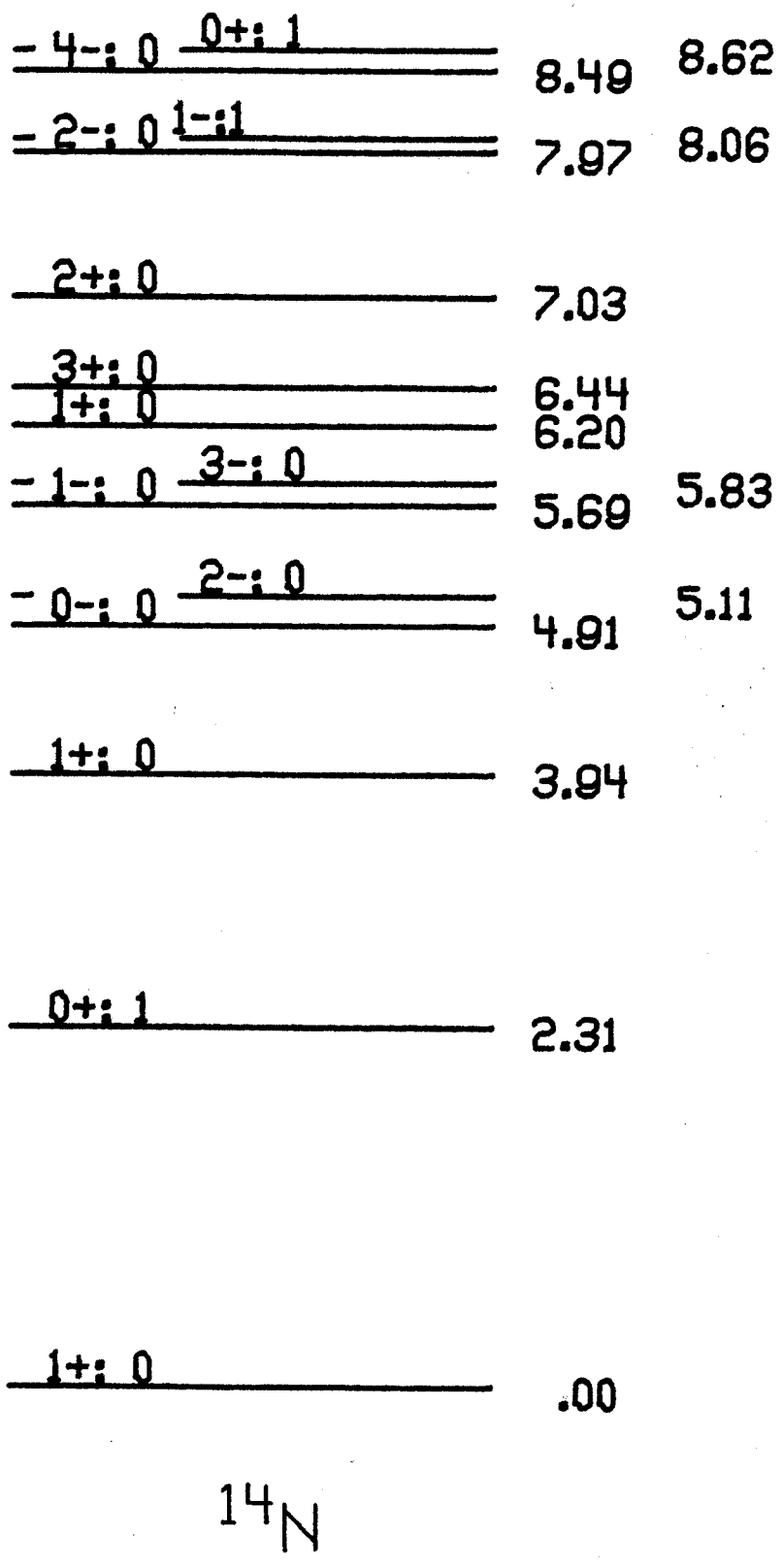

FIGURE 2. Energy levels of ^{14}N up to 8.62 MeV.

2.2 Measurements Made with Gas Targets

2.2.1 Gas Target Construction

At 29.8 MeV bombarding energy, the angular distributions for elastic scattering and for inelastic scattering leading to the first twelve excited states of ^{14}N were obtained with gas targets in the 35" and later 40" scattering chambers. The gas targets used were machined of brass and the 0.5 mil. kapton windows were epoxied onto the sanded clean brass with a ten to one mixture by weight of Ciba Araldite 502 and 951 hardner. Application of solvents to the brass after sanding seemed to weaken the bond. The gas pressure was about 50 cm of Hg for the 1" cells and 30 cm of Hg for the 2" cells. These pressures represent a compromise between the desire for higher count rates and sufficient cell lifetimes in the beam. At higher pressures, the cells tended to develop slow leaks after on hour or so in the beam.

2.2.2 Gas Cell Diameter and Scattering Angle Range

Figure (3) shows how the front and back slits of the collimating system define the line source of scattered particles observed by the detector at any given scattering angle θ. If θ is smaller than some angle, θ_{min}, or greater than some angle, θ_{max}, the area of the Kapton window through

TABLE 1. Collimation units' dimensions, foreward angle limits, and G factors.

Telescope	a (inches)	b (inches)	c (inches)	h (inches)	t (90°) (inches)	θmin 1" Cell	θmin 2" Cell	$\Delta\theta$ f.w.h.m.	G (inches)
C_1	14.5 $\pm$0.1	10.0 $\pm$0.1	0.127 $\pm$0.002	0.161* $\pm$0.005	0.241	25.7°	13.5°	0.07°	1.79×10^{-5}
C_2	12.0 $\pm$0.1	8.0 $\pm$0.1	0.127 $\pm$0.002	0.161* $\pm$0.005	0.254	26.6	14.2	0.09	2.71×10^{-5}
C_3	10.5 $\pm$0.1	6.0 $\pm$0.1	0.127 $\pm$0.002	0.161* $\pm$0.005	0.318	32.4	17.6	0.12	4.12×10^{-5}
C_4	12.8 0.05	10.0 $\pm$0.05	0.125 $\pm$0.001	0.127 $\pm$0.001	0.198	21.6	11.2	0.07	1.55×10^{-5}

*Oblong slit heights reduced to equivalent rectangular slit heights.

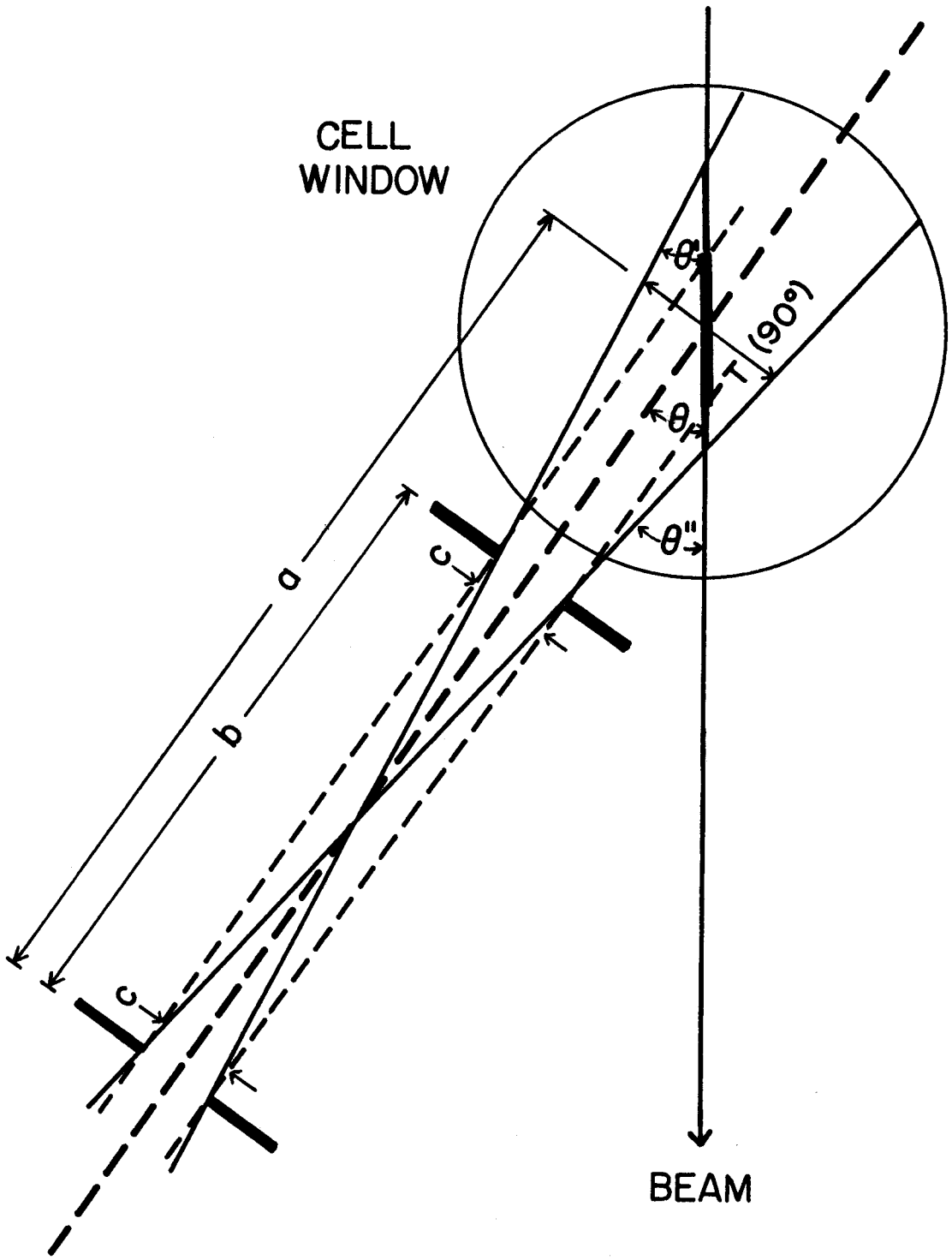

FIGURE 3. Definition of the line source target in a gas cell by the collimator's slits.

which the beam enters or leaves the gas cell becomes part of the target. This would complicate the calculation of the cross section and include unwanted background peaks in the spectra, for Kapton background peaks due to hydrogen and carbon would appear. It is shown in reference (Pi 70) that for small beam widths as used in this experiment, θ_{min} can be calculated from the formula:

$$\tan \theta_{min} = \frac{2\ t\ (90°)}{D}$$

where t (90°) is the length of the line source of the gas target for a lab scattering angle of 90° and D is the diameter of the gas cell. θ_{max} is $(180 - \theta_{min})$. θ_{min}, θ_{max}, and t (90°) for different collimators and gas cells are tabulated in Table ( ). In practice, the appearance of ^{12}C peaks in the spectra was used to detect these limits.

2.2.3 Effective Target Thickness

The effective target thickness of a gas target is just the product of the gas density and the effective length of the line source defined by the collimators. Neglecting corrections for the changing effectiveness of the penumbra, the effective target length at angle θ is $t(90^{\circ})/\sin\theta$. For the collimator system with the best angular resolution, a gas pressure of $\frac{1}{2}$ atmosphere, and temperature at 23°C, the effective target thickness at 90° was 268 $\mu g/cm^2$. This amounts to an energy loss of 4 keV for 30 MeV protons.

2.2.4 Gas Pressure Measurements

For the absolute measurement of the ^{14}N (p, p) angular distribution at 29.8 MeV a mercury manometer was used to continually monitor gas cell pressure. The error for this measurement was about ± 1 mm. The cell pressure for the normalization points taken at 36.6 and 40.0 MeV were measured with a Wallace and Tierman Type FA-145 MM 17069 aneroid gauge. According to the manufacturer's specifications these measurements were good to ± 0.8 mm or ± .1% of full scale. The gauge checked with the weather bureau to within 2 mm or 0.3%.

2.2.5 Gas Temperature Measurement

The gas temperature was measured by determining the temperature of the scattering chamber and assuming the gas cell and gas temperature to be the same. The temperature of the scattering chamber was observed not to vary more than ± 0.5°C during a run. H. W. Laumer (La 71) and W. L. Pickles (Pi 70a) have both looked into the question of local heating of the target gas by the passing beam. Both Pickles and Laumer measured a particular cross section with different beam intensities. Laumer found no significant change in

cross section for a five-fold increase (100-500na) in current while Pickles found the same result for a ten-fold increase (10-100na) in current. The statistical error in Laumer's investigation was 1.5% and in Pickles', 1%.

2.2.6 Scattered Particle Collimation Units

For a gas cell target, two apertures are needed to define the solid angle and the radial acceptance angle. If only one aperture is used in front of the particle detector, the entire length of the beam passing through the gas would be the line source of scattered particles. To restrict the length of the line source of scattered particles, a slit at some point between the target and back aperture must be used. In this experiment the height of the target was determined by the beam's vertical width and so the front slit functioned only in the horizontal direction. In Figure (3) we have a top view of the situation. The horizontal openings of the two apertures define two regions of the line source. For the center section, defined by the intercepts of the two dashed lines with the beam, each point along the beam has access to the full solid angle of the back aperture. Points along the beam in the penumbra of the slit telescope have access to only part of the back aperture. The geometry dependent G factor that appears in Silverstein's (Si 59) expression for the differential cross section below is the

integral of the solid angle from any point along the beam over the length of beam that the slits define as the target, and includes corrections due to the first and second derivatives of the differential cross section.

$$\frac{d\sigma}{d\Omega} = \frac{\sin\theta}{G} \frac{N_p}{N_T N_B}$$

$$G = G_o (1 + X + \bar{=}' Y + \bar{=}'' Z)$$

where:

N_p = the yield at lab angle θ

N_T = the number of target nuclei per cm^3

N_B = the number of incident particles

X, Y, and Z are functions of the shapes of the beam cross section and of the slits

σ' and σ'' are the first and second angular derivatives of the differential cross section.

The program "G-FACTOR" written by Dr. R. A. Paddock and based on Silversteins analysis was used to calculate the values of G needed. σ'/σ and σ''/σ were nowhere large enough to require slope corrections to be included in G calculations. Formulas useful for estimating G_o and the kinematic broadening for certain slit telescopes are developed in Appendix A.

The collimating units used were designed and built by Dr. Bill Pickles and are described in his thesis (Pi 70b). Figure (4) is a schematic drawing of one of these units. An important feature of these units are the baffle slits. Their purpose is to eliminate particles slit scattered by the sides

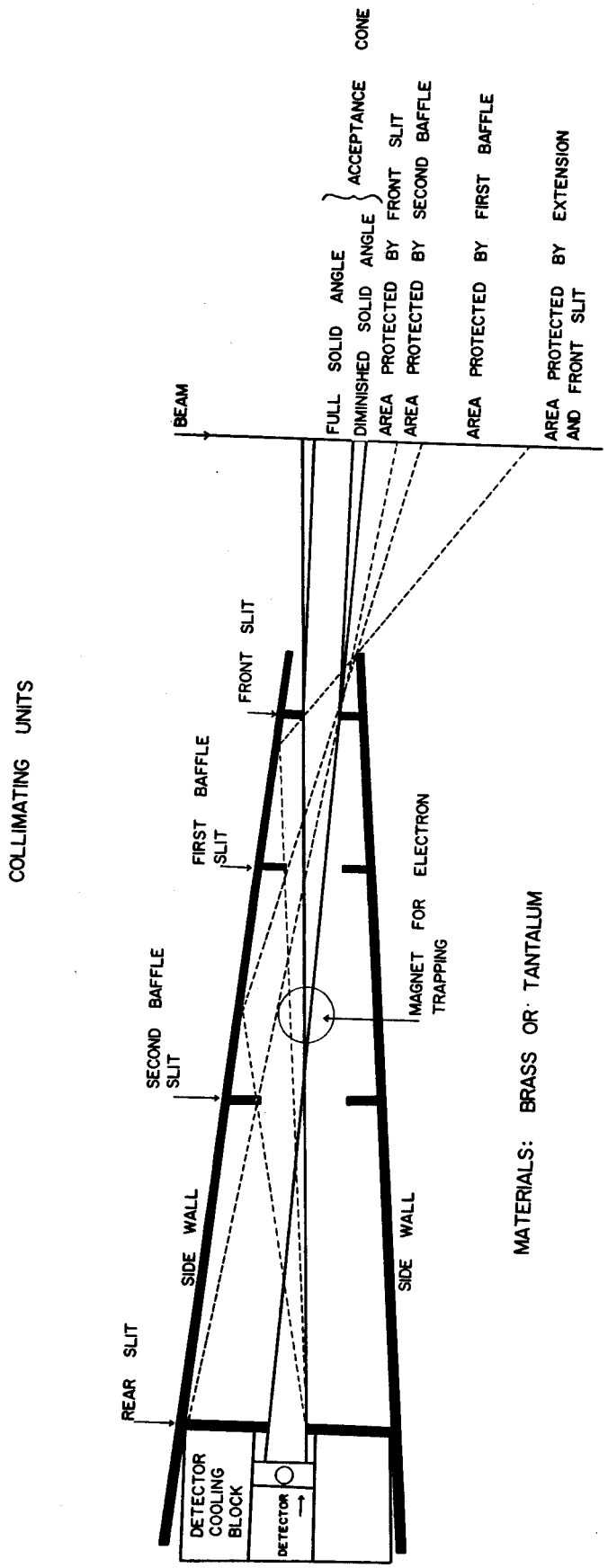

FIGURE 4. A schematic drawing of one of the collimating units.

of the front slit. The front and rear geometry defining slits are themselves made up of two slits. The first defines the opening of the slit but is thick enough only to degrade particles passing through it so that they appear in the spectra below the region of interest. The second slit placed just behind the first is thick enough to stop the expected products of the reaction but has an opening slightly wider than the first slit. Thus only an area proportional to the thickness of the first slit is a source of slit scattering. A small permanent magnet was set in the collimator to trap electrons that might have been swept along by the scattered particles. Side walls of tantalum or brass protected the counters from stray particles.

Four different geometries were used in taking data. They will be referred to as C1, C2, C3, and C4 and their dimensions and specifications with errors appear in Table (1). C1 had the best resolution and smallest G factor. It was used at forward angles where the background under the peaks of interest was highest and resolution a definite asset. C3 is characterized by poorer angular resolution but larger solid angle and was used at backward angles. C2 represents a compromise. It was used at a number of middle and back angles and for the measurement of the elastic scattering. C4 was used in absolute normalization runs.

2.2.7 Angular Measurement

The apparatus used to measure the scattering angle in the 35" scattering chamber is completely described in Dr. Pickles' thesis (Pi 70c). The relative angle error for the system is quoted to be 0.1^{o}. Before each run a surveying transit was aligned along the beam line. The collimator was rotated to 0.00^{o} on the readout and the beam line was seen to go through the middle of the slits to within a few mils. The wire target on the scintillator was then aligned with the beam. Thus the angular errors were much less than the 0.7^{o} full angular acceptance of C1.

2.2.8 Beam Current Measurement

The beam is dumped on an aluminum plug at the back of a 57" long section of 4" diameter beam pipe, insulated from the scattering chamber by a 1.5" plastic section of beam pipe. Horseshoe magnets were placed on the beam line to trap electrons streaming along with the beam. The current was integrated by an Elcor model A310B current indicator and integrator, tested with a 1.35 volt mercury battery in series with a 1% 4.5 meg. ohm resistor. Input was made at both the Fraday cup and at the current integrator and the calculated charge and integrated charge agreed within 1%. The overall integrating accur-

acy was 2%.

2.2.9 E/△ E Dectector Telescope

Charged particles of equal kinetic energy but differing in mass and charge will loose different amounts of energy in passing through a detector. Using a detector telescope this can be exploited to generate separate energy spectra for different detected particles. The front detector, the △E-detector, must be thin enough to transmit the least penetrating particle of interest, yet thick enough to produce a useful signal for the most penetrating particle. The back detector or detectors must be thick enough to stop any particles of interest after they pass through the △E detector. In this experiment, the △E detector was a 500 μm surface barrier silicon detector and the back detector was a 5.0 mm lithium drifted silicon detector. The detectors were cooled by circulating alcohol, cooled in a reservior in contact with dry ice. This alcohol was pumped through copper tubing attached to a brass cold finger in contact with the detectors. Figure (5) is a schematic of the detector package. Three signals are measured; a △E signal from the front detector, an E_B from the back detector, and the total energy, Es = △E + E_B from the connected cases of the two detectors.

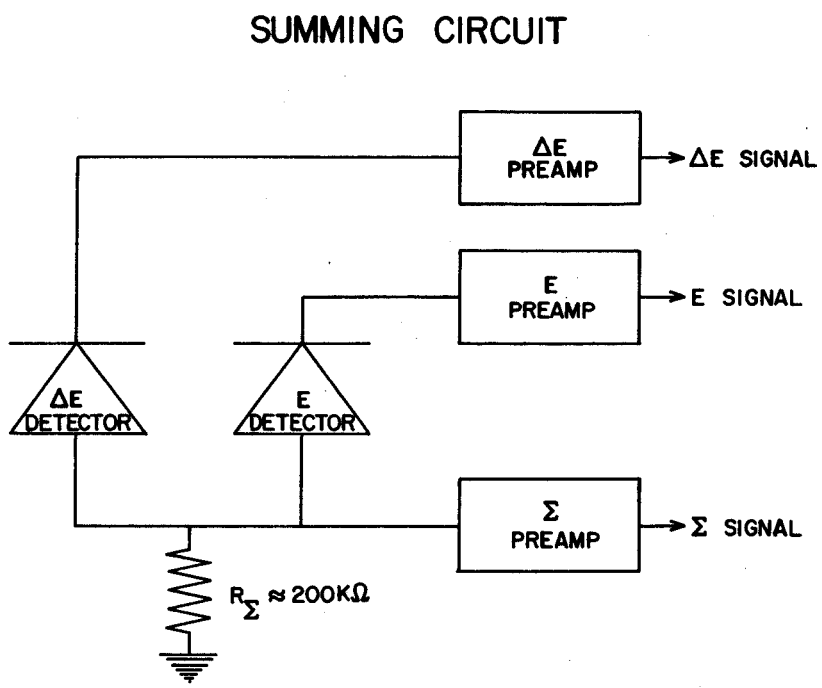

FIGURE 5. Two detector telescope summing circuit.

2.2.10 E/△E Signal Processing

The electronic set up for handling the signals is shown in Figure (6). The △E/E option of program TOOTSIE (Ba 71) running in the M.S.U. Cyclotron Lab. SIGMA-7 computer was used to provide particle identification. The code first generates two dimensional △E, Es spectra which may be displayed on a cathode ray screen (Figure [7]). The different particle bands are then defined by lines generated as polynomial fits to chosen points. The code uses these lines as gates on the △E and Es signals to generate separate Es spectra for each band. For the detectors used here only proton and deuteron bands were defined. Only the proton spectra were useful and one is reproduced in Figure (8). The f.w.h.m. for peaks of interest in this spectra was 80 KeV. For some spectra the f.w.h.m. was as high as 105 KeV.

2.2.11 Monitor Detector

A cesium iodide crystal mounted on a photo tube was used as a monitor counter with the gas targets, to provide dead time corrections, and for run to run normalization when necessary. The package used was designed and built by L..Learn of the Cyclotron Lab. except that an additional slit was placed between the detector and gas cell. A single channel analyzer was set to accept the elastic proton peak.

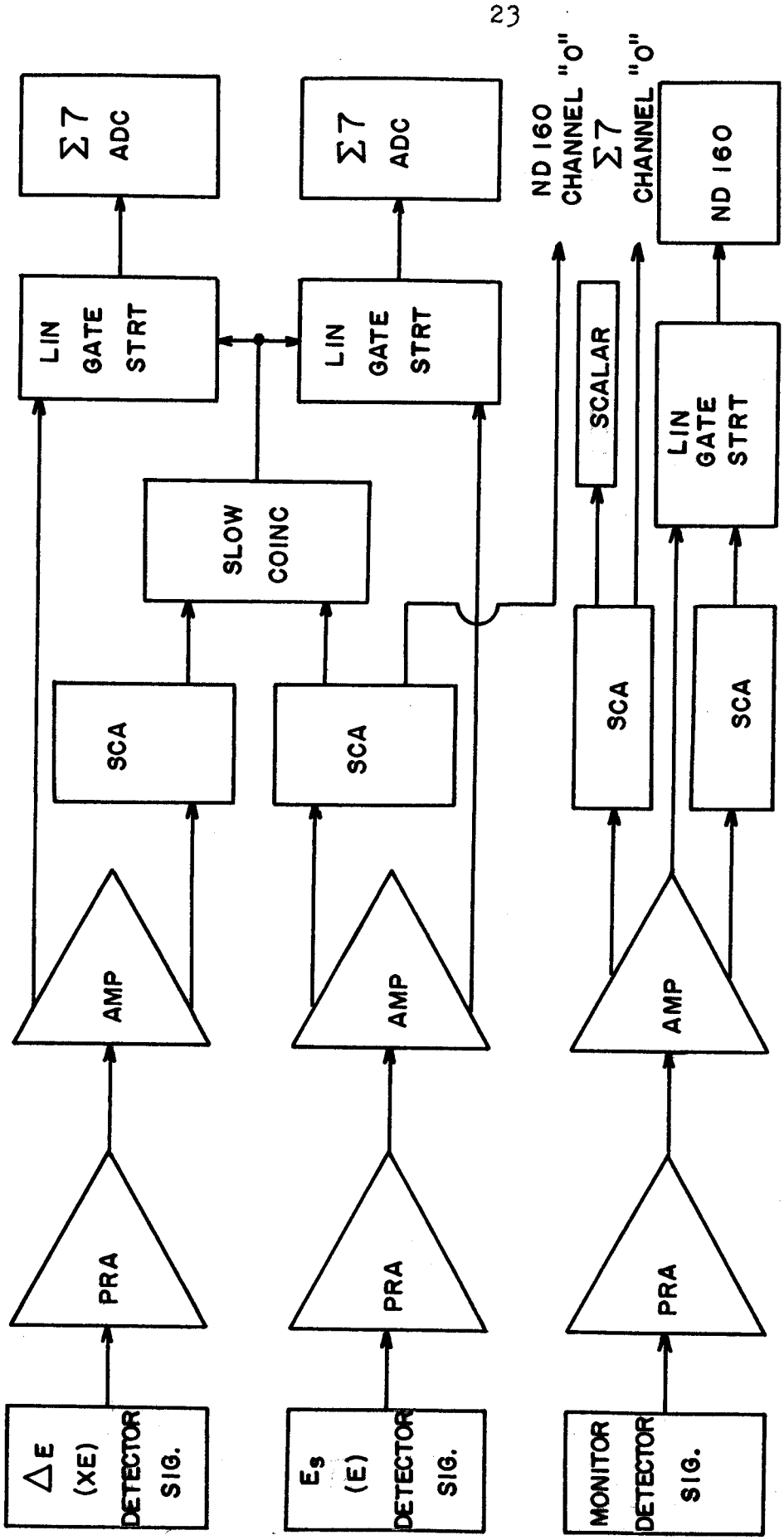

FIGURE 6. Signal processing electronics.

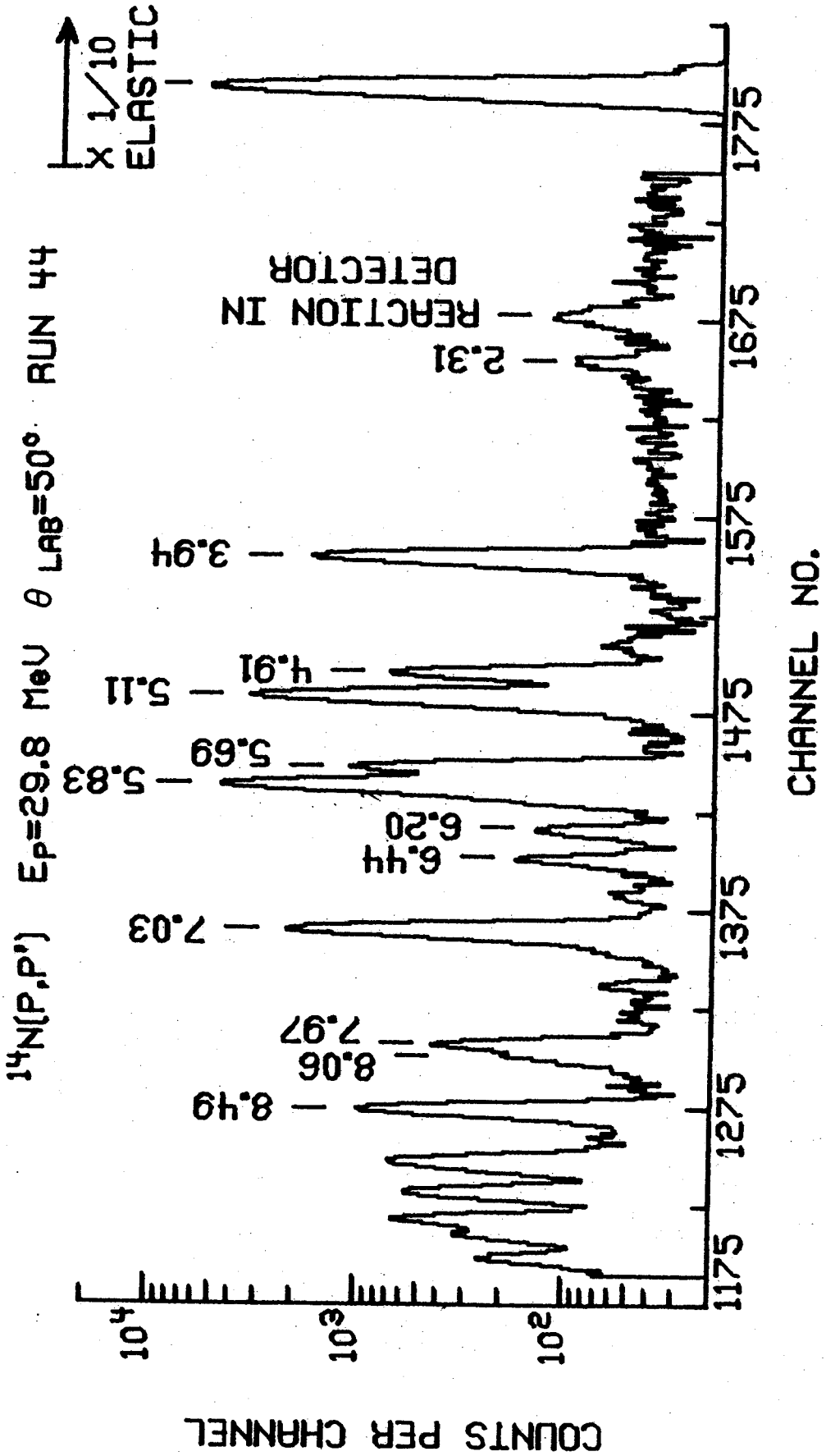

FIGURE 8. A proton spectrum taken with the E/ΔE detector package and gas target.

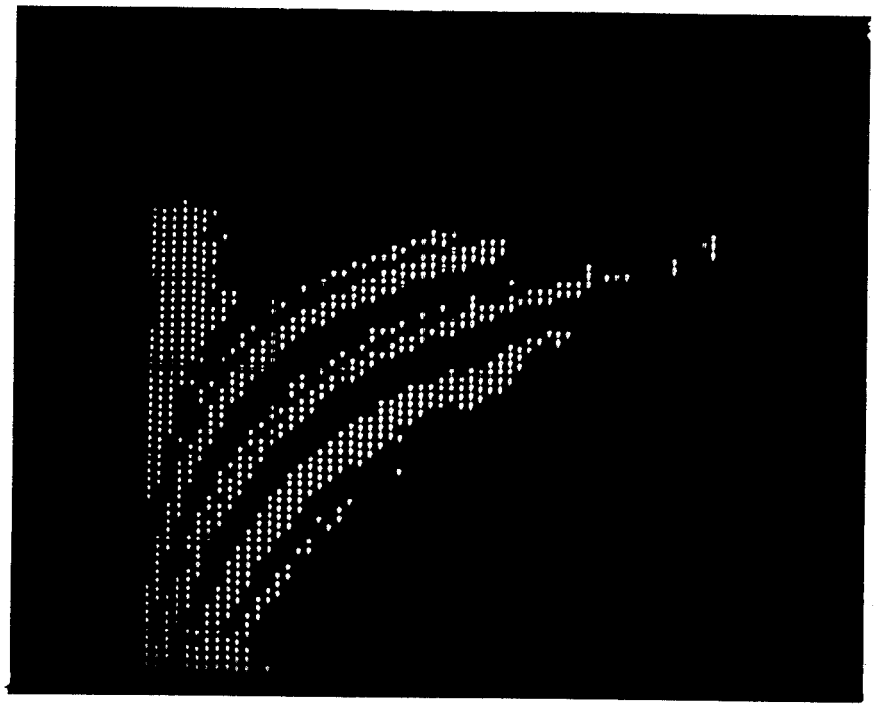

FIGURE 7. Two dimensional TOOTSIE display.

The slow logic pulse output of the single channel analyzer was sent to a scaler and the channel zero input of the program TOOTSIE.

2.2.12 Degrader — Detector Combination for 36.6 and 40.0 MeV Absolute Normalization Measurements

Absolute normalization of the 36.6 and 40.0 MeV spectrograph data was accomplished by measuring points of the elastic scattering angular distributions with a gas cell target in the 40" scattering chamber. The detector was a 5 mm Si(li) detector with a 0.114" thick aluminum absorber for 40.0 MeV bombarding protons and with a 0.064" thick aluminum absorber for 36.6 Mev bombarding protons. The degraders were placed directly in front of the detectors so that losses due to elastic scattering at angles less than 45^{o} could be neglected. The total reaction cross section for 29 MeV protons on ^{27}Al is 775 $\pm$ 37 mb (Ma 64) and for 34 MeV protons, 600 $\pm$ 20 mb (Go 59). The total elastic cross section for 29 MeV protons by ^{27}Al at angles greater than 45^{o} in the lab, is 90 mb (Ma 64). Thus proton reactions with the aluminum absorbers could remove about 1% of the proton flux to the detector, and the resulting cross sections had to be corrected for this.

2.3 Measurements Made with the Enge Split-Pole Spectrograph

2.3.1 The Spectrograph vs. the Scattering Chamber

There are a number of problems associated with doing this experiment in the scattering chamber as described so far. The excitation of 1.78 MeV state of ^{28}Si by inelastic scattering in the solid state detectors, of protons elastically scattered from the ^{14}N gas target, produces a peak in the proton spectra close to the peak due to excitation of the 2.31 state in ^{14}N. For 29.8 MeV incident protons and at 30° in the lab, the silicon reaction peak was 250 KeV f.w.h.m. and appeared 410 KeV above the ^{14}N 2.31 peak. The 2.31 state is weak and of primary interest. Thus one must resolve it and the peak due to the above excitation in the detector. For a light nucleus like ^{14}N where kinematic broadening is important this means a small solid angle. Even if the resolution is good enough at forward angles, this artifact peak will get closer to the 2.31 peak as you go back in angle. As you go back in angle, the spectrum becomes compressed. For 36.6 MeV incident protons, the difference in lab energy between elastically scattered protons and protons from the 2.31 state in ^{14}N at 5° is 2.315 MeV, at 90° it is 2.152 MeV, and at 120°, 2.071 MeV. The peak, due to the reaction in the detector, appears at the same energy down from the elastic peak for all angles. In the scattering

chamber the tail of the elastic proton peak produces a high background at angles forward of 30° in the lab. Also, the high elastic count rate is a problem in itself at forward angles in the scattering chamber. These problems are all avoided by using the Enge Split-Pole spectrograph, since the elastic protons do not fall on the detector when the 2.31 state is being measured. This allowed measuring the cross section for the 2.31 state at angles as small as 10° in the lab, and reduced the resolution required so that thick targets and solid state position sensitive detectors could be used.

The Enge Split-Pole double focusing magnetic spectrograph also allows one to compensate for kinematic broadening by proper positioning of the spectrograph focal plane and so a large solid angle can be used without loss of resolution. The program SPECTKINE (Tr 70a) incorporates Enge's (En 67) linear approximation to the displacement of the focal plane from the first order focal plane due to kinematic broadening. For a given interaction, energy, and effective radius of curvature, SPECTKINE calculates the required magnetic field strength and focal plane position. Thus it was possible to use a slit 0.368" x 0.372" that subtended 1.202 millisterradians for the 36.6 MeV runs and a slit that was (0.372") x (0.298") subtending 0.972 millisterradians for the 40.0 MeV runs. Table (2) contains the dimensions with errors of the slits used. In the spectrograph it was possible to measure the weakest points of the 2.31 angular distributions with 3%

TABLE 2. Dimensions of spectrograph apertures.

Slit	Height	Width	Solid Angle (Millistereradians)	Error Due to Rounded Corners
1	0.372" ±0.001" (2°)	0.368" ±0.001" (2°)	1.202	.75%
2	0.372" ±0.001" (2°)	0.298" ±0.001" (1.7°)	0.972	1.0 %

statistical errors in about 30 minutes of running time.

One disadvantage of doing this experiment in the spectrograph was the small area of the focal plane that we could cover with the one working solid state position sensitive detector available. Thus it was only practical to measure the elastic and first two excited states in ^{14}N. Another disadvantage is that the spectrograph scattering chamber and beam line has equipment incorporated to facilitate high resolution spectroscopy. This equipment limited the back angle to which we could measure the 2.31 cross section at 40.0 MeV to $\theta \leq 120°$. Figure (9) shows the the basic geometry of the spectrograph.

2.3.2 Melamine Targets

The ^{14}N target used in the spectrograph experiments was melamine ($C_3 H_6 N_6$) in $NH_2C{:}NC(NH_2){:}NC(NH_2){:}N$ on 100 $\mu g/cm^2$ carbon foil backings. There are several problems associated with making evaporated melamine targets. Melamine is a fine white powder that sublimes at 354°C. If one evaporates it in an open boat, the escaping vapor carries with it unevaporated clumps of the material. If one uses a boat with one or more pinholes as a source, heat radiating from that source raises the temperature of the carbon foil and the melamine plates out on everything but the target. A heat shield with a small hole will trap almost all of the

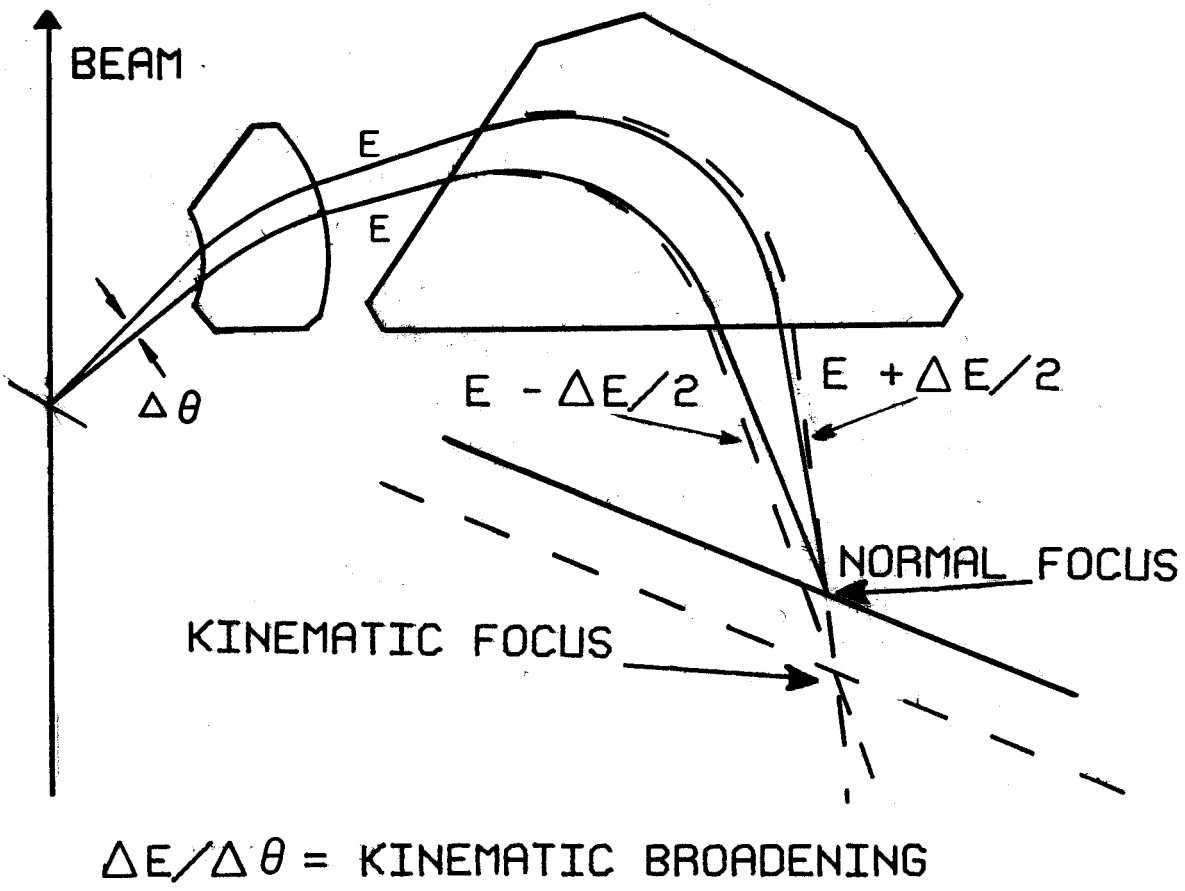

FIGURE 9. Kinematic correction in the Enge split-pole spectrograph.

vapor before it gets to the carbon foil and the hole will fill up before a useful target is made. A solution was found by covering an open boat with a fine stainless steel mesh that was heated along with the boat itself. The clumps would either be trapped or evaporated by the mesh which was of 0.0021" wire with 200 wires to the inch. Relatively clump free targets as thick as the 3.1 mg/cm^2 target used for the 40.0 MeV measurements were made with this mesh covered boat.

Melamine slurry targets were also used for some of the data at 36.6 MeV. One part polystyrene to three parts by weight of melamine were mixed in benzene. The mixture was sprayed onto a glass slide that had been covered with a thin layer of Tepol. The target was then pealed off the slide. These targets were relatively grainy and non-uniform, worsening the resolution in the spectra taken with them.

2.3.3 Target Spinner

If the melamine target were left stationary in the beam the beam would evaporate the melamine off the target spot. Thus the target was rotated about an axis parallel to the scattering plane but displaced about 3/8 of an inch above the beam. The target spinner is shown in Figure (10). The driving torque is transmitted through a 1 mm quartz vacuum window by means of a "magnetic clutch." The target was rotated at about 600 rpm and withstood beams of 300 nanoamps

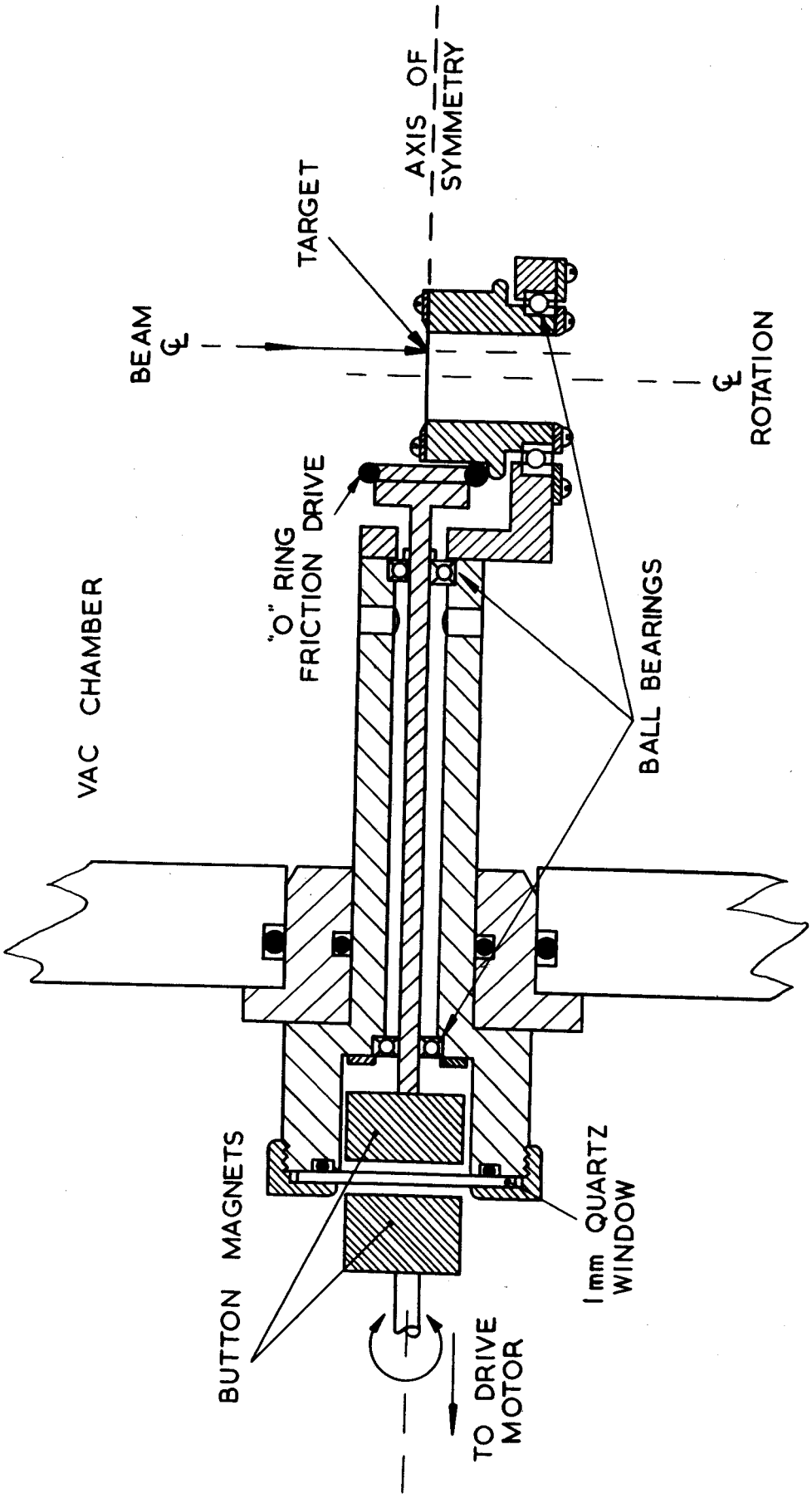

FIGURE 10. A schematic drawing of the target spinner.

for 10 to 20 hours. There was discoloration of area exposed to the beam but little decrease in thickness as measured by the monitor counter and integrated current.

2.3.4 Silicon, Surface Barrier, Position Sensitive Detector

The scattered particles were detected at the focal plane of the spectrograph by a Nuclear Diodes (Da 69) silicon surface barrier position sensitive detector. This detector was 3 cm long and 1 cm high. Its thickness was 300 μm, but since the particles were incident at 45°, the effective thickness was 425 μm. Two signals are taken from the detector, an E signal proportional to the energy lost by a particle passing through the detector and an XE signal proportional to the product of the energy lost and the position along the segment of the focal plane covered by the detector. The XE signal is obtained by dividing a signal equal to the E signal between the two ends of the thin resistive back layer of the detector.

2.3.5 Particle Identification

For particles of equal magnetic rigidity, $B\rho$, but different masses and whose range in silicon is long compared to the detector thickness, the E signals are proportional to their masses squared (Da 69). This makes it possible to

separate events due to particles differing in mass.

2.3.6 Signal Processing Electronics

The electronics setup used including that for the monitor counter is shown in Figure (6). The detector has a large area and so large capacitance. Noise in the XE signal is due to a relatively small resistance ($\sim$10KΩ) in series with that capacitance. A short shaping time constant ($\sim$ .2 μsec) will reduce the more serious resistive noise at the cost of reducing the size of the slow rising XE signal, and increasing its non-linearity. 40 MeV incident protons lose only about 900 KeV in 450 μ of silicon so that one cannot afford too great a reduction of the XE signal. In this experiment, all the shaping times on the Ortec model 451 spectroscopy amplifier used for the XE signal were set at 2 μsec. Other settings did not improve the resolution.

2.3.7 Computer Data Handling

The two signals E and XE were handled by the XE/E routine of the program TOOTSIE (Ba 71a) running in the Σ 7 computer. In SETUP MODE the E and the quotient XE/E were analyzed into a 128 x 128 array. This array was displayed on a TEKTRONIX 611 storage scope with E the ordinate and XE/E the abcissa. The program allows for areas in the E,

XE/E space to be associated with particles of a particular mass. In RUN MODE, the windows set in SETUP MODE are used to separate the incoming data into position spectra for the particle masses defined. In this experiment proton and deuteron bands were defined and 512 channel position spectra were obtained. One such spectrum is shown in Figure (11). The resolution in this spectra is 56 KeV f.w.h.m. which corresponds to a position resolution of about 1.6 mm f.w.h.m. Other data taken also at 40.0 MeV but with a thinner target had a resolution of 35 KeV f.w.h.m. or about 1.0 mm f.w.h.m.

2.3.8 Monitor Detector

The monitor counter was very important in this experiment because it provided the only reliable point to point normalization of the data. The melamine target contains ^{12}C as well as nitrogen and so resolution had to be good enough to separate the elastic peaks due to the two. For the 36.6 MeV run a 5 mm Si (Li) detector was placed at 150° inside the spectrograph scattering chamber. A 10 mil copper absorber was used to insure that the particles would stop in the detector and the detector was not cooled. Background from the Faraday cup limited the beam current to about 250 nanoamps. One of the monitor spectra taken at 40.0 MeV is shown in Figure (12). For the 40.0 MeV run, the monitor was again at 150° but now it was outside of the scattering chamber

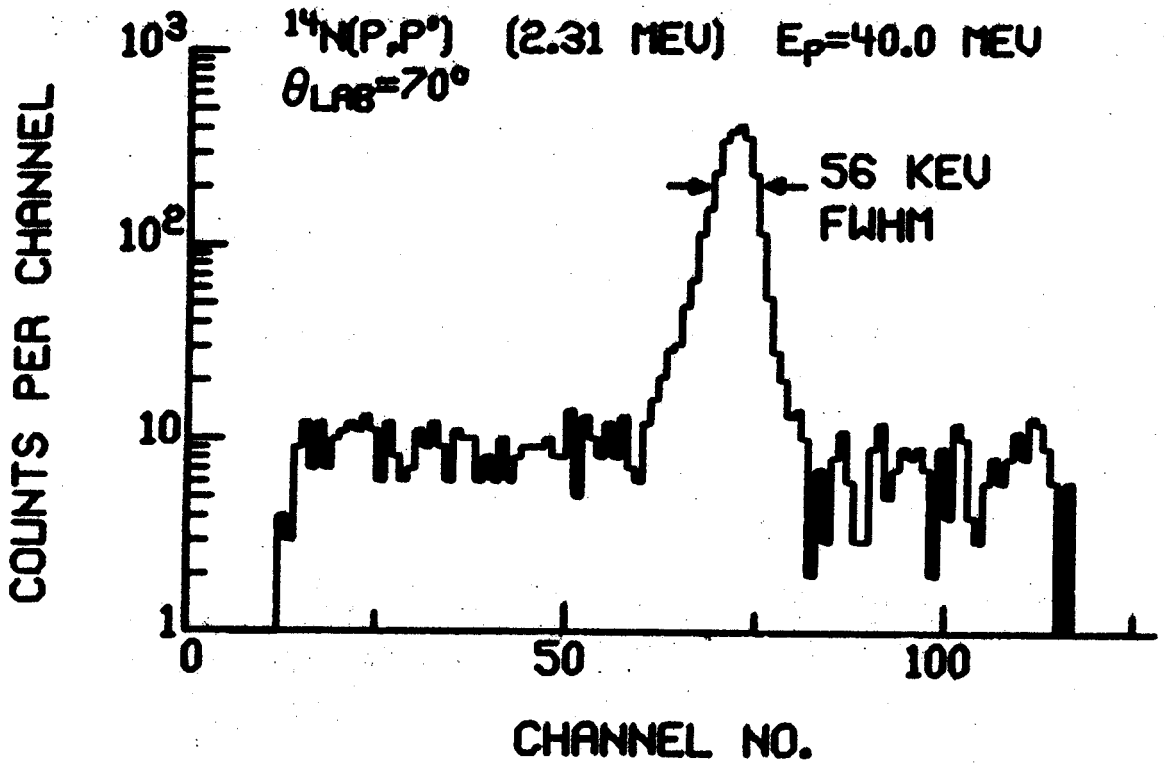

FIGURE 11. Spectrum taken in the spectrograph.

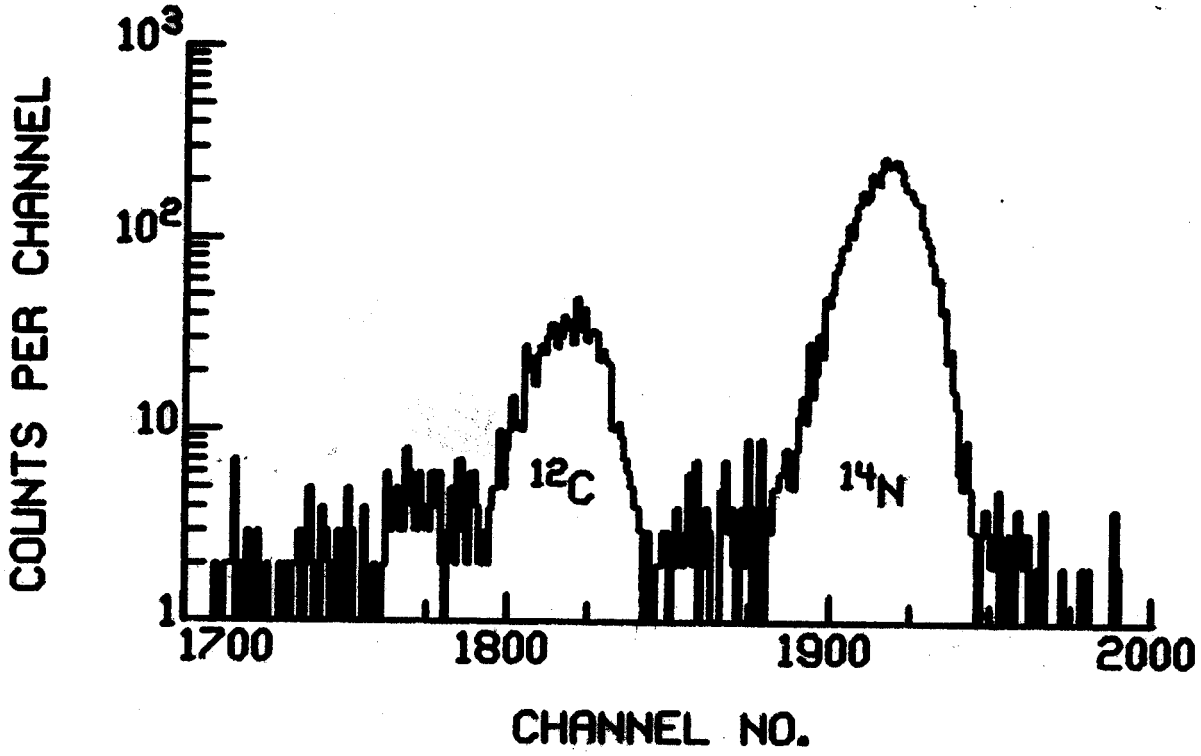

FIGURE 12. 40.0 MeV monitor spectrum from an evaporated melamine target. The detector angle is 150°.

and cooled to the temperature of alcohol circulated around dry ice. The 10 mil absorber was still used. Due to the increased distance between the detector and Faraday cup and to improve shielding made possible by the improve geometry, current was not limited by background in the monitor.

As one can see from the monitor electronics in Figure (6), that monitor spectra were recorded. A logic signal generated by a single channel analyzer on the E signal from the position sensitive detector was used to keep track of the monitor spectra dead times.

3. DATA

3.1 General Description of the Data

For incident proton energies of 29.8, 36.6, and 40.0 MeV angular distributions for elastic scattering from ^{14}N and for the reaction $^{14}N(p, p') \, ^{14}N^*$ to the first two excited states at 2.31[+] and 3.94 MeV were obtained. In addition angular distributions for 29.8 MeV incident protons of the reaction $^{14}N(p, p') \, ^{14}N^*$ to the ten excited states between 4.91 and 8.49 MeV were obtained. These 29.8 MeV angular distributions were taken with gas targets. The resolution obtained for these angular distributions was as good as 80 KeV at 30° and as poor as 105 KeV at about 85° where kinematic broadening is greatest. This resolution was such that all but the 7.97 and 8.06 MeV state and the 8.62 and 8.49 MeV states were resolved. Where the 5.69 MeV state was not resolved to its half maximum point from the 5.83 MeV state, the code SAMPO (Ro 69) was used to reduce the data.

[+] ^{14}N energy levels are taken from the F. Ajzenberg-Selone compilation of energy levels for A = 13, 14, and 15 nuclei. F. Ajzenberg-Selone, Nucl. Phys. A152 (1970) 1-221.

SAMPO can be used to fit a Gaussian shape with exponential tails to isolated peaks in the spectra. The three shape parameters involved are stored as a function of channel number of the peaks fit. The program does a linear interpolation to assign shape parameters to other peaks in the spectrum. To fit a doublet the program varies the heights and centroids of the two appropriate shapes until the overall envelope is fit.

An attempt was also made to separate the states at 7.97 and 8.06 MeV with SAMPO, but here the results were not as reliable. At forward angles reactions in the detector and contaminants in the target complicated the extraction of the angular distributions for the 6.44 and 7.03 MeV states.

The angular distributions at 36.6 and 40.0 MeV were taken in the M.S.U. Enge Split-Pole spectrograph. Non-uniformities in the target used for the initial 36.6 MeV run spread the peaks out and made it necessary to make some correction for non-linearities in the silicon surface barrier position sensitive detector. The 40.0 MeV data as well as check points for the 29.8 and 36.6 MeV angular distributions of the 2.31 state were taken with improved evaporated targets. Here the peaks were narrow enough that background and non-linearity corrections were not serious problems. The relative uncertainty of this data was less than 5% and the check points agreed with the earlier data at 29.8 and 36.6 MeV.

3.2 Reduction of Gas Target Data

3.2.1 2.31 MeV State Data: Gas Target Data

The peak to valley ratio at 30° in the lab was 1.5 to 1 for the 2.31 MeV peak and so background subtraction for $\theta \leq 60°$ was the main source of error. The background was subtracted using the code MOD-7 (Au 70) which fits a polynomial to sections of the background on either side of the peaks of interest and then continues this background under the channels containing the peaks. Backgrounds representing upper and lower limits were drawn and the average taken. The error assigned to choosing the background was 1/3 of the difference between the net number of counts in the peak with either extreme background. Where the 1.78 MeV silicon state was clearly separated from the 2.31 MeV peak it too was reduced and its strength relative to the elastic peak calculated. The ratio of 1.78 ^{28}Si to elastic ^{14}N was found to average $20 \pm 2 \times 10^{-4}$. Where the 1.78 MeV silicon peak and the 2.31 MeV peak were not separated SAMPO was used to strip the 2.31 MeV peak. MOD-7 was used to find the total number of counts in the combination from which an estimate of the 1.78 MeV silicon peak based on its ratio to the elastic peak was subtracted. The final result was the average of the two values with an error due to separation of 1/3 the difference between the two values. $^{14}N(p,p')$ spectra taken at

24.8 MeV incident proton energy by Crawley et al. (Cr 70) were reanalyzed in this way, and no disagreement with the published cross section was found.

3.2.2 Inelastic Gas Target Data other than the 2.31 MeV State Data

The rest of the gas cell data was stripped using both SAMPO and MOD-7. MOD-7 was sufficient for all but the 5.69 and 5.83 MeV state combination and the 7.97 and 8.06 MeV state combination. The backgrounds most easily drawn with MOD-7 seemed a little low to the eye and since the background of SAMPO seemed to be high to the eye, thus all the data was stripped with both SAMPO and MOD-7. The isolated peaks were used as a test of SAMPO's ability to reproduce the peak shapes and areas. For the elastic, 3.94, 6.20, 6.44, and 7.03 MeV states the results of SAMPO and MOD-7 were averaged and 2/3 of the difference between the average and either of the results taken as the error due to background subtraction. The 4.91 and 5.11 MeV peak combination and the 5.69 and 5.83 MeV peak combination were first stripped with SAMPO and the results taken as the lower limit. Then MOD-7 was used on the combined peaks and the sum for each combination taken as the upper limit. The SAMPO results scaled up to that seem to provide upper limits for the peaks. The average was then taken. The 7.97 and 8.06 MeV states appeared

as a doublet and SAMPO was the only hope of obtaining separate angular distributions. The results of separating these two peaks using SAMPO indicates that the 7.97 MeV state is from 5 to 10 times stronger than the 8.06 MeV state. A test of SAMPO on a series of manufactured doublets described below leads to an estimate of the error in separating out the 7.97 MeV state of 5% and of 20% for the 8.06 MeV state. SAMPO was also tried on the 8.49-8.62 MeV state combination, but it could not locate the 8.62 state. The assumed controid locations for the two peaks were input to SAMPO. The code rejected the 8.62 MeV state and fit the combination as a singlet. The resultant fit was as good as that to known singlets. Thus the excitation cross section for the 8.62 MeV state must be less than 30 μb/sr at 30° in the lab. The test of SAMPO described below indicates that the peak would not have been rejected if it were 10% as strong as the 8.49 MeV peak.

The quantum numbers (0 + 1) of 8.62 MeV level were established in the early 1950's, through the study of the ^{13}C (p , γ) $^{14}N^*$ reaction and resonances in the cross section of the reaction ^{13}C (p, p) ^{13}C (Se 52, Wo 53, Mi 54). The state has been seen in the reactions ^{12}C (^{3}He, p) ^{14}N with a cross section of about 0.3 mb/sr at 15° in the lab for 20.1 MeV incident ^{3}He (Ma 68), and in the reaction ^{15}N (p, d) ^{14}N with a cross section of 0.02 $\pm$ 0.01 mb/sr at 21° $\pm$ 2° in the lab for 39.8 MeV incident protons (Ma 68).

3.2.3 A Test of SAMPO

To see how well SAMPO could be expected to do on the present data a set of spectra were manufactured. A section of a typical spectrum containing an isolated peak was selected. It was then added to itself after being shifted some number of channels and multiplied by a scale factor. Thus the areas and separation of the peaks making up the resultant doublets were known. The scale factors used were 1, 0.75, 0.5, and 0.1, and the centroid separations ranged from 1 channel to 8 channels. The f.w.h.m. of the original peak was about 6 channels, and the shape parameters were taken from other peaks in the original spectrum. For the spectra with scale factors 1.0, 0.75, and 0.50, SAMPO separated the doublet into two peaks with the correct area within 2% when the separation between the two was 5 channels or more. For the spectra with a .10 scale factor, the larger peak was reproduced quickly but the smaller one was about 15% too large at a separation of 5 channels. At a separation of 8 channels the error was about 7%. It should be pointed out that 5 channels of separation were less than the f.w.h.m. of the peaks and the doublet looked unresolved to the eye. See Figure (13). It was found that changing the initial estimate of the centroid locations for the peaks in a doublet did not effect the final results. If the fitting process converged, it always converged to the same result.

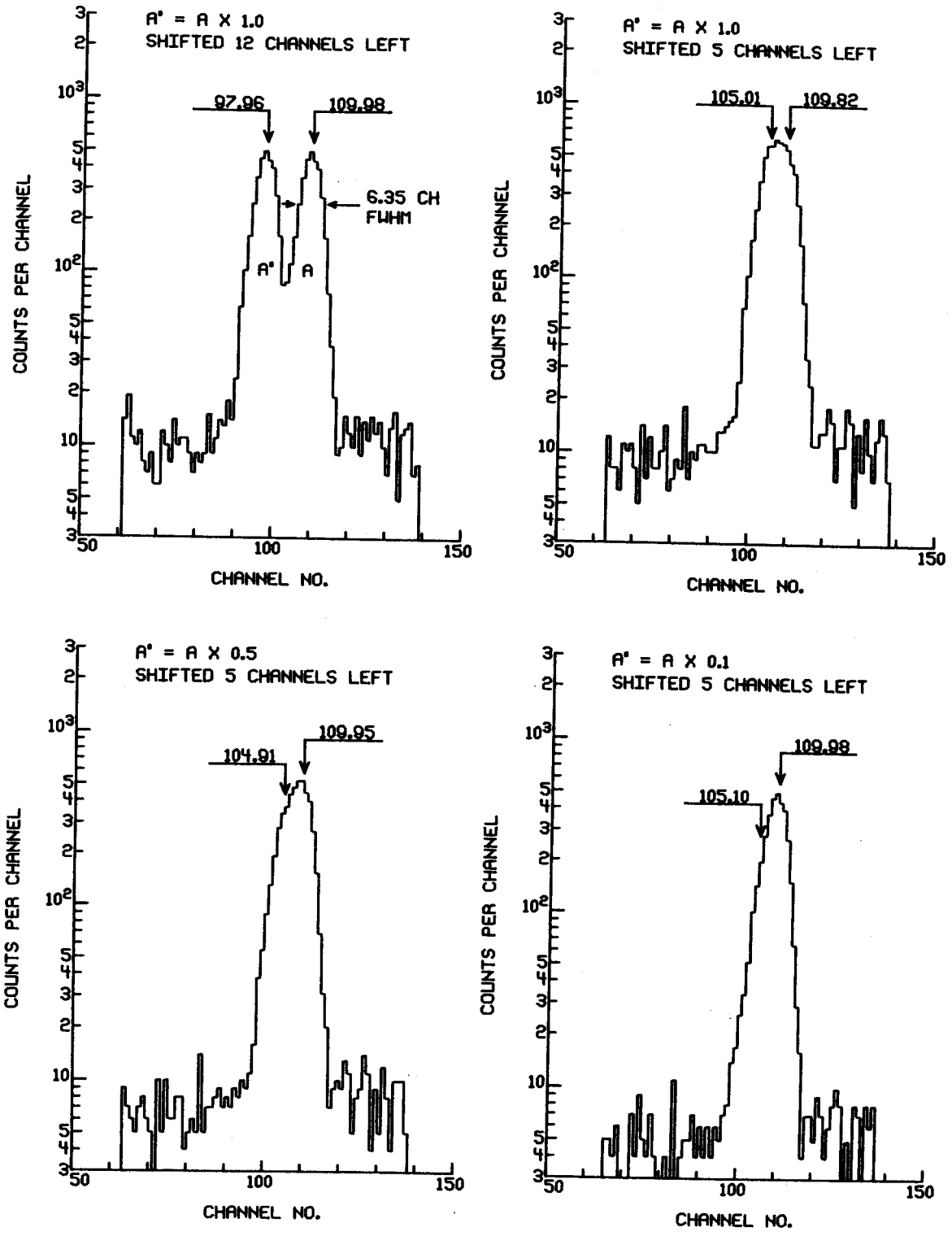

FIGURE 13. Pseudo spectra of the type used to test SAMPO. Arrows indicate centroids as assigned by SAMPO.

The effect of changing the f.w.h.m. fitting parameter by 5% was explored. For the test spectra with a 1.0 scale factor, the doublet was not separated to 1% until the centroids separation reached 6 channels. For the spectra with 0.1 scale factor, the smaller peak was underestimated by 20% for a centroid separation of 6 channels. Changing the tail shape paramenters by 20% had little effect. Since the centroids of the 7.97 MeV and the 8.06 MeV states should have been separated by about 6 channels, these results were used to assign errors to their intensities.

3.2.4 Reactions in the Detector and the 6.44 MeV State Angular Distribution

The 6.44 MeV state is as weak as the 2.31 MeV state and its peak is over a peak due to inelastic scattering to the 6.27 MeV ^{28}Si state in the detector at forward angles. Unlike the 2.31 MeV case, the detector reaction peak and the peak of interest are not separated at forward angles. K. M. Thomson et al. (Th 67) measured the strength of the reactions induced in silicon detectors for 25 MeV incident protons. These results were used to subtract the counts due to reactions in the detector from the 6.44 MeV peak. The large errors assigned to the forward points of the 6.44 MeV angular distribution reflect the uncertainty involved in this subtraction. At 30° in the lab, for example, the sum was about 2400

counts, while the Thomson et al. result led to an estimate of about 1700 counts for the 6.27 MeV reaction in the detector. The energy of the protons reacting with the detector is 29.2 MeV in this experiment and the peak due to the 1.78 MeV reaction in the detector is 30% less in this experiment than in the work of Thomson et al.

3.2.5 Normalization of the Gas Target Data

The gas cell data required long counting periods and were taken in a number of separate runs. It was decided to normalize it to the elastic scattering and take a separate elastic angular distribution measurement. This procedure introduces an additional normalization error, mainly due to uncertainty in reproducing scattering angles. This is most critical at forward angles, but the forward angle data were taken during the same run as the normalization data. Thus the reproducibility of these angles was good to .1°. For most other angles except those around 80° this was a less critical factor, and the uncertainty in reproducing angles was taken as $\pm$ 0.3°. This lead to an uncertainty in the cross sections which was at most 2.8% and which was added in quadrature to the other uncertainties. The absolute level of the 29.8 MeV data was also checked using the same setup used to obtain an absolute normalization for the 36.6 and 40.0 MeV data (see section 3.3.4).

3.3 Reduction of the Position-Sensitive Detector Data

3.3.1 Description of Difficulties

The solid state position sensitive detector data were taken relative to a Si (Li) solid state monitor detector for point to point normalization and absolute normalization was by gas target runs (see section 3.3.4). There were a number of problems in stripping the data. The position sensitive detector was not linear over its entire length and there were regions where its efficiency dropped. Thus in taking data, one not only had to make certain that the detector was at the right height in the focal plane but one also had to map out the areas of constant efficiency and reasonable linearity. The efficiency was mapped by varying the spectrograph field to move a peak along the detector and noting the ratio of counts in the peak to monitor counts at each stop. Thus areas of poor efficiency were noted and avoided. The linearity of the detector was measured well enough to make a first order correction to the background by looking at slit scattering which was assumed to be constant across the face of the detector.

The best data taken was the evaporated melamine target data. The errors on the points in the relative angular distributions of these data are less than 5%. The peaks were narrow and easily kept on the "good" part of the detector,

background subtraction uncertainties were minimal, and the monitor spectra of high quality. A number of the points were retaken during the run and data at 30^{o} was taken several times as a safety measure. Data of this high quality was taken at 29.8 and 36.6 MeV to check the data taken earlier. In each case the agreement was within the errors assigned.

The peak to valley ratio at 30° in the lab for the 36.6 MeV incident proton, 2.31 MeV state data was 12 to 1 with the slurry target and 40 to 1 with the evaporated melamine target. This compares to 1.5 to 1 for the gas target data at 30° in the lab and 29.8 MeV incident protons.

3.3.2 Background Subtraction

Only the 36.6 MeV slurry target data presented any background subtraction problem. Since the slurry target had many large grains it had many spots that were quite thick and the peaks in these data are spread out. Backgrounds were drawn for the spectra as taken and after the background on each side of the peak were corrected for the non-linearity of the detector. The results were averaged and the difference included in the error. For the data taken with the evaporated melamine targets the peaks were narrower and the background could be subtracted directly.

3.3.3 Point to Point Normalization

Point to point normalization was by a 5 mm Si (Li) detector used in conjunction with hardware and electronics described earlier (see section 2.2.9). For the 36.6 MeV slurry target data the monitor spectra began to deteriorate toward the end of the run. The monitor detector had been damaged by γ-rays and neutrons from the Faraday cup and there was no replacement available. The channel "0" scalar, the stripped monitor spectra, and beam on target corrected for changes in target angle were all compared. The percent difference between the channel "0" scalar and the stripped monitor counter spectra, which was as high as 5%, were included in the uncertainties reported. For all the later data an improved monitor detector holder was used and the channel "0" and the stored monitor spectra agreed to within 2%.

3.3.4 Absolute Normalization

Absolute normalization of the spectrograph data was done by measuring the ^{14}N elastic mass section at certain points using a gas target and collimator system described earlier (see sections 2.2.1 to 2.2.8).

Use was made of the fact that the elastic angular distribution was least dependent on angle at about 55° in the lab. The measurement error in the absolute cross section due to local heating in the gas caused by the beam 1%;

due to pressure measurements was 0.3%; due to temperature measurements, 0.2%; due to beam current integration, 2%; and due to collimator dimension measurements, 2%. Corrections for reactions in the absorber of + 0.8% ± 0.3% at 36.6 MeV and 1.3 ± 0.3% at 40.0 MeV were made. A 1.7 ± 0.3% correction was added for counts lost due to nuclear reactions in the silicon detector (Ca 70). The error in the absolute level of the angular distributions should be less than 4% for the 36.6 and 40.0 MeV data.

3.4 Summary of Error Determination

3.4.1 29.8 MeV Gas Cell Data

In assigning errors to the points of the relative angular distributions taken with a gas target at 29.8 MeV, the following sources of error were considered; statistical uncertainty in the number of counts in a peak ($\sqrt{2\,N + B}$ where N is the net number of counts in the peak and B is the number of background counts under the peak), statistical uncertainty in the number of counts in the elastic peak in the spectrum, statistical uncertainty in the number of counts in the elastic peak of the normalization run, the error due to angle non-reproducibility in the normalization run, uncertainty in determining the background, the error involved in separating peaks not completely resolved and in subtracting

contaminant peaks, and the error involved in subtracting peaks due to reactions in the silicon detector. All the above errors were added in quadrature.

3.4.2 Position Sensitive Detector Data

For the position sensitive detector data the errors included were statistical uncertainty in the number of counts in a peak, the uncertainty in determining the background, and the uncertainty in the number of counts in the monitor. The errors in the absolute normalization are the same here as in the gas cell data only an error in the correction for reactions in the aluminum degraders in front of the detectors must be included. This uncertainty was about 0.3%. The overall normalization error is about 4%.

3.5 Plots and Tables of the Angular Distributions.

Plots of all the angular distributions measured for this work are found in Figures(14-32). The data are also tabulated in Tables(3-21). The 2.31 angular distributions plotted as a function of momentum transfer are found in Figure(33) and in Tables(22-25). Where not shown explicitly, the relative errors are smaller than the points.

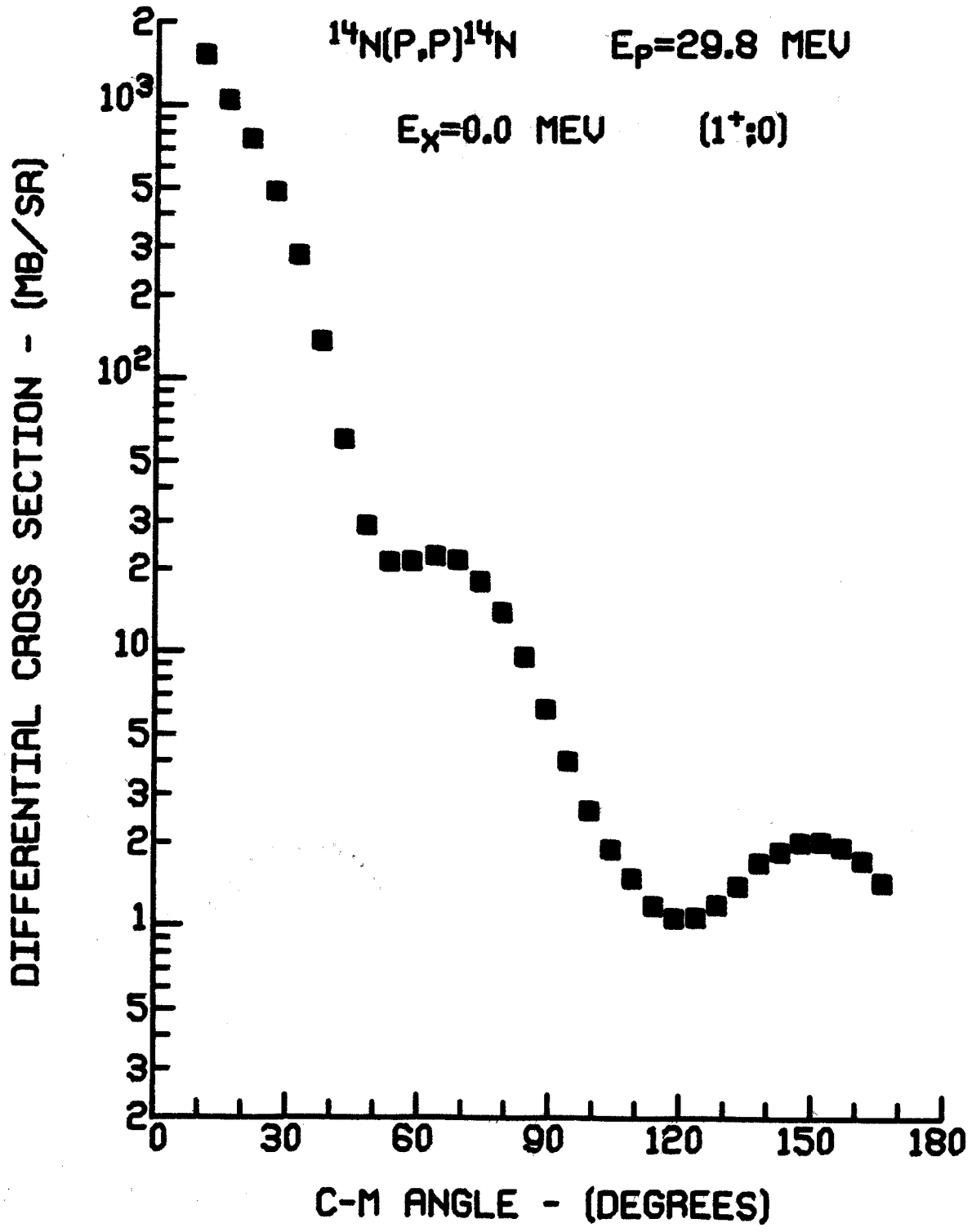

FIGURE 14. $^{14}N(p,p)^{14}N$ angular distribution for E_p = 29.8 MeV. (Where not shown explicitly, the relative errors are smaller than the points.)

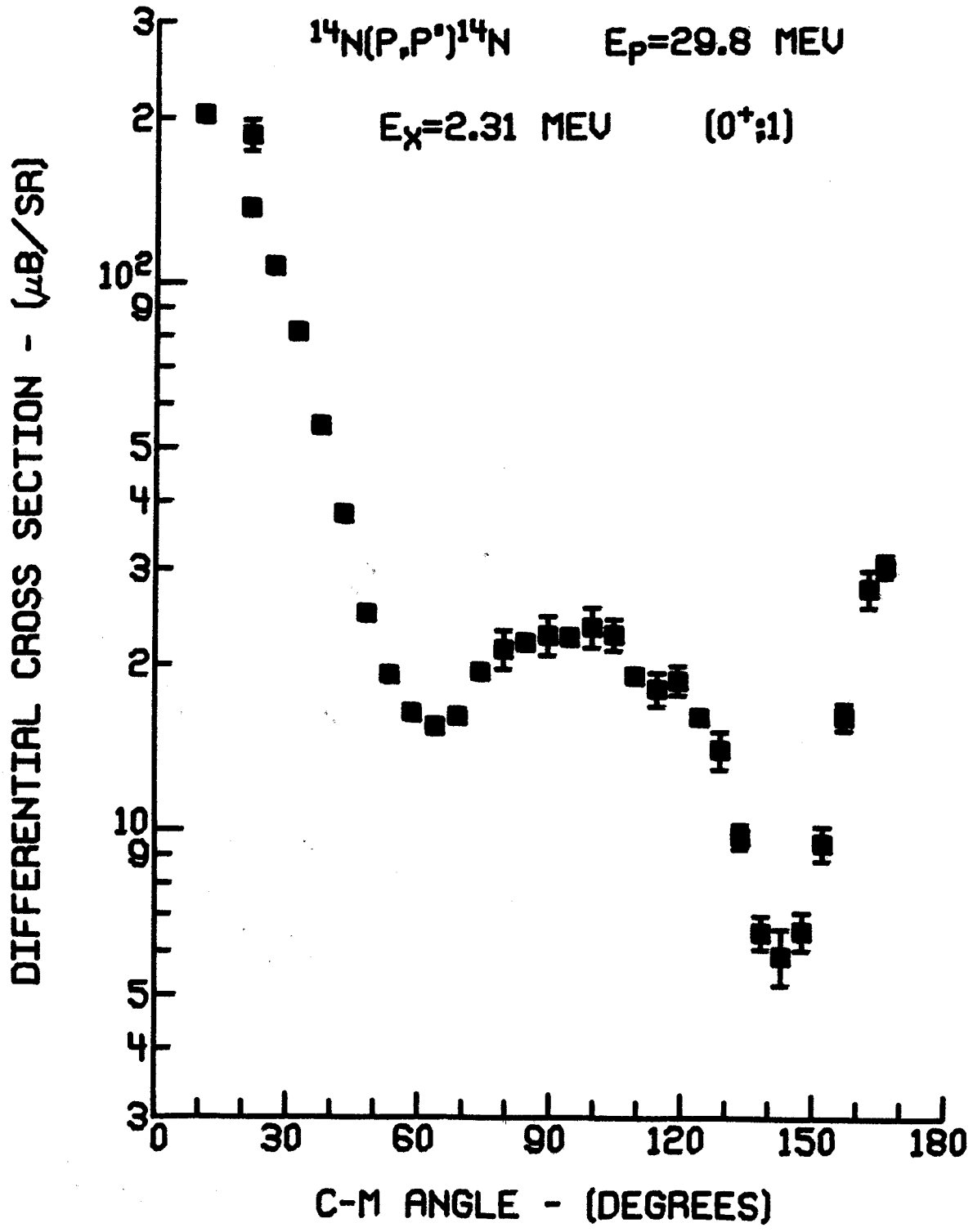

FIGURE 15. $^{14}N(p,p')^{14}N^*$ (2.31 MeV, $(0^+;1)$) angular distribution for E_p = 29.8 MeV. (See caption of Figure 14).

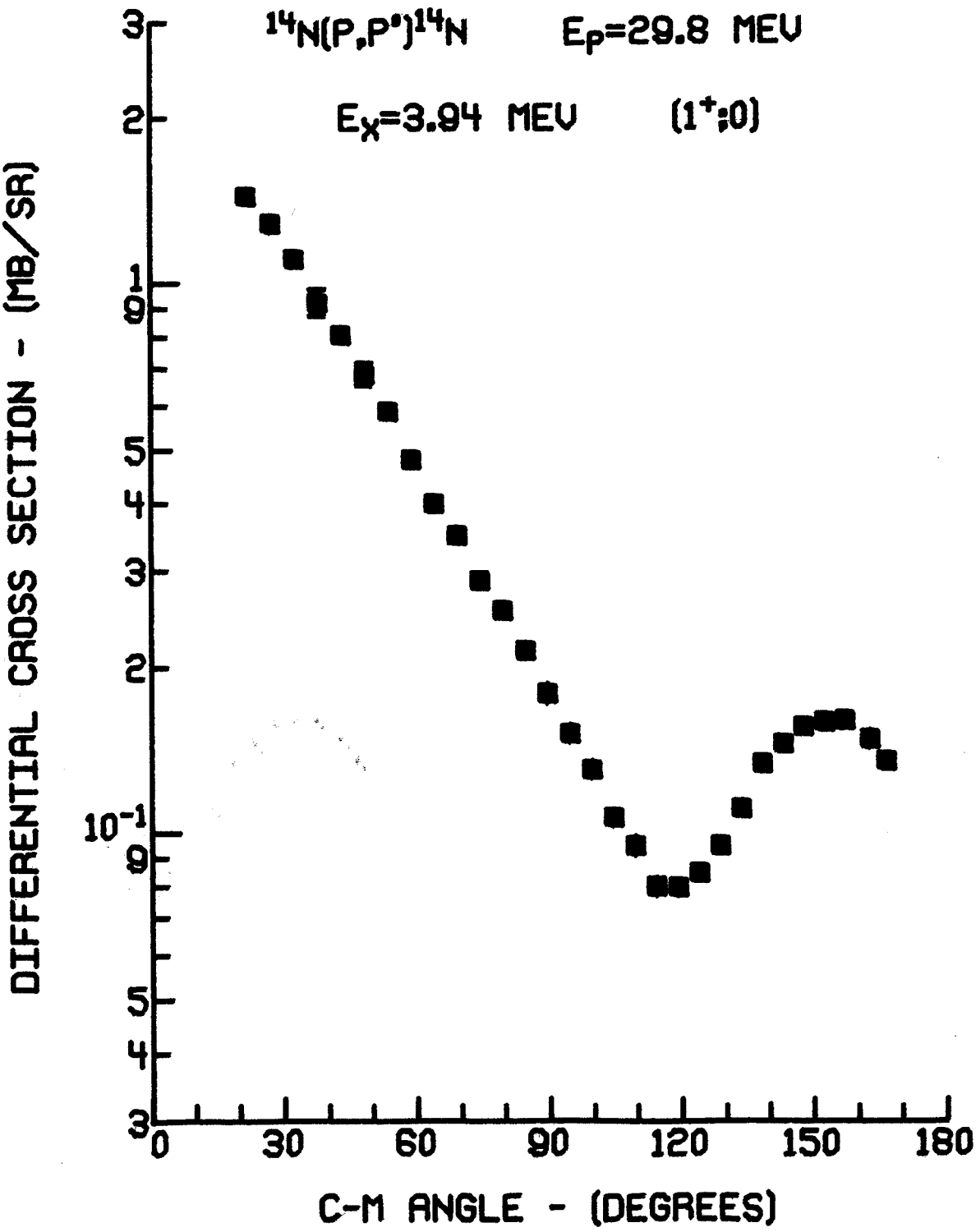

FIGURE 16. $^{14}N(p,p')^{14}N^*$ (3.94 MeV,(1^+;0)) angular distribution for E_p = 29.8 MeV. (See caption of Figure 14.)

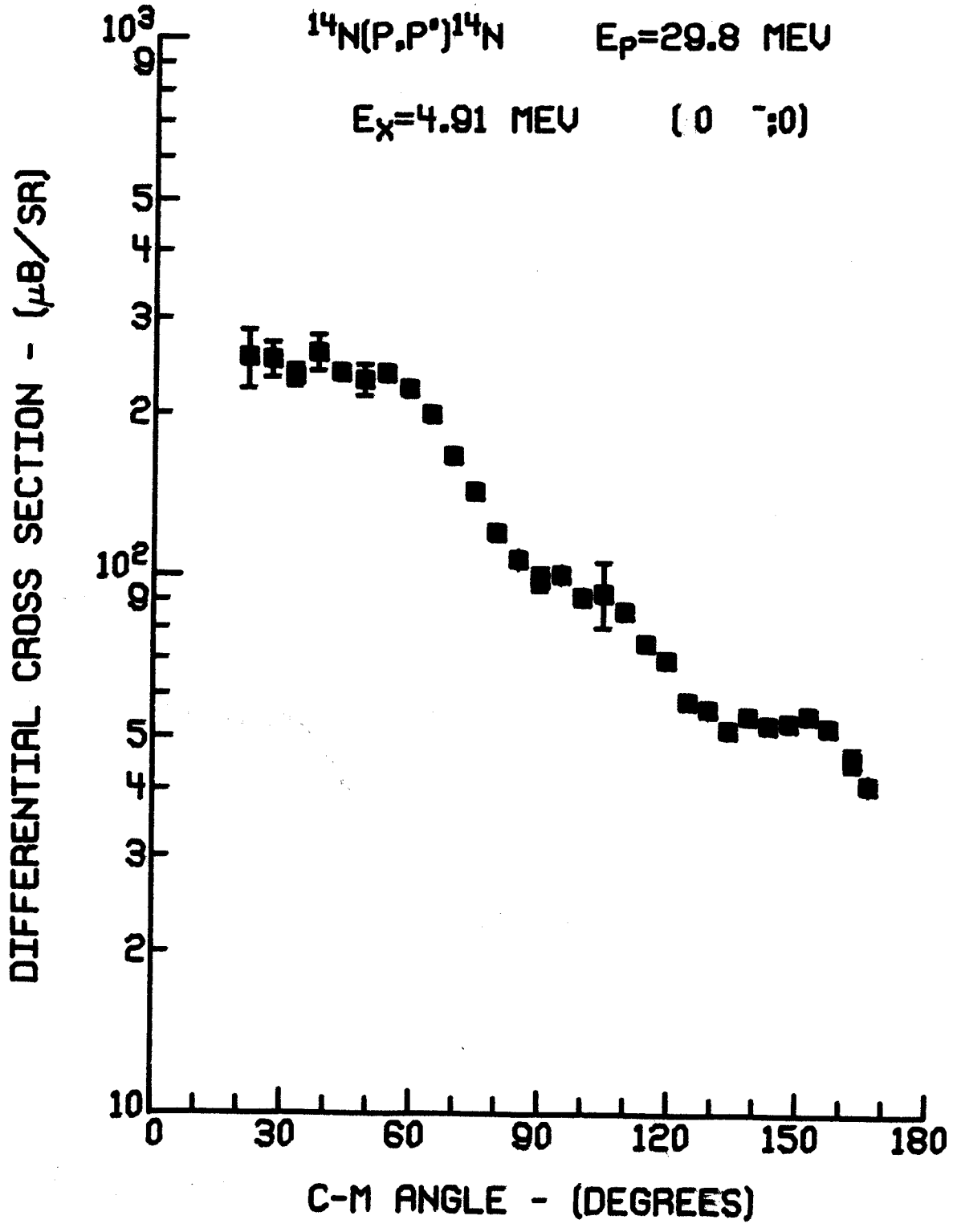

FIGURE 17. $^{14}N(p,p')^{14}N^*$ (4.91 MeV,(0^-;0)) angular distribution for E_p = 29.8 MeV. (See caption of Figure 14.)

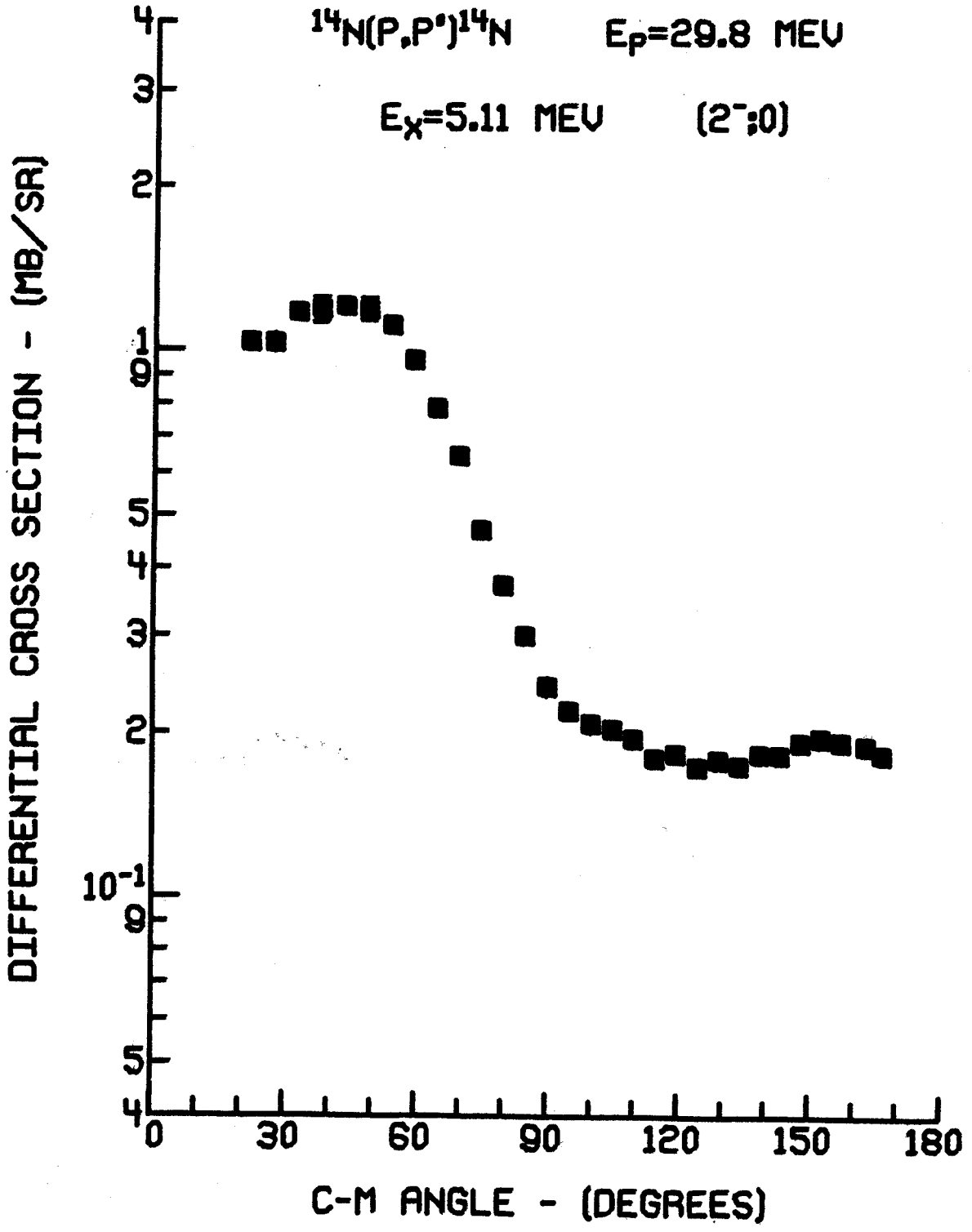

FIGURE 18. $^{14}N(p,p')^{14}N^*$ (5.11 MeV,(2⁻;0)) angular distribution for E_p = 29.8 MeV. (See caption of Figure 14.)

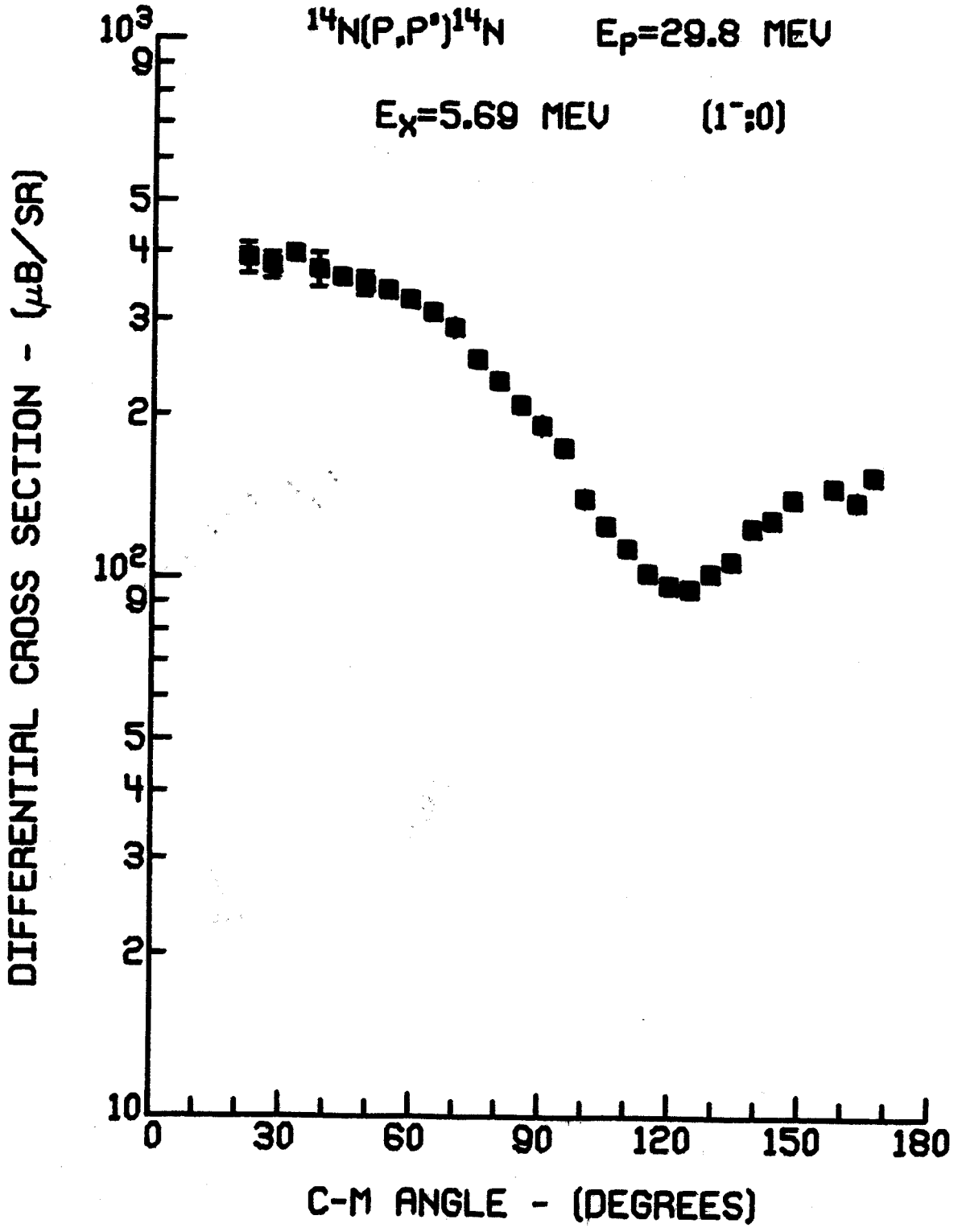

FIGURE 19. $^{14}N(p,p')^{14}N^*$ (5.69 MeV,(1⁻;0)) angular distribution for E_p = 29.8 MeV. (See caption of Figure 14.)

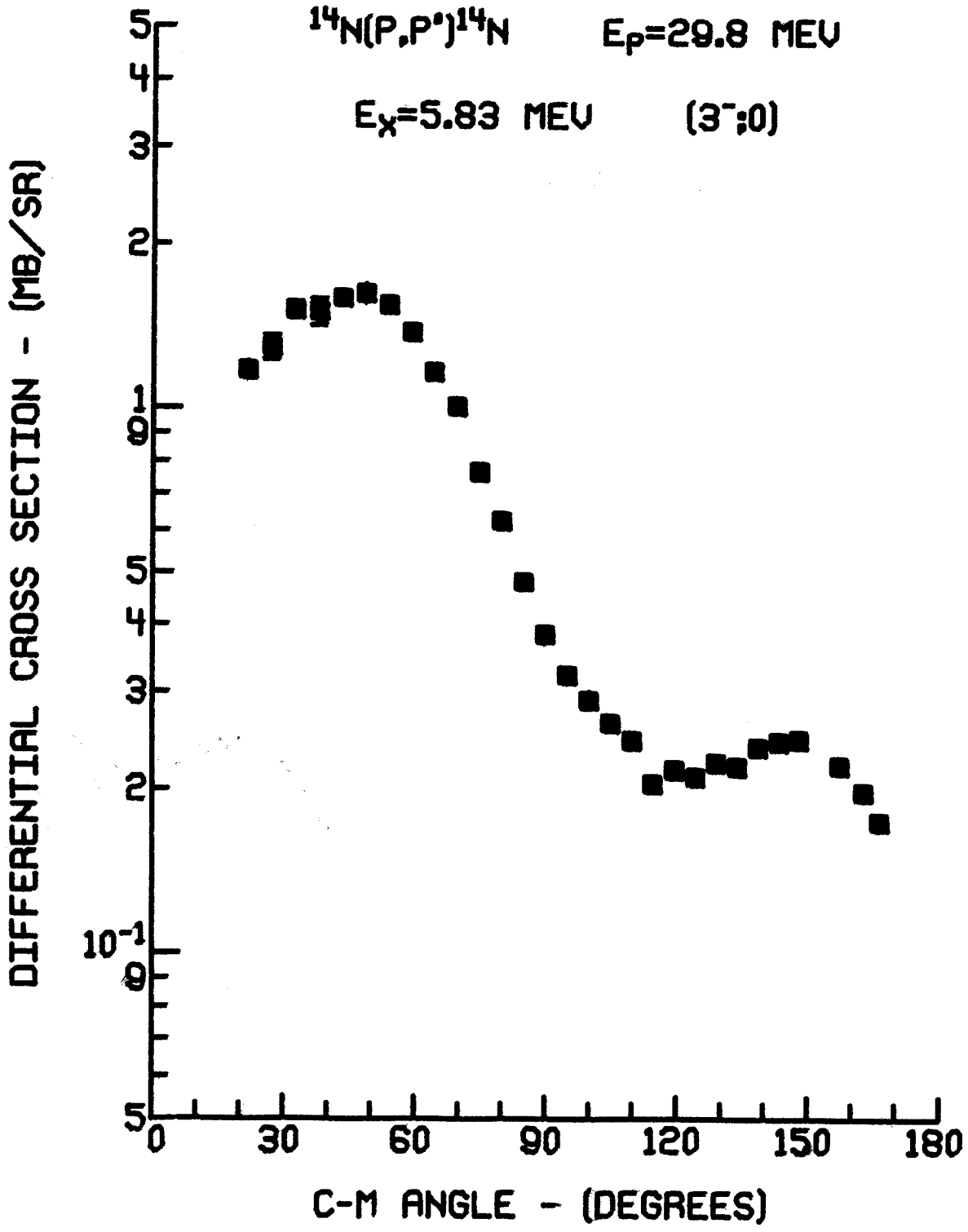

FIGURE 20. $^{14}N(p,p')^{14}N^*$ (5.83 MeV,$(3^-;0)$) angular distribution for E_p = 29.8 MeV. (See caption of Figure 14.)

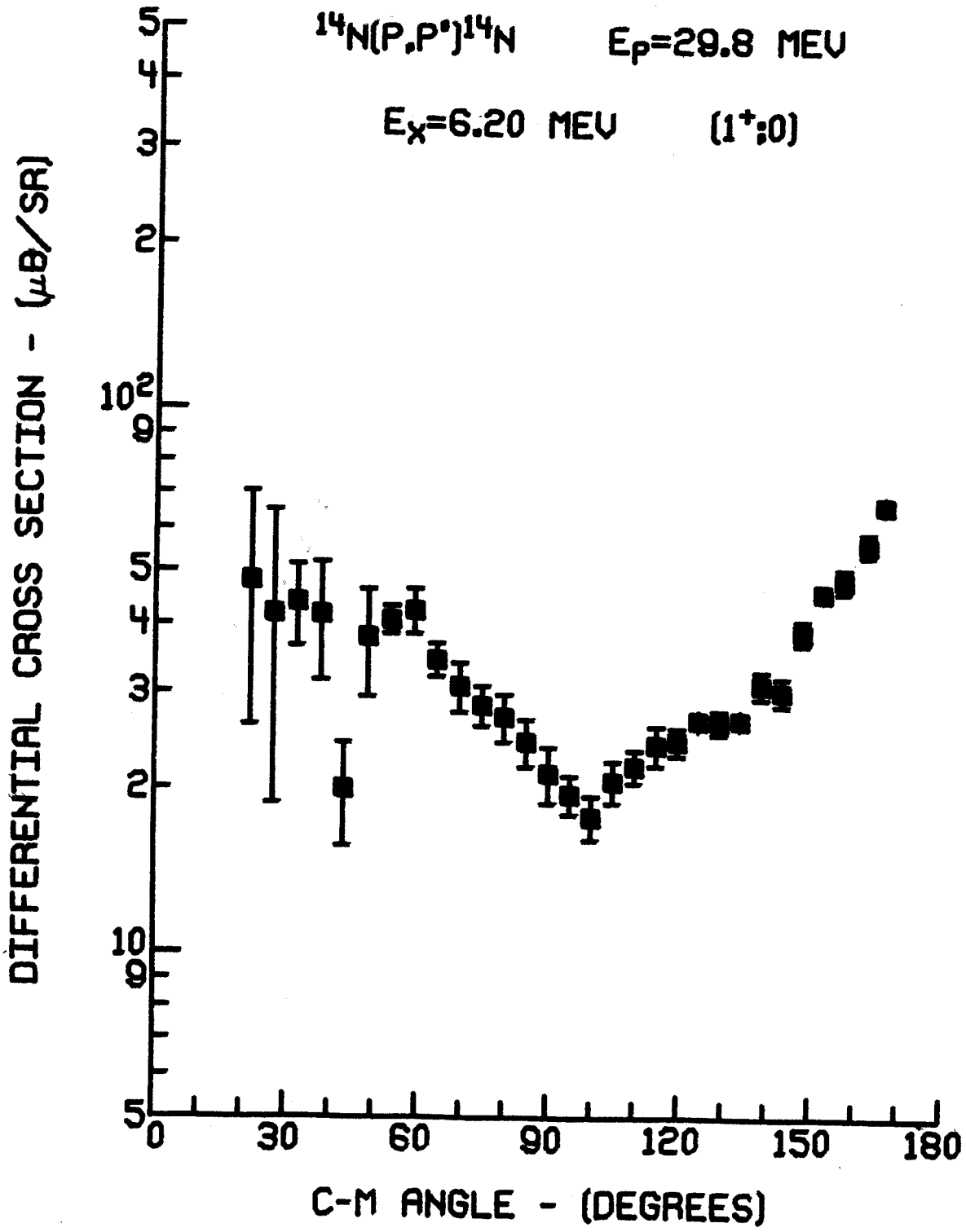

FIGURE 21. $^{14}N(p,p')^{14}N^*$ (6.20 MeV, $(1^+;0)$) angular distribution for E_p = 29.8 MeV. (See caption of Figure 14.)

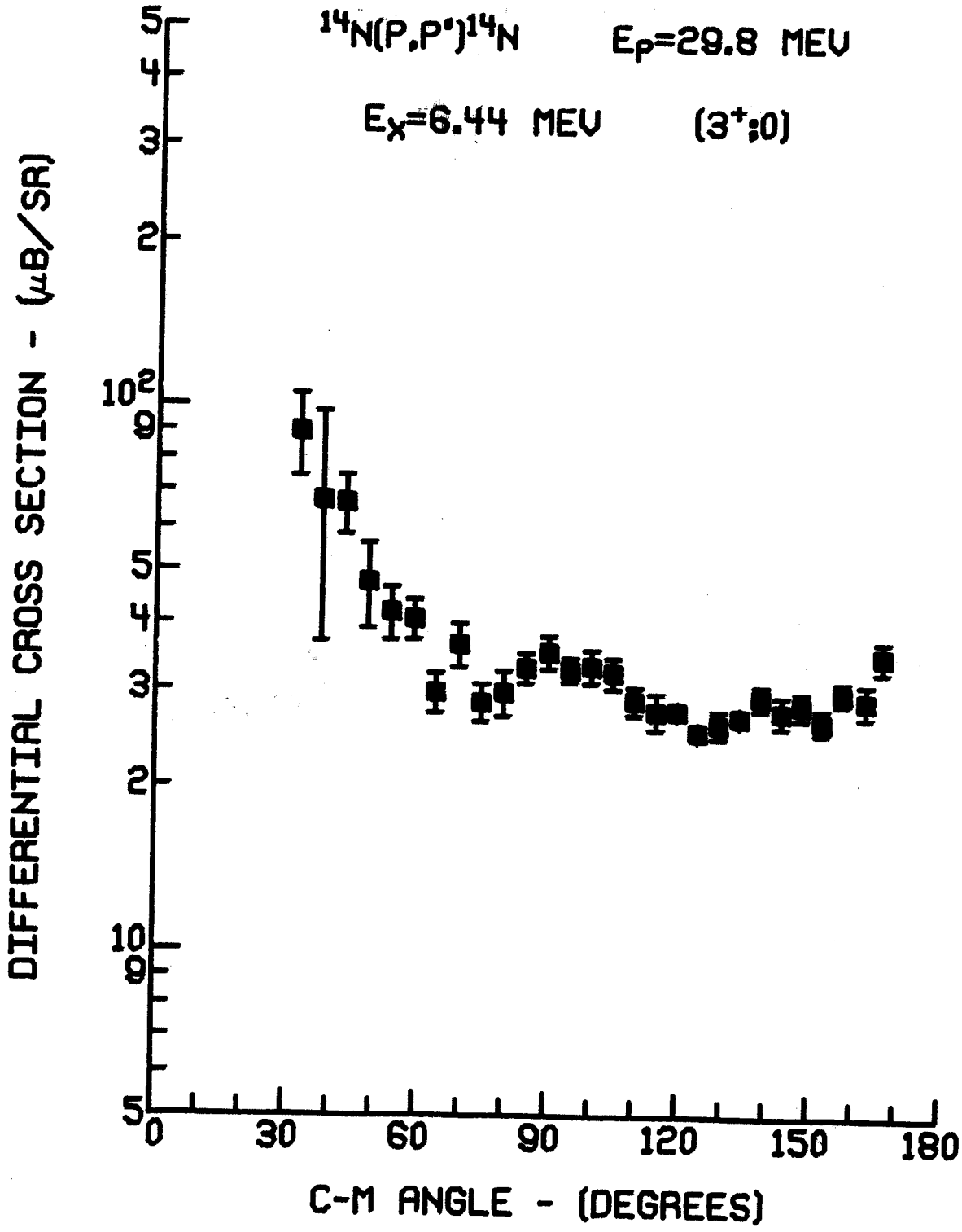

FIGURE 22. $^{14}N(p,p')^{14}N^*$ (6.44 MeV, $(3^+;0)$) angular distribution for E_p = 29.8 MeV. (See caption of Figure 14.)

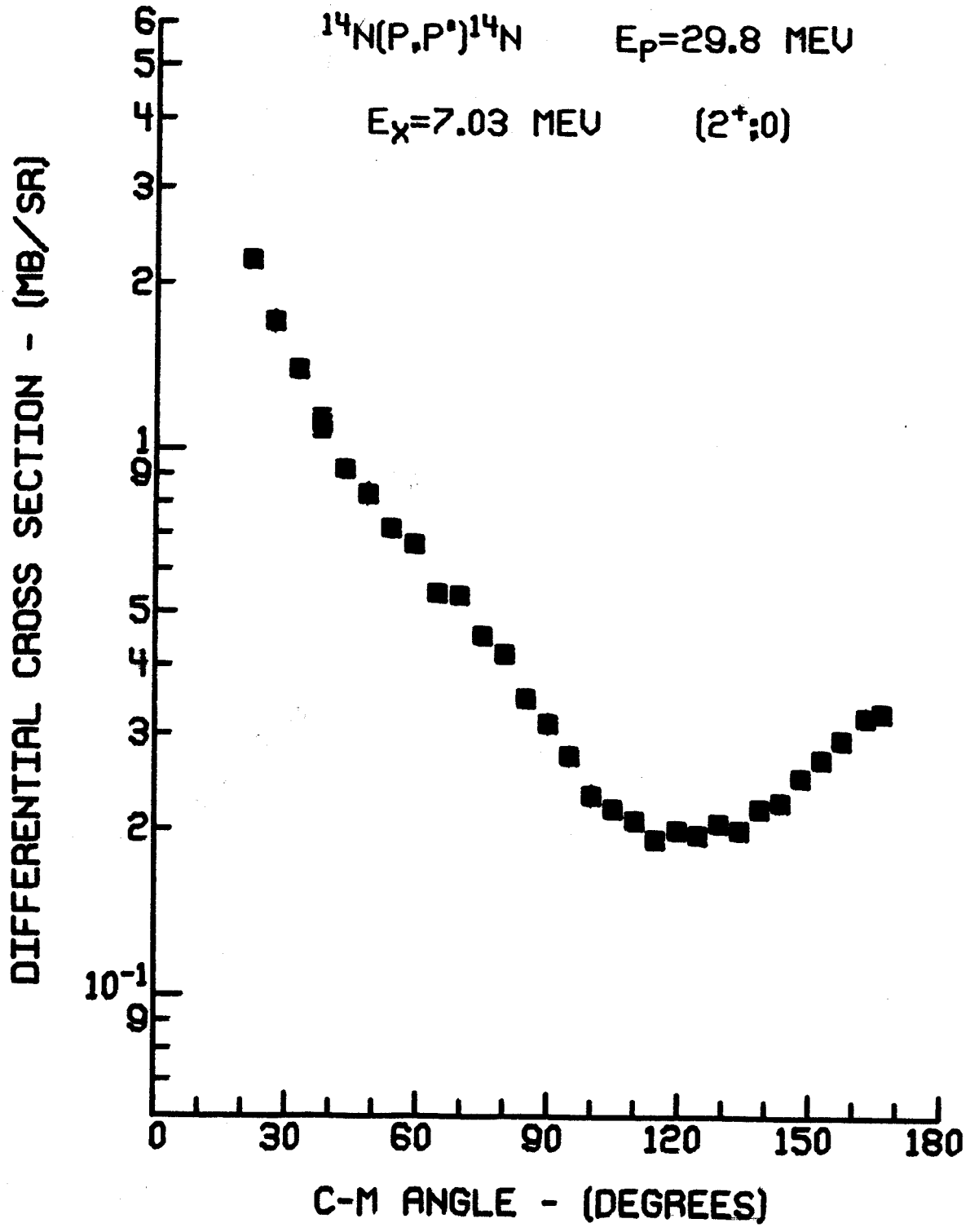

FIGURE 23. $^{14}N(p,p')^{14}N^*$ (7.03 MeV, $(2^+;0)$) angular distribution for E_p = 29.8 MeV. (See caption of Figure 14.)

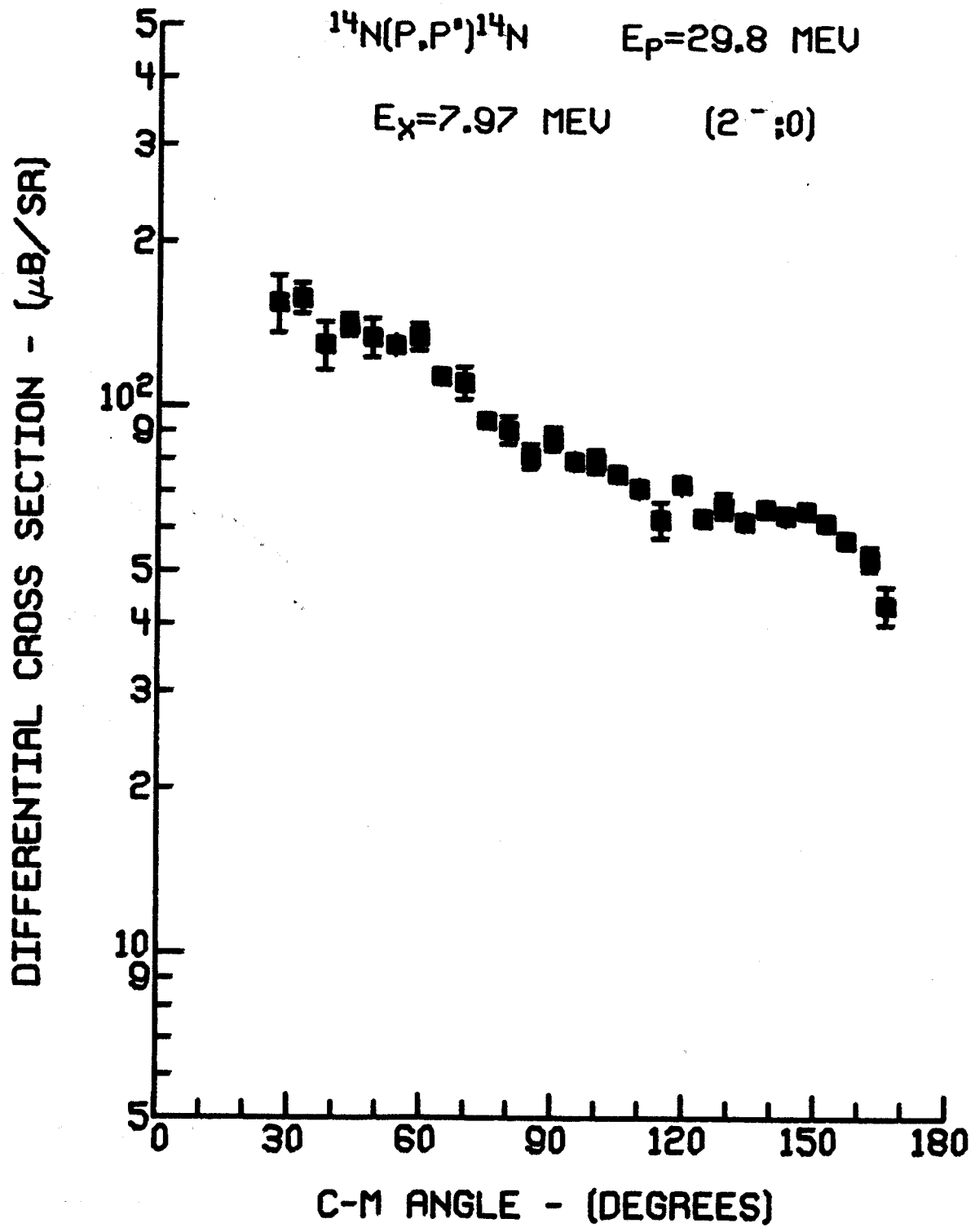

FIGURE 24. $^{14}N(p,p')^{14}N^*$ (7.97 MeV, $(2^-;0)$) angular distribution for E_p = 29.8 MeV. (See caption of Figure 14.)

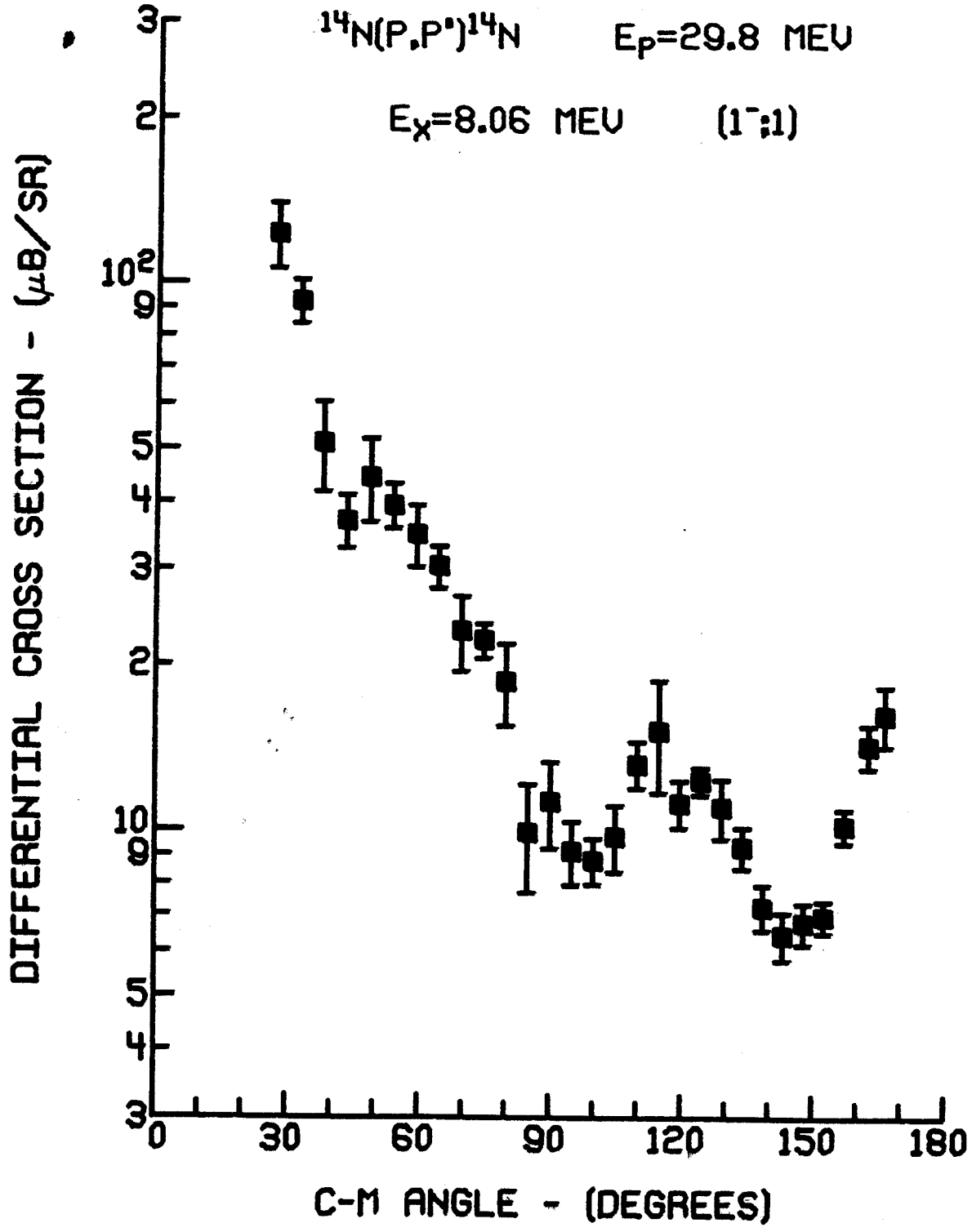

FIGURE 25. $^{14}N(p,p')^{14}N^*$ (8.06 MeV, $(1^-;1)$) angular distribution for E_p = 29.8 MeV. (See caption of Figure 14.)

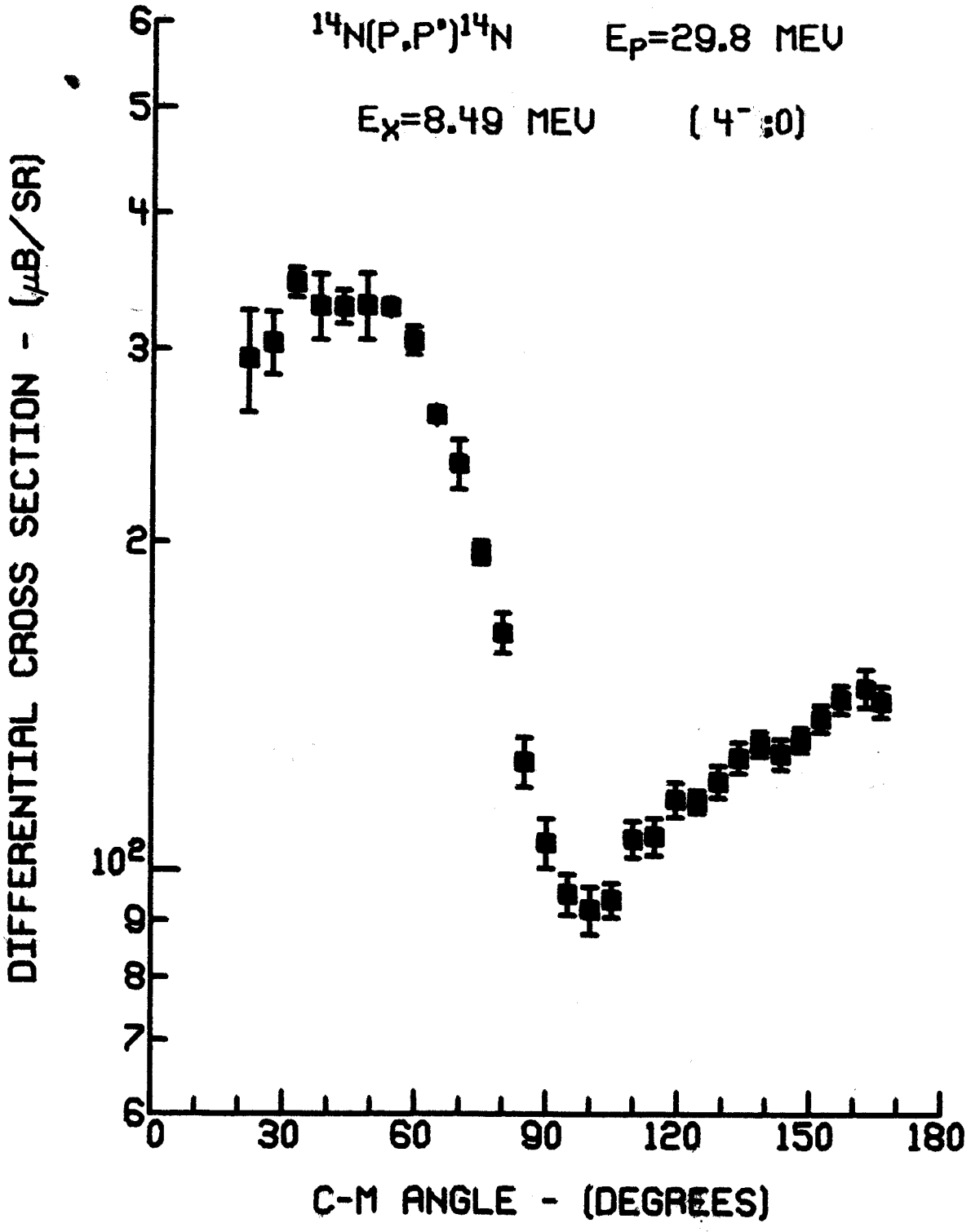

FIGURE 26. $^{14}N(p,p')^{14}N^*$ (8.49 MeV, $(4^-;0)$) angular distribution for E_p = 29.8 MeV. (See caption of Figure 14.)

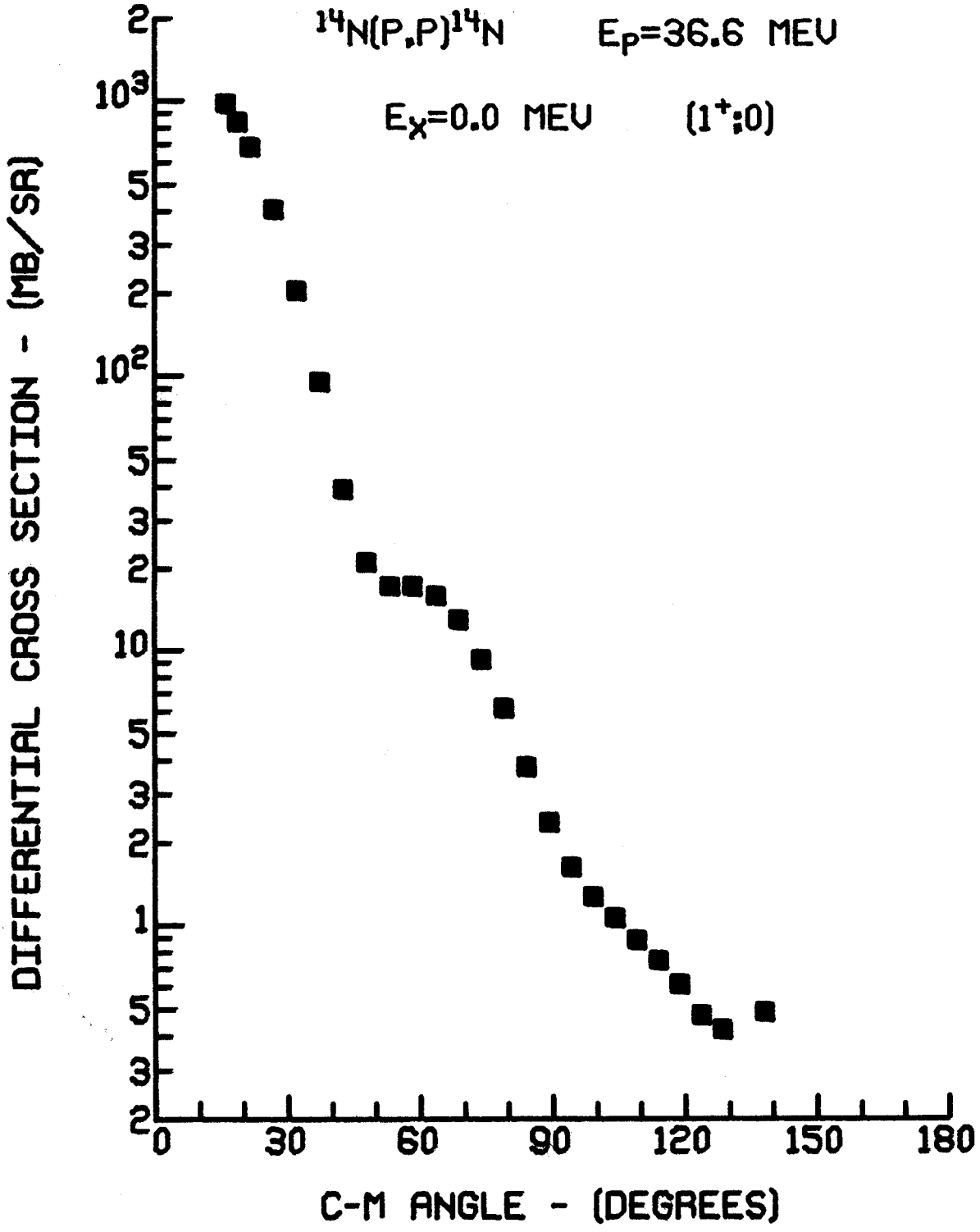

FIGURE 27. $^{14}N(p,p)^{14}N$ angular distribution for E_p = 36.6 MeV. (See caption of Figure 14.)

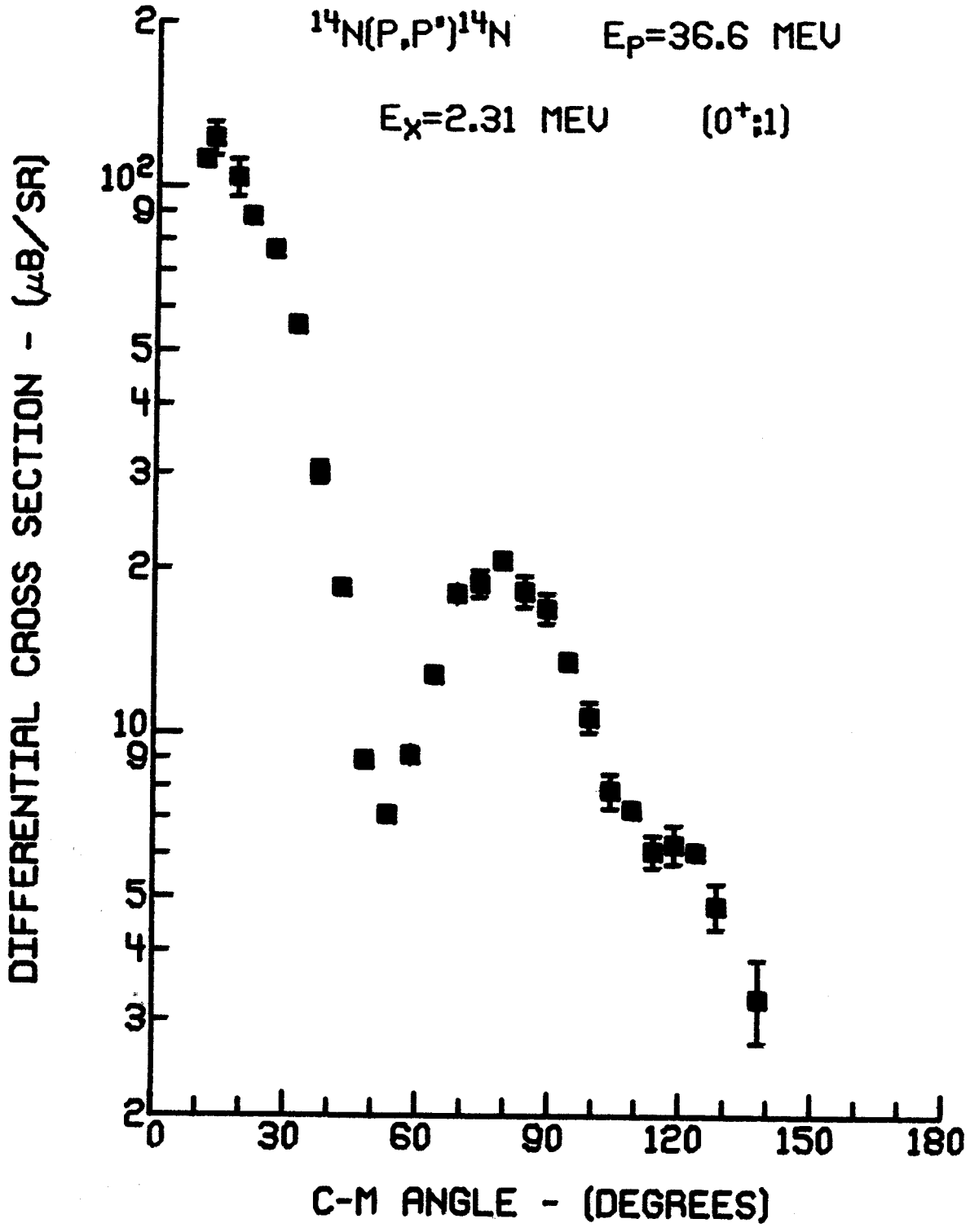

FIGURE 28. $^{14}N(p,p')^{14}N^*$ (2.31 MeV, $(0^+;1)$) angular distribution for E_p = 36.6 MeV. (See caption of Figure 14.)

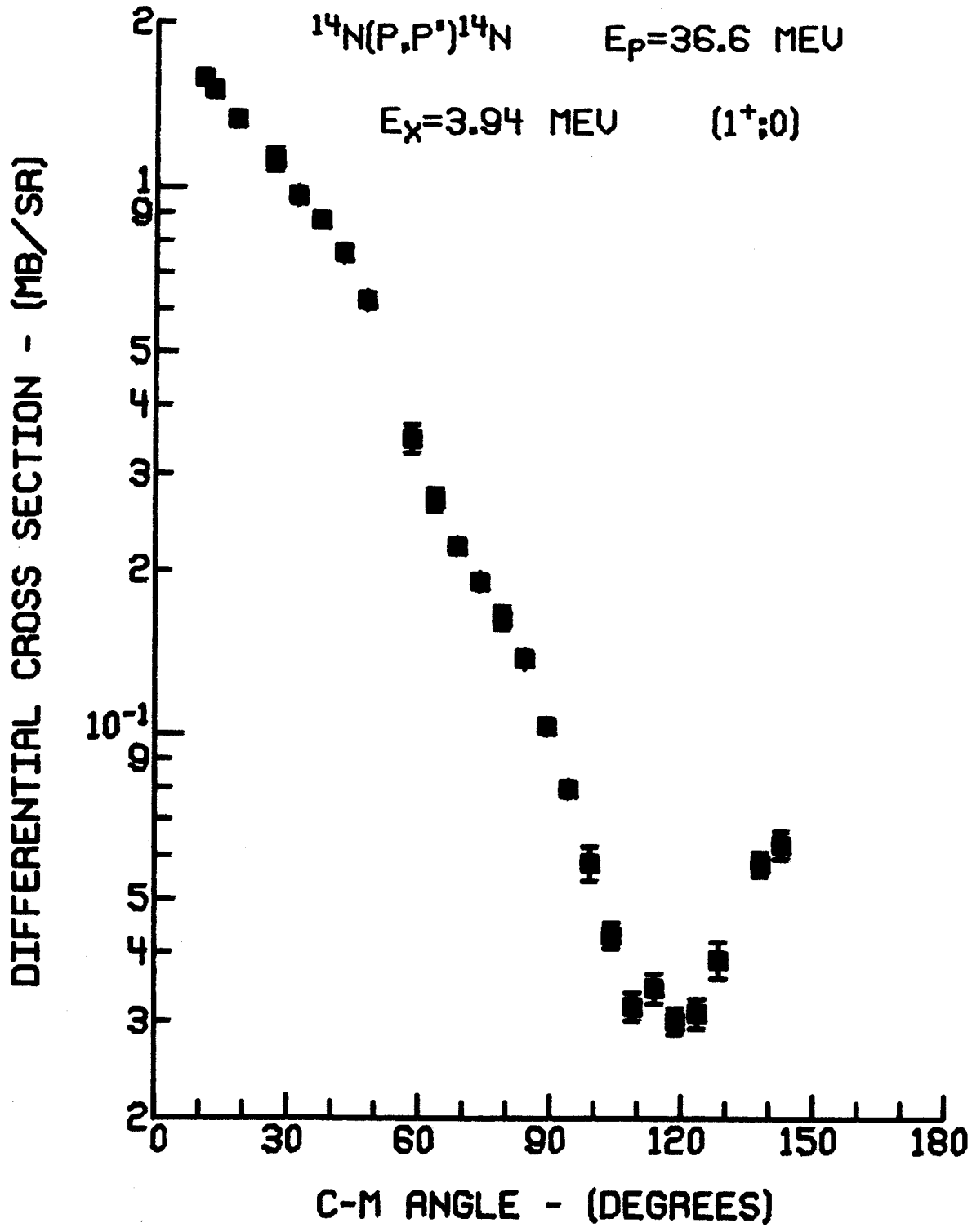

FIGURE 29. $^{14}N(p,p')^{14}N^*$ (3.94 MeV, $(1^+;0)$) angular distribution for E_p = 36.6 MeV. (See caption of Figure 14.)

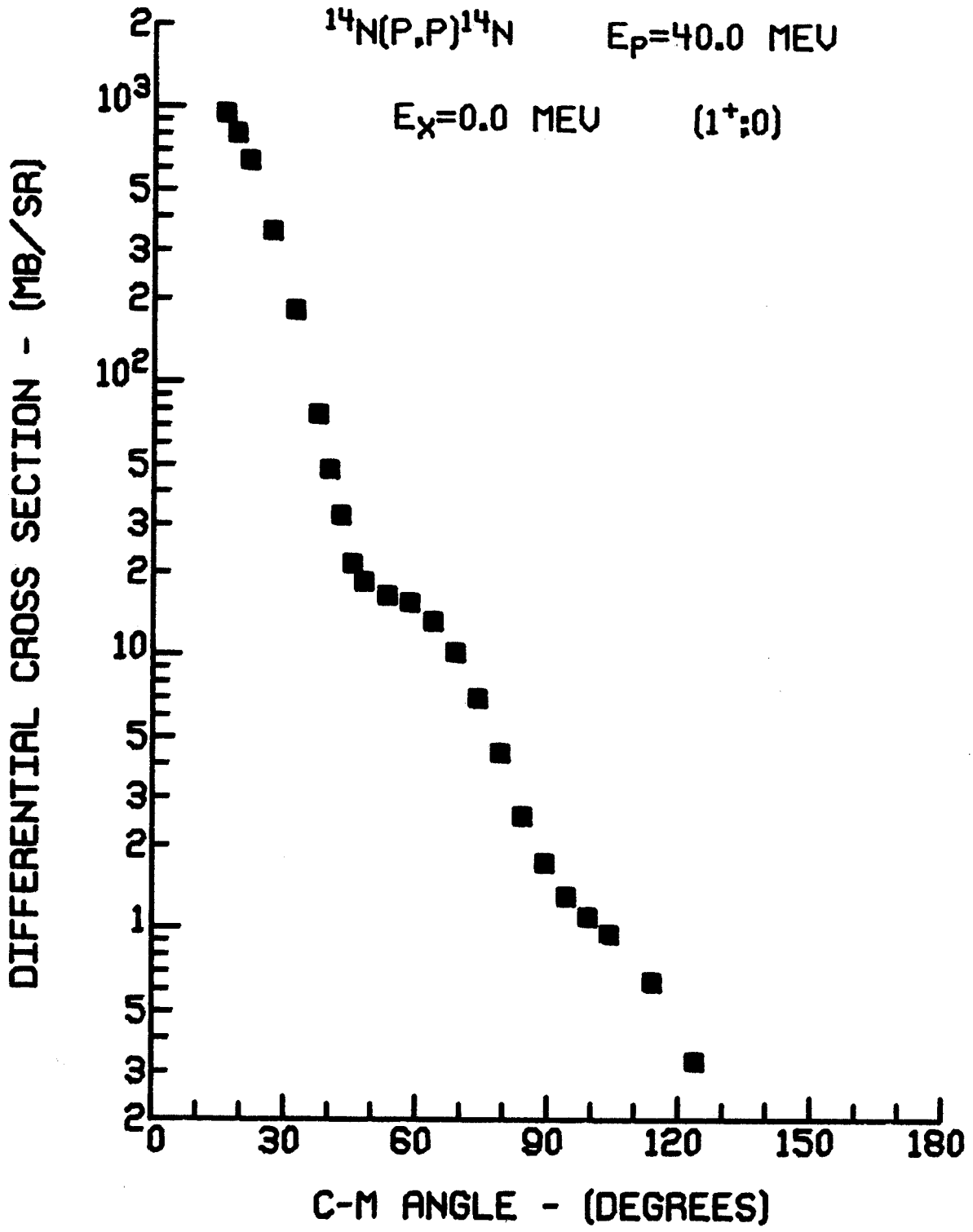

FIGURE 30. $^{14}N(p,p)^{14}N$ angular distribution for E_p = 40.0 MeV. (See caption of Figure 14.)

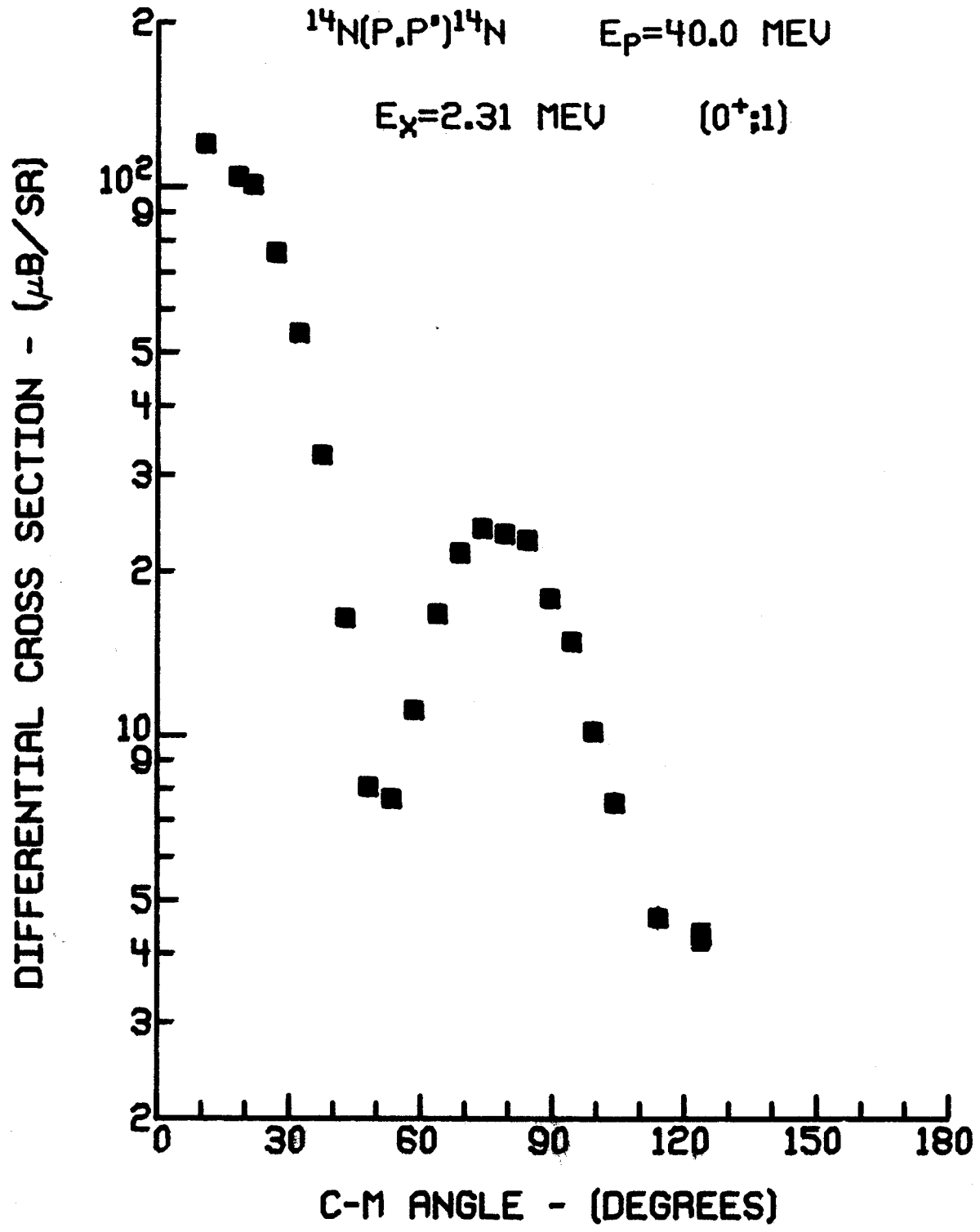

FIGURE 31. $^{14}N(p,p')^{14}N^*$ (2.31 MeV, $(0^+;1)$) angular distribution for E_p = 40.0 MeV. (See caption of Figure 14.)

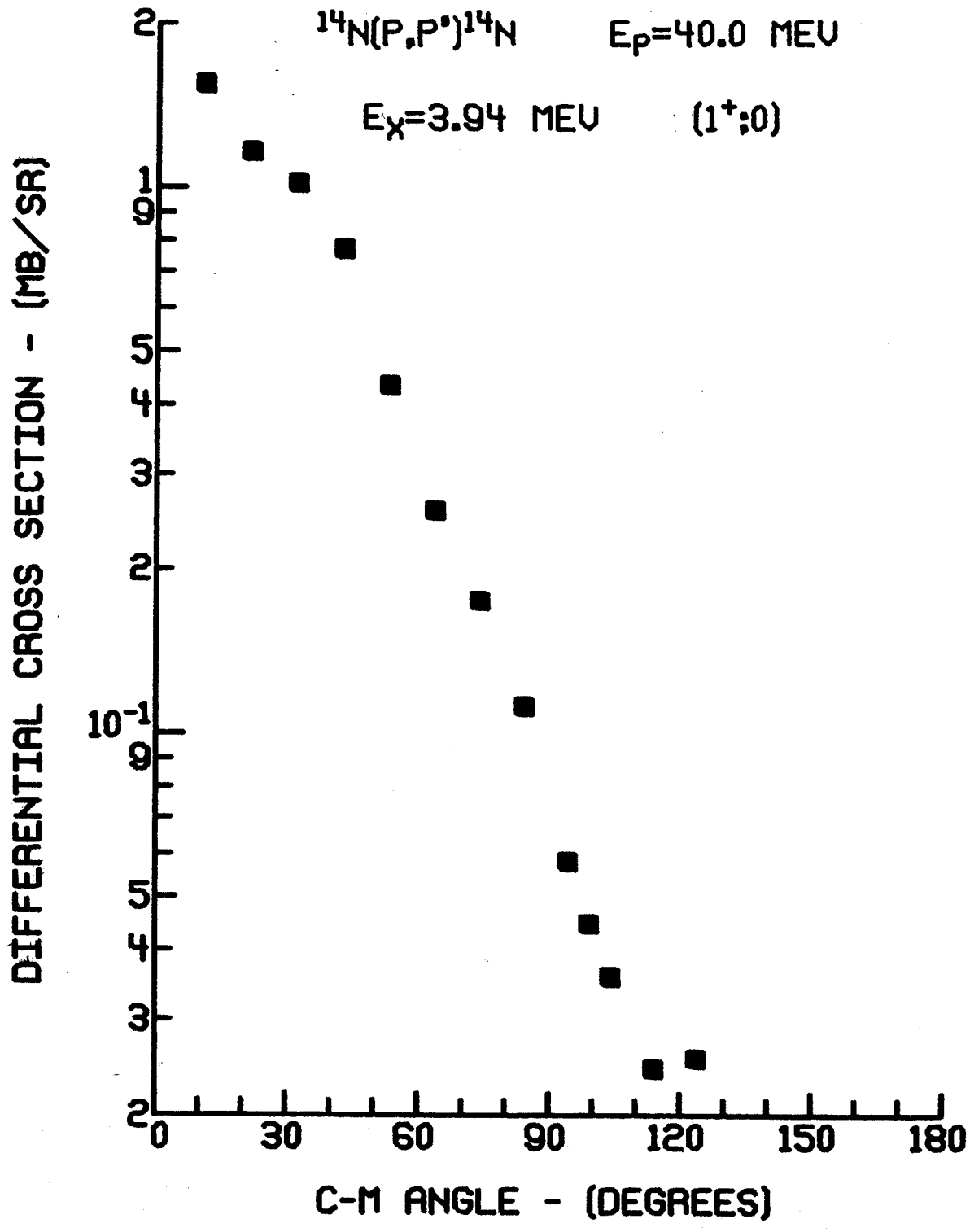

FIGURE 32. $^{14}N(p,p')^{14}N^*$ (3.94 MeV, $(1^+;0)$) angular distribution for E_p = 40.0 MeV. (See caption of Figure 14.)

TABLE 3. $^{14}N(p,p)^{14}N$ elastic scattering, E_p = 29.8 MeV.

C.M. ANGLE (DEG.)	DIFFERENTIAL CROSS SECTION (MB/SR)	LAB. ANGLE (DEG.)	DIFFERENTIAL CROSS SECTION (MB/SR)	RELATIVE PER CENT ERROR	NORM. ERROR
10.73	1.528E+03	10.00	1.757E+03	2.8	4.0
16.09	1.052E+03	15.00	1.207E+03	2.8	4.0
21.44	7.601E+02	20.00	8.685E+02	2.8	4.0
26.78	4.877E+02	25.00	5.546E+02	2.8	4.0
32.11	2.812E+02	30.00	3.179E+02	2.9	4.0
37.42	1.371E+02	35.00	1.540E+02	2.8	4.0
42.71	6.049E+01	40.00	6.743E+01	2.9	4.0
47.98	2.915E+01	45.00	3.222E+01	3.0	4.0
53.23	2.130E+01	50.00	2.332E+01	3.0	4.0
58.45	2.143E+01	55.00	2.337E+01	2.9	4.0
63.65	2.245E+01	60.00	2.408E+01	2.9	4.0
68.82	2.172E+01	65.00	2.304E+01	3.0	4.0
73.96	1.810E+01	70.00	1.897E+01	2.9	4.0
79.07	1.401E+01	75.00	1.451E+01	3.1	4.0
84.15	9.662E+00	80.00	9.884E+00	3.0	4.0
89.19	6.243E+00	85.00	6.305E+00	3.3	4.0
94.21	4.010E+00	90.00	3.999E+00	3.1	4.0
99.19	2.637E+00	95.00	2.596E+00	3.4	4.0
104.14	1.901E+00	100.00	1.848E+00	3.1	4.0
109.06	1.483E+00	105.00	1.423E+00	3.4	4.0
113.95	1.181E+00	110.00	1.119E+00	3.2	4.0
118.81	1.072E+00	115.00	1.005E+00	3.3	4.0
123.64	1.076E+00	120.00	9.963E-01	3.4	4.0
128.44	1.198E+00	125.00	1.097E+00	3.4	4.0
133.22	1.405E+00	130.00	1.273E+00	3.5	4.0
137.97	1.707E+00	135.00	1.532E+00	3.4	4.0
142.70	1.868E+00	140.00	1.662E+00	3.4	4.0
147.41	2.029E+00	145.00	1.818E+00	3.4	4.0
152.10	2.046E+00	150.00	1.793E+00	3.4	4.0
156.77	1.954E+00	155.00	1.702E+00	3.4	4.0
161.44	1.743E+00	160.00	1.511E+00	3.4	4.0
166.09	1.452E+00	165.00	1.254E+00	3.3	4.0

TABLE 4. $^{14}N(p,p')^{14}N^*$ (2.31,(0^+;1)), E_p = 29.8 MeV.

C.M. ANGLE (DEG.)	DIFFERENTIAL CROSS SECTION (MB/SR)	LAB. ANGLE (DEG.)	DIFFERENTIAL CROSS SECTION (MB/SR)	RELATIVE PER CENT ERROR	NORM. ERROR
10.73	2.036E-01	10.00	2.341E-01	2.2	4.0
21.44	1.372E-01	20.00	1.568E-01	1.8	4.0
21.50	1.867E-01	20.10	2.145E-01	6.6	4.0
26.78	1.074E-01	25.00	1.222E-01	1.7	4.0
32.11	8.157E-02	30.00	9.223E-02	1.1	4.0
37.42	5.490E-02	35.00	6.167E-02	3.3	4.0
42.71	3.793E-02	40.00	4.228E-02	2.2	4.0
47.98	2.492E-02	45.00	2.755E-02	3.1	4.0
53.23	1.923E-02	50.00	2.106E-02	2.3	4.0
58.45	1.636E-02	55.00	1.774E-02	3.1	4.0
63.65	1.549E-02	60.00	1.661E-02	2.7	4.0
68.82	1.616E-02	65.00	1.714E-02	3.4	4.0
73.96	1.950E-02	70.00	2.045E-02	2.3	4.0
79.24	2.144E-02	75.00	2.224E-02	3.2	4.0
84.15	2.208E-02	80.00	2.259E-02	2.7	4.0
89.37	2.279E-02	85.00	2.303E-02	3.3	4.0
94.21	2.260E-02	90.00	2.254E-02	2.4	4.0
99.37	2.358E-02	95.00	2.319E-02	3.5	4.0
104.32	2.283E-02	100.00	2.216E-02	6.7	4.0
109.06	1.916E-02	105.00	1.839E-02	2.6	4.0
114.12	1.812E-02	110.00	1.713E-02	7.2	4.0
118.97	1.883E-02	115.00	1.759E-02	6.4	4.0
123.80	1.610E-02	120.00	1.485E-02	3.8	4.0
128.59	1.401E-02	125.00	1.278E-02	7.9	4.0
133.36	9.766E-03	130.00	8.812E-03	5.3	4.0
138.10	6.526E-03	135.00	5.830E-03	7.1	4.0
142.82	5.906E-03	140.00	5.227E-03	11.7	4.0
147.51	6.572E-03	145.00	5.769E-03	8.0	4.0
152.19	9.519E-03	150.00	8.293E-03	7.2	4.0
156.85	1.617E-02	155.00	1.400E-02	5.8	4.0
162.43	2.789E-02	161.00	2.400E-02	7.8	4.0
166.13	3.066E-02	165.00	2.629E-02	4.8	4.0

TABLE 5. $^{14}N(p,p')^{14}N^*$ (3.94,(1^+;0)), E_p = 29.8 MeV.

C.M. ANGLE (DEG.)	DIFFERENTIAL CROSS SECTION (MB/SR)	LAB. ANGLE (DEG.)	DIFFERENTIAL CROSS SECTION (MB/SR)	RELATIVE PER CENT ERROR	NORM. ERROR
21.55	1.441E+00	20.00	1.562E+00	2.6	4.0
26.92	1.282E+00	25.00	1.472E+00	3.9	4.0
32.27	1.108E+00	30.00	1.279E+00	2.3	4.0
37.60	9.216E-01	35.00	1.044E+00	5.5	4.0
42.92	8.041E-01	40.00	9.034E-01	2.9	4.0
48.21	6.838E-01	45.00	7.613E-01	4.6	4.0
53.47	5.854E-01	50.00	6.453E-01	1.7	4.0
58.71	4.792E-01	55.00	5.226E-01	2.2	4.0
63.93	3.981E-01	60.00	4.293E-01	1.4	4.0
69.11	3.475E-01	65.00	3.702E-01	3.2	4.0
74.26	2.876E-01	70.00	3.025E-01	1.8	4.0
79.38	2.540E-01	75.00	2.637E-01	3.2	4.0
84.46	2.143E-01	80.00	2.195E-01	3.6	4.0
89.52	1.793E-01	85.00	1.812E-01	4.4	4.0
94.53	1.518E-01	90.00	1.513E-01	4.1	4.0
99.51	1.304E-01	95.00	1.282E-01	4.2	4.0
104.46	1.063E-01	100.00	1.031E-01	3.7	4.0
109.37	9.471E-02	105.00	9.059E-02	4.2	4.0
114.26	7.969E-02	110.00	7.522E-02	4.1	4.0
119.10	7.948E-02	115.00	7.406E-02	3.5	4.0
123.92	8.461E-02	120.00	7.786E-02	2.1	4.0
128.71	9.478E-02	125.00	8.619E-02	3.6	4.0
133.47	1.106E-01	130.00	1.013E-01	2.4	4.0
138.20	1.339E-01	135.00	1.191E-01	2.8	4.0
142.91	1.455E-01	140.00	1.283E-01	2.9	4.0
147.59	1.564E-01	145.00	1.366E-01	2.6	4.0
152.26	1.597E-01	150.00	1.385E-01	2.6	4.0
156.91	1.604E-01	155.00	1.382E-01	2.8	4.0
162.47	1.486E-01	161.00	1.272E-01	4.0	4.0
166.17	1.352E-01	165.00	1.153E-01	3.0	4.0

TABLE 6. $^{14}N(p,p')^{14}N^*(4.91,(0^-;0))$, E_p = 29.8 MeV.

C.M. ANGLE (DEG.)	DIFFERENTIAL CROSS SECTION (MB/SR)	LAB. ANGLE (DEG.)	DIFFERENTIAL CROSS SECTION (MB/SR)	RELATIVE PER CENT ERROR	NORM. ERROR
21.58	2.541E-01	20.00	2.941E-01	12.4	4.0
26.96	2.520E-01	25.00	2.901E-01	7.5	4.0
32.31	2.353E-01	30.00	2.691E-01	4.7	4.0
37.65	2.597E-01	35.00	2.950E-01	7.7	4.0
42.97	2.386E-01	40.00	2.687E-01	3.5	4.0
48.27	2.307E-01	45.00	2.574E-01	6.8	4.0
53.54	2.375E-01	50.00	2.623E-01	2.8	4.0
58.79	2.225E-01	55.00	2.431E-01	3.3	4.0
64.01	1.997E-01	60.00	2.156E-01	1.8	4.0
69.19	1.672E-01	65.00	1.783E-01	3.0	4.0
74.35	1.430E-01	70.00	1.506E-01	2.1	4.0
79.47	1.204E-01	75.00	1.250E-01	3.3	4.0
84.55	1.072E-01	80.00	1.049E-01	4.2	4.0
89.61	9.868E-02	85.00	9.662E-02	4.7	4.0
94.62	1.007E-01	90.00	1.004E-01	3.9	4.0
99.61	9.144E-02	95.00	8.985E-02	3.9	4.0
104.55	9.316E-02	100.00	9.027E-02	13.9	4.0
109.46	8.633E-02	105.00	8.249E-02	3.6	4.0
114.34	7.516E-02	110.00	7.085E-02	3.4	4.0
119.19	6.997E-02	115.00	6.509E-02	3.4	4.0
124.00	5.853E-02	120.00	5.377E-02	2.1	4.0
128.78	5.661E-02	125.00	5.137E-02	3.8	4.0
133.54	5.185E-02	130.00	4.652E-02	2.9	4.0
138.26	5.504E-02	135.00	4.886E-02	2.8	4.0
142.97	5.288E-02	140.00	4.649E-02	2.7	4.0
147.65	5.332E-02	145.00	4.646E-02	3.0	4.0
152.31	5.509E-02	150.00	4.763E-02	2.9	4.0
156.95	5.233E-02	155.00	4.494E-02	3.0	4.0
162.50	4.568E-02	161.00	3.897E-02	4.7	4.0
166.19	4.091E-02	165.00	3.478E-02	4.1	4.0

TABLE 7. $^{14}N(p,p')^{14}N^*(5.11,(2^-;0))$, E_p = 29.8 MeV.

C.M. ANGLE (DEG.)	DIFFERENTIAL CROSS SECTION (MB/SR)	LAB. ANGLE (DEG.)	DIFFERENTIAL CROSS SECTION (MB/SR)	RELATIVE PER CENT ERROR	NORM. ERROR
21.59	1.034E+00	20.00	1.198E+00	3.5	4.0
26.96	1.031E+00	25.00	1.188E+00	4.0	4.0
32.32	1.174E+00	30.00	1.344E+00	2.3	4.0
37.66	1.187E+00	35.00	1.348E+00	3.3	4.0
42.99	1.204E+00	40.00	1.357E+00	2.8	4.0
48.29	1.190E+00	45.00	1.328E+00	4.6	4.0
53.56	1.114E+00	50.00	1.231E+00	1.6	4.0
58.81	9.629E-01	55.00	1.052E+00	1.9	4.0
64.02	7.885E-01	60.00	8.516E-01	1.2	4.0
69.21	6.436E-01	65.00	6.866E-01	2.7	4.0
74.36	4.712E-01	70.00	4.962E-01	1.6	4.0
79.49	3.729E-01	75.00	3.875E-01	2.9	4.0
84.57	3.016E-01	80.00	3.091E-01	3.4	4.0
89.63	2.433E-01	85.00	2.459E-01	4.1	4.0
94.64	2.201E-01	90.00	2.194E-01	3.6	4.0
99.62	2.083E-01	95.00	2.047E-01	3.7	4.0
104.57	2.039E-01	100.00	1.975E-01	3.0	4.0
109.48	1.957E-01	105.00	1.870E-01	3.3	4.0
114.36	1.803E-01	110.00	1.699E-01	3.1	4.0
119.20	1.839E-01	115.00	1.711E-01	3.0	4.0
124.02	1.742E-01	120.00	1.600E-01	1.7	4.0
128.80	1.791E-01	125.00	1.625E-01	3.2	4.0
133.55	1.749E-01	130.00	1.569E-01	2.5	4.0
138.28	1.841E-01	135.00	1.633E-01	2.5	4.0
142.98	1.837E-01	140.00	1.614E-01	2.8	4.0
147.66	1.935E-01	145.00	1.685E-01	2.4	4.0
152.32	1.970E-01	150.00	1.702E-01	2.4	4.0
156.96	1.939E-01	155.00	1.664E-01	2.5	4.0
162.51	1.909E-01	161.00	1.627E-01	3.7	4.0
166.20	1.837E-01	165.00	1.561E-01	2.9	4.0

TABLE 8. $^{14}N(p,p')^{14}N^*(5.69,(1^-;0))$, E_p = 29.8 MeV.

C.M. ANGLE (DEG.)	DIFFERENTIAL CROSS SECTION (MB/SR)	LAB. ANGLE (DEG.)	DIFFERENTIAL CROSS SECTION (MB/SR)	RELATIVE PER CENT ERROR	NORM. ERROR
21.61	3.898E-01	20.00	4.521E-01	6.8	4.0
26.99	3.774E-01	25.00	4.354E-01	5.6	4.0
32.35	3.985E-01	30.00	4.568E-01	2.8	4.0
37.70	3.710E-01	35.00	4.222E-01	7.6	4.0
43.02	3.598E-01	40.00	4.060E-01	3.3	4.0
48.33	3.497E-01	45.00	3.908E-01	5.1	4.0
53.60	3.414E-01	50.00	3.776E-01	2.8	4.0
58.85	3.278E-01	55.00	3.586E-01	2.6	4.0
64.07	3.110E-01	60.00	3.362E-01	1.7	4.0
69.26	2.910E-01	65.00	3.107E-01	4.5	4.0
74.42	2.544E-01	70.00	2.681E-01	1.7	4.0
79.54	2.318E-01	75.00	2.410E-01	3.1	4.0
84.63	2.098E-01	80.00	2.151E-01	3.6	4.0
89.68	1.916E-01	85.00	1.937E-01	4.3	4.0
94.70	1.742E-01	90.00	1.736E-01	3.7	4.0
99.68	1.405E-01	95.00	1.380E-01	4.0	4.0
104.63	1.251E-01	100.00	1.212E-01	3.3	4.0
109.54	1.135E-01	105.00	1.084E-01	3.5	4.0
114.41	1.025E-01	110.00	9.651E-02	3.7	4.0
119.26	9.723E-02	115.00	9.033E-02	3.3	4.0
124.07	9.595E-02	120.00	8.801E-02	1.9	4.0
128.85	1.024E-01	125.00	9.280E-02	3.5	4.0
133.60	1.079E-01	130.00	9.665E-02	2.5	4.0
138.32	1.241E-01	135.00	1.100E-01	2.6	4.0
143.02	1.290E-01	140.00	1.131E-01	2.9	4.0
147.69	1.409E-01	145.00	1.225E-01	2.5	4.0
156.98	1.480E-01	155.00	1.268E-01	2.7	4.0
162.53	1.394E-01	161.00	1.186E-01	4.0	4.0
166.21	1.553E-01	165.00	1.317E-01	3.1	4.0

TABLE 9. $^{14}N(p,p')^{14}N^*(5.83,(3^-;0))$, E_p = 29.8 MeV.

C.M. ANGLE (DEG.)	DIFFERENTIAL CROSS SECTION (MB/SR)	LAB. ANGLE (DEG.)	DIFFERENTIAL CROSS SECTION (MB/SR)	RELATIVE PER CENT ERROR	NORM. ERROR
21.61	1.168E+00	20.00	1.355E+00	4.2	4.0
26.99	1.289E+00	25.00	1.488E+00	5.0	4.0
32.36	1.510E+00	30.00	1.731E+00	2.1	4.0
37.71	1.498E+00	35.00	1.705E+00	5.5	4.0
43.03	1.588E+00	40.00	1.793E+00	2.9	4.0
48.34	1.617E+00	45.00	1.808E+00	4.6	4.0
53.62	1.542E+00	50.00	1.706E+00	1.7	4.0
58.87	1.374E+00	55.00	1.504E+00	1.7	4.0
64.09	1.159E+00	60.00	1.254E+00	1.1	4.0
69.28	1.003E+00	65.00	1.071E+00	3.1	4.0
74.43	7.632E-01	70.00	8.043E-01	1.5	4.0
79.56	6.234E-01	75.00	6.482E-01	2.9	4.0
84.65	4.809E-01	80.00	4.931E-01	3.3	4.0
89.70	3.825E-01	85.00	3.866E-01	4.0	4.0
94.72	3.220E-01	90.00	3.208E-01	3.6	4.0
99.70	2.899E-01	95.00	2.847E-01	3.8	4.0
104.64	2.633E-01	100.00	2.549E-01	3.0	4.0
109.55	2.450E-01	105.00	2.339E-01	3.3	4.0
114.43	2.043E-01	110.00	1.924E-01	3.2	4.0
119.27	2.171E-01	115.00	2.017E-01	2.8	4.0
124.08	2.102E-01	120.00	1.928E-01	1.7	4.0
128.86	2.236E-01	125.00	2.025E-01	3.1	4.0
133.61	2.200E-01	130.00	1.970E-01	2.3	4.0
138.33	2.387E-01	135.00	2.114E-01	2.4	4.0
143.03	2.442E-01	140.00	2.140E-01	2.7	4.0
147.70	2.461E-01	145.00	2.138E-01	2.3	4.0
156.99	2.213E-01	155.00	1.895E-01	2.5	4.0
162.53	1.978E-01	161.00	1.682E-01	3.8	4.0
166.22	1.747E-01	165.00	1.481E-01	3.0	4.0

TABLE 10. $^{14}N(p,p')^{14}N^*(6.20,(1^+;0))$, E_p = 29.8 MeV.

C.M. ANGLE (DEG.)	DIFFERENTIAL CROSS SECTION (MB/SR)	LAB. ANGLE (DEG.)	DIFFERENTIAL CROSS SECTION (MB/SR)	RELATIVE PER CENT ERROR	NORM. ERROR
21.63	4.808E-02	20.00	5.585E-02	45.7	4.0
27.01	4.180E-02	25.00	4.830E-02	55.3	4.0
32.38	4.398E-02	30.00	5.049E-02	17.1	4.0
37.73	4.174E-02	35.00	4.756E-02	24.5	4.0
43.06	1.991E-02	40.00	2.249E-02	21.7	4.0
48.36	3.790E-02	45.00	4.241E-02	22.4	4.0
53.64	4.084E-02	50.00	4.522E-02	5.9	4.0
58.90	4.243E-02	55.00	4.647E-02	9.5	4.0
64.12	3.450E-02	60.00	3.733E-02	7.1	4.0
69.31	3.078E-02	65.00	3.289E-02	10.5	4.0
74.47	2.843E-02	70.00	2.998E-02	8.5	4.0
79.59	2.700E-02	75.00	2.808E-02	10.1	4.0
84.68	2.430E-02	80.00	2.492E-02	10.1	4.0
89.74	2.127E-02	85.00	2.150E-02	11.9	4.0
94.75	1.943E-02	90.00	1.936E-02	8.2	4.0
99.74	1.767E-02	95.00	1.735E-02	9.4	4.0
104.68	2.059E-02	100.00	1.993E-02	8.7	4.0
109.59	2.200E-02	105.00	2.099E-02	7.0	4.0
114.46	2.408E-02	110.00	2.266E-02	8.3	4.0
119.31	2.447E-02	115.00	2.272E-02	5.9	4.0
124.11	2.672E-02	120.00	2.448E-02	4.4	4.0
128.89	2.658E-02	125.00	2.405E-02	5.0	4.0
133.64	2.676E-02	130.00	2.394E-02	4.4	4.0
138.36	3.112E-02	135.00	2.753E-02	5.7	4.0
143.05	3.026E-02	140.00	2.650E-02	5.9	4.0
147.72	3.899E-02	145.00	3.383E-02	5.1	4.0
152.37	4.598E-02	150.00	3.959E-02	3.4	4.0
157.00	4.850E-02	155.00	4.146E-02	5.2	4.0
162.54	5.652E-02	161.00	4.800E-02	5.0	4.0
166.23	6.674E-02	165.00	5.648E-02	4.1	4.0

TABLE 11. $^{14}N(p,p')^{14}N^*(6.44,(3^+;0))$, E_p = 29.8 MeV.

C.M. ANGLE (DEG.)	DIFFERENTIAL CROSS SECTION (MB/SR)	LAB. ANGLE (DEG.)	DIFFERENTIAL CROSS SECTION (MB/SR)	RELATIVE PER CENT ERROR	NORM. ERROR
32.39	8.971E-02	30.00	1.031E-01	17.3	4.0
37.74	6.726E-02	35.00	7.669E-02	45.2	4.0
43.08	6.649E-02	40.00	7.516E-02	12.5	4.0
48.38	4.755E-02	45.00	5.325E-02	18.0	4.0
53.67	4.180E-02	50.00	4.631E-02	11.2	4.0
58.92	4.069E-02	55.00	4.458E-02	8.6	4.0
64.14	2.976E-02	60.00	3.222E-02	8.6	4.0
69.34	3.645E-02	65.00	3.896E-02	9.3	4.0
74.50	2.852E-02	70.00	3.008E-02	8.0	4.0
79.62	2.971E-02	75.00	3.091E-02	9.7	4.0
84.71	3.304E-02	80.00	3.388E-02	6.3	4.0
89.76	3.531E-02	85.00	3.570E-02	7.0	4.0
94.78	3.275E-02	90.00	3.263E-02	5.4	4.0
99.76	3.330E-02	95.00	3.270E-02	7.1	4.0
104.71	3.239E-02	100.00	3.134E-02	6.6	4.0
109.62	2.880E-02	105.00	2.748E-02	6.0	4.0
114.49	2.751E-02	110.00	2.588E-02	7.6	4.0
119.33	2.757E-02	115.00	2.558E-02	4.1	4.0
124.14	2.519E-02	120.00	2.307E-02	4.2	4.0
128.91	2.607E-02	125.00	2.358E-02	5.8	4.0
133.66	2.683E-02	130.00	2.543E-02	4.5	4.0
138.37	2.921E-02	135.00	2.582E-02	5.3	4.0
143.07	2.752E-02	140.00	2.408E-02	6.6	4.0
147.74	2.828E-02	145.00	2.452E-02	5.5	4.0
152.39	2.645E-02	150.00	2.275E-02	5.2	4.0
157.02	2.982E-02	155.00	2.547E-02	4.7	4.0
162.55	2.886E-02	161.00	2.449E-02	7.1	4.0
166.23	3.491E-02	165.00	2.951E-02	6.6	4.0

TABLE 12. $^{14}N(p,p')^{14}N^*(7.03,(2^+;0))$, E_p = 29.8 MeV.

C.M. ANGLE (DEG.)	DIFFERENTIAL CROSS SECTION (MB/SR)	LAB. ANGLE (DEG.)	DIFFERENTIAL CROSS SECTION (MB/SR)	RELATIVE PER CENT ERROR	NORM. ERROR
21.66	2.203E+00	20.00	2.566E+00	3.4	4.0
27.05	1.698E+00	25.00	1.967E+00	4.4	4.0
32.42	1.392E+00	30.00	1.602E+00	2.5	4.0
37.78	1.113E+00	35.00	1.271E+00	5.5	4.0
43.12	9.180E-01	40.00	1.039E+00	2.9	4.0
48.43	8.263E-01	45.00	9.266E-01	4.5	4.0
53.71	7.152E-01	50.00	7.935E-01	1.9	4.0
58.97	6.694E-01	55.00	7.343E-01	1.9	4.0
64.20	5.417E-01	60.00	5.869E-01	1.9	4.0
69.39	5.364E-01	65.00	5.737E-01	3.0	4.0
74.56	4.517E-01	70.00	4.767E-01	1.8	4.0
79.68	4.189E-01	75.00	4.359E-01	3.2	4.0
84.77	3.475E-01	80.00	3.566E-01	3.5	4.0
89.83	3.128E-01	85.00	3.163E-01	4.1	4.0
94.85	2.737E-01	90.00	2.727E-01	4.0	4.0
99.83	2.313E-01	95.00	2.270E-01	4.2	4.0
104.77	2.184E-01	100.00	2.113E-01	3.5	4.0
109.68	2.082E-01	105.00	1.985E-01	3.6	4.0
114.55	1.924E-01	110.00	1.808E-01	3.8	4.0
119.39	2.003E-01	115.00	1.856E-01	3.1	4.0
124.19	1.964E-01	120.00	1.796E-01	1.9	4.0
128.96	2.063E-01	125.00	1.863E-01	3.3	4.0
133.71	1.997E-01	130.00	1.782E-01	2.5	4.0
138.42	2.194E-01	135.00	1.936E-01	2.8	4.0
143.11	2.251E-01	140.00	1.966E-01	2.8	4.0
147.77	2.499E-01	145.00	2.162E-01	2.4	4.0
152.42	2.711E-01	150.00	2.326E-01	2.5	4.0
157.04	2.937E-01	155.00	2.503E-01	2.5	4.0
162.57	3.236E-01	161.00	2.739E-01	3.8	4.0
166.25	3.295E-01	165.00	2.779E-01	2.8	4.0

TABLE 13. $^{14}N(p,p')^{14}N^*(7.97,(2^-;0))$ E_p = 29.8 MeV.

C.M. ANGLE (DEG.)	DIFFERENTIAL CROSS SECTION (MB/SR)	LAB. ANGLE (DEG.)	DIFFERENTIAL CROSS SECTION (MB/SR)	RELATIVE NORM. PER CENT ERROR	NORM. ERROR
27.10	1.544E-01	25.00	1.794E-01	11.9	4.0
32.48	1.576E-01	30.00	1.820E-01	6.5	4.0
37.84	1.297E-01	35.00	1.486E-01	10.3	4.0
43.19	1.410E-01	40.00	1.601E-01	4.7	4.0
48.51	1.337E-01	45.00	1.503E-01	8.1	4.0
53.80	1.294E-01	50.00	1.439E-01	4.5	4.0
59.06	1.342E-01	55.00	1.475E-01	5.6	4.0
64.29	1.133E-01	60.00	1.230E-01	3.9	4.0
69.49	1.103E-01	65.00	1.182E-01	6.9	4.0
74.66	9.418E-02	70.00	9.951E-02	3.4	4.0
79.79	9.050E-02	75.00	9.427E-02	5.9	4.0
84.88	8.095E-02	80.00	8.309E-02	5.3	4.0
89.94	8.731E-02	85.00	8.829E-02	4.9	4.0
94.96	7.924E-02	90.00	7.893E-02	4.1	4.0
99.94	7.938E-02	95.00	7.788E-02	4.9	4.0
104.88	7.514E-02	100.00	7.262E-02	3.8	4.0
109.78	7.085E-02	105.00	6.746E-02	4.0	4.0
114.65	6.208E-02	110.00	5.826E-02	7.5	4.0
119.49	7.203E-02	115.00	6.664E-02	4.0	4.0
124.29	6.258E-02	120.00	5.711E-02	2.3	4.0
129.05	6.594E-02	125.00	5.940E-02	5.3	4.0
133.79	6.177E-02	130.00	5.497E-02	4.1	4.0
138.50	6.514E-02	135.00	5.731E-02	3.2	4.0
143.18	6.326E-02	140.00	5.508E-02	3.9	4.0
147.84	6.470E-02	145.00	5.580E-02	3.3	4.0
152.47	6.155E-02	150.00	5.264E-02	2.6	4.0
157.09	5.729E-02	155.00	4.864E-02	3.5	4.0
162.61	5.301E-02	161.00	4.469E-02	5.2	4.0
166.28	4.354E-02	165.00	3.658E-02	8.3	4.0

TABLE 14. $^{14}N(p,p')^{14}N^*(8.06,(1^-;1))$, E_p = 29.8 MeV.

C.M. ANGLE (DEG.)	DIFFERENTIAL CROSS SECTION (MB/SR)	LAB. ANGLE (DEG.)	DIFFERENTIAL CROSS SECTION (MB/SR)	RELATIVE PER CENT ERROR	NORM. ERROR
27.10	1.227E-01	25.00	1.427E-01	17.0	4.0
32.48	9.251E-02	30.00	1.068E-01	13.6	4.0
37.85	5.107E-02	35.00	5.852E-02	21.3	4.0
43.19	3.684E-02	40.00	4.183E-02	15.2	4.0
48.51	4.419E-02	45.00	4.968E-02	20.1	4.0
53.81	3.935E-02	50.00	4.377E-02	13.8	4.0
59.07	3.474E-02	55.00	3.818E-02	16.5	4.0
64.30	3.035E-02	60.00	3.295E-02	13.4	4.0
69.50	2.312E-02	65.00	2.476E-02	18.7	4.0
74.67	2.222E-02	70.00	2.348E-02	12.4	4.0
79.80	1.870E-02	75.00	1.947E-02	19.8	4.0
84.89	9.908E-03	80.00	1.017E-02	24.8	4.0
89.95	1.129E-02	85.00	1.142E-02	20.8	4.0
94.96	9.149E-03	90.00	9.113E-03	16.8	4.0
99.94	8.782E-03	95.00	8.617E-03	13.9	4.0
104.89	9.735E-03	100.00	9.408E-03	17.3	4.0
109.79	1.324E-02	105.00	1.260E-02	14.0	4.0
114.66	1.526E-02	110.00	1.432E-02	25.3	4.0
119.49	1.122E-02	115.00	1.038E-02	14.1	4.0
124.29	1.234E-02	120.00	1.126E-02	11.5	4.0
129.06	1.104E-02	125.00	9.944E-03	16.2	4.0
133.80	9.329E-03	130.00	8.300E-03	13.3	4.0
138.50	7.255E-03	135.00	6.382E-03	13.7	4.0
143.18	6.434E-03	140.00	5.600E-03	14.1	4.0
147.84	6.777E-03	145.00	5.842E-03	13.3	4.0
152.48	6.962E-03	150.00	5.952E-03	12.1	4.0
157.09	1.024E-02	155.00	8.691E-03	12.3	4.0
162.61	1.437E-02	161.00	1.211E-02	13.5	4.0
166.28	1.634E-02	165.00	1.372E-02	15.9	4.0

TABLE 15. $^{14}N(p,p')^{14}N^*(8.49,(4^-;0))$, E_p = 29.8 MeV.

C.M. ANGLE (DEG.)	DIFFERENTIAL CROSS SECTION (MB/SR)	LAB. ANGLE (DEG.)	DIFFERENTIAL CROSS SECTION (MB/SR)	RELATIVE PER CENT ERROR	NORM. ERROR
21.72	2.942E-01	20.00	3.445E-01	10.6	4.0
27.12	3.044E-01	25.00	3.545E-01	6.6	4.0
32.51	3.452E-01	30.00	3.993E-01	3.0	4.0
37.88	3.286E-01	35.00	3.770E-01	6.8	4.0
43.23	3.281E-01	40.00	3.731E-01	3.5	4.0
48.55	3.290E-01	45.00	3.703E-01	6.9	4.0
53.85	3.280E-01	50.00	3.652E-01	2.1	4.0
59.12	3.057E-01	55.00	3.364E-01	2.9	4.0
64.35	2.614E-01	60.00	2.840E-01	2.3	4.0
69.55	2.357E-01	65.00	2.527E-01	5.2	4.0
79.85	1.654E-01	70.00	2.069E-01	4.2	4.0
74.72	1.957E-01	75.00	1.723E-01	2.4	4.0
84.95	1.258E-01	80.00	1.292E-01	5.4	4.0
90.00	1.059E-01	85.00	1.072E-01	5.3	4.0
95.02	9.518E-02	90.00	9.480E-02	4.3	4.0
100.00	9.210E-02	95.00	9.033E-02	5.0	4.0
104.94	9.412E-02	100.00	9.091E-02	3.6	4.0
109.85	1.068E-01	105.00	1.016E-01	3.9	4.0
114.71	1.075E-01	110.00	1.008E-01	4.0	4.0
119.55	1.162E-01	115.00	1.074E-01	3.6	4.0
129.11	1.207E-01	120.00	1.055E-01	3.5	4.0
124.34	1.157E-01	125.00	1.086E-01	2.4	4.0
133.84	1.271E-01	130.00	1.129E-01	3.2	4.0
138.54	1.309E-01	135.00	1.149E-01	2.6	4.0
143.22	1.280E-01	140.00	1.113E-01	3.3	4.0
147.87	1.321E-01	145.00	1.137E-01	2.5	4.0
152.50	1.381E-01	150.00	1.178E-01	2.9	4.0
157.12	1.439E-01	155.00	1.219E-01	3.0	4.0
162.63	1.474E-01	161.00	1.240E-01	4.2	4.0
166.30	1.432E-01	165.00	1.200E-01	3.4	4.0

TABLE 16. $^{14}N(p,p)\ ^{14}N$ elastic scattering for E_p = 36.6 MeV.

C.M. ANGLE (DEG.)	DIFFERENTIAL CROSS SECTION (MB/SR)	LAB. ANGLE (DEG.)	DIFFERENTIAL CROSS SECTION (MB/SR)	RELATIVE NORM. PER CENT ERROR	
16.10	9.758E+02	15.00	1.120E+03	.8	4.0
18.78	8.380E+02	17.50	9.601E+02	1.0	4.0
21.45	6.809E+02	20.00	7.787E+02	.4	4.0
26.79	4.049E+02	25.00	4.609E+02	1.0	4.0
32.12	2.051E+02	30.00	2.320E+02	1.0	4.0
37.43	9.556E+01	35.00	1.074E+02	1.8	4.0
42.73	3.880E+01	40.00	4.328E+01	2.0	4.0
48.00	2.110E+01	45.00	2.333E+01	1.6	4.0
53.25	1.720E+01	50.00	1.885E+01	1.9	4.0
58.47	1.717E+01	55.00	1.862E+01	1.2	4.0
63.67	1.593E+01	60.00	1.710E+01	1.4	4.0
68.84	1.300E+01	65.00	1.379E+01	1.0	4.0
73.98	9.255E+00	70.00	9.705E+00	1.5	4.0
79.09	6.159E+00	75.00	6.380E+00	1.9	4.0
84.17	3.787E+00	80.00	3.874E+00	1.4	4.0
89.22	2.375E+00	85.00	2.399E+00	1.3	4.0
94.24	1.627E+00	90.00	1.623E+00	1.4	4.0
99.22	1.274E+00	95.00	1.254E+00	3.0	4.0
104.17	1.066E+00	100.00	1.035E+00	4.0	4.0
109.09	8.833E-01	105.00	8.475E-01	3.4	4.0
113.98	7.478E-01	110.00	7.086E-01	4.0	4.0
118.83	6.106E-01	115.00	5.717E-01	3.3	4.0
123.66	4.748E-01	120.00	4.394E-01	3.0	4.0
128.46	4.208E-01	125.00	3.852E-01	3.4	4.0
137.99	4.850E-01	135.00	4.351E-01	4.0	4.0

TABLE 17. $^{14}N(p,p')^{14}N^*(2.31,(0^+;1))$, E_p = 36.6 MeV.

C.M. ANGLE (DEG.)	DIFFERENTIAL CROSS SECTION (MB/SR)	LAB. ANGLE (DEG.)	DIFFERENTIAL CROSS SECTION (MB/SR)	RELATIVE PER CENT ERROR	NORM. ERROR
10.74	1.119E-01	10.00	1.289E-01	2.8	4.0
12.88	1.228E-01	12.00	1.412E-01	7.0	4.0
18.24	1.036E-01	17.00	1.188E-01	8.0	4.0
21.45	8.789E-02	20.00	1.005E-01	2.1	4.0
26.79	7.625E-02	25.00	8.678E-02	3.3	4.0
32.12	5.576E-02	30.00	6.310E-02	1.8	4.0
37.43	3.012E-02	35.00	3.385E-02	4.7	4.0
42.73	1.843E-02	40.00	2.055E-02	2.1	4.0
48.00	8.901E-03	45.00	9.844E-03	2.9	4.0
53.25	7.068E-03	50.00	7.744E-03	2.8	4.0
58.47	9.112E-03	55.00	9.884E-03	4.2	4.0
63.67	1.280E-02	60.00	1.374E-02	2.8	4.0
68.84	1.799E-02	65.00	1.909E-02	4.4	4.0
73.98	1.880E-02	70.00	1.971E-02	5.8	4.0
79.09	2.073E-02	75.00	2.147E-02	2.6	4.0
84.17	1.817E-02	80.00	1.859E-02	6.7	4.0
89.22	1.692E-02	85.00	1.709E-02	6.5	4.0
94.24	1.354E-02	90.00	1.350E-02	2.6	4.0
99.22	1.070E-02	95.00	1.053E-02	6.4	4.0
104.17	7.846E-03	100.00	7.624E-03	7.4	4.0
109.09	7.226E-03	105.00	6.934E-03	2.9	4.0
113.98	6.076E-03	110.00	5.758E-03	7.0	4.0
118.83	6.262E-03	115.00	5.863E-03	8.2	4.0
123.66	6.059E-03	120.00	5.607E-03	3.6	4.0
128.46	4.834E-03	125.00	4.424E-03	9.6	4.0
137.99	3.292E-03	135.00	2.953E-03	17.2	4.0

TABLE 18. $^{14}N(p,p')^{14}N^*(3.94,(1^+;0))$, E_p = 36.6 MeV.

C.M. ANGLE (DEG.)	DIFFERENTIAL CROSS SECTION (MB/SR)	LAB. ANGLE (DEG.)	DIFFERENTIAL CROSS SECTION (MB/SR)	RELATIVE PER CENT ERROR	NORM. ERROR
10.74	1.585E+00	10.00	1.824E+00	3.2	4.0
12.88	1.509E+00	12.00	1.735E+00	3.5	4.0
18.24	1.329E+00	17.00	1.523E+00	2.2	4.0
26.79	1.119E+00	25.00	1.274E+00	4.8	4.0
32.12	9.640E-01	30.00	1.091E+00	4.4	4.0
37.43	8.692E-01	35.00	9.770E-01	1.9	4.0
42.73	7.568E-01	40.00	8.441E-01	4.0	4.0
48.00	6.213E-01	45.00	6.870E-01	4.4	4.0
58.47	3.476E-01	55.00	3.771E-01	6.0	4.0
63.67	2.691E-01	60.00	2.888E-01	4.6	4.0
68.84	2.215E-01	65.00	2.350E-01	4.2	4.0
73.98	1.902E-01	70.00	1.995E-01	4.3	4.0
79.09	1.635E-01	75.00	1.694E-01	4.9	4.0
84.17	1.373E-01	80.00	1.405E-01	4.6	4.0
89.22	1.032E-01	85.00	1.043E-01	3.8	4.0
94.24	7.937E-02	90.00	7.914E-02	4.0	4.0
99.22	5.823E-02	95.00	5.731E-02	7.1	4.0
104.17	4.302E-02	100.00	4.180E-02	5.4	4.0
109.09	3.194E-02	105.00	3.065E-02	6.0	4.0
113.98	3.450E-02	110.00	3.270E-02	6.2	4.0
118.83	2.999E-02	115.00	2.807E-02	5.6	4.0
123.66	3.104E-02	120.00	2.873E-02	6.4	4.0
128.46	3.893E-02	125.00	3.563E-02	7.7	4.0
137.99	5.821E-02	135.00	5.222E-02	5.0	4.0
142.72	6.309E-02	140.00	5.609E-02	5.8	4.0

TABLE 19. $^{14}N(p,p)^{14}N$ elastic scattering for E_p = 40.0 MeV.

C.M. ANGLE (DEG.)	DIFFERENTIAL CROSS SECTION (MB/SR)	LAB. ANGLE (DEG.)	DIFFERENTIAL CROSS SECTION (MB/SR)	RELATIVE PER CENT ERROR	NORM. ERROR
16.10	9.482E+02	15.00	1.089E+03	.1	4.0
18.08	8.675E+01	17.50	9.260E+02	1.2	4.0
21.46	6.422E+02	20.00	7.348E+02	.2	4.0
26.80	3.516E+02	25.00	4.003E+02	.9	4.0
32.13	1.817E+02	30.00	2.047E+02	.5	4.0
37.44	7.584E+01	35.00	8.527E+01	1.4	4.0
40.09	4.762E+01	37.50	5.334E+01	.8	4.0
42.74	3.230E+01	40.00	3.604E+01	2.9	4.0
45.37	2.155E+01	42.50	2.395E+01	1.4	4.0
48.01	1.854E+01	45.00	2.051E+01	1.6	4.0
53.26	1.638E+01	50.00	1.795E+01	2.2	4.0
58.48	1.543E+01	55.00	1.674E+01	1.3	4.0
63.68	1.320E+01	60.00	1.417E+01	2.1	4.0
68.85	1.014E+01	65.00	1.076E+01	1.1	4.0
74.00	6.939E+00	70.00	7.277E+00	1.2	4.0
79.11	4.364E+00	75.00	4.521E+00	1.3	4.0
84.19	2.567E+00	80.00	2.626E+00	1.5	4.0
89.23	1.725E+00	85.00	1.742E+00	1.1	4.0
94.25	1.301E+00	90.00	1.297E+00	1.5	4.0
99.23	1.098E+00	95.00	1.080E+00	1.4	4.0
104.18	9.498E-01	100.00	9.229E-01	1.8	4.0
113.99	6.406E-01	110.00	6.069E-01	1.2	4.0
123.67	3.302E-01	120.00	3.055E-01	2.0	4.0

TABLE 20. $^{14}N(p,p')^{14}N^*(2.31,(0^+;1))$, E_p = 40.0 MeV.

C.M. ANGLE (DEG.)	DIFFERENTIAL CROSS SECTION (MB/SR)	LAB. ANGLE (DEG.)	DIFFERENTIAL CROSS SECTION (MB/SR)	RELATIVE PER CENT ERROR	NORM. ERROR
10.74	1.198E-01	10.00	1.379E-01	2.8	4.0
18.24	1.041E-01	17.00	1.194E-01	2.7	4.0
21.46	1.007E-01	20.00	1.153E-01	2.7	4.0
26.80	7.600E-02	25.00	8.654E-02	2.4	4.0
32.13	5.433E-02	30.00	6.150E-02	1.8	4.0
37.44	3.251E-02	35.00	3.655E-02	2.7	4.0
42.74	1.641E-02	40.00	1.831E-02	3.0	4.0
48.01	8.040E-03	45.00	8.894E-03	3.8	4.0
53.26	7.651E-03	50.00	8.385E-03	3.2	4.0
58.48	1.115E-02	55.00	1.210E-02	3.6	4.0
63.68	1.675E-02	60.00	1.797E-02	2.9	4.0
68.85	2.163E-02	65.00	2.295E-02	3.1	4.0
74.00	2.396E-02	70.00	2.513E-02	2.0	4.0
79.11	2.344E-02	75.00	2.429E-02	3.0	4.0
84.19	2.281E-02	80.00	2.334E-02	2.8	4.0
89.23	1.786E-02	85.00	1.804E-02	3.3	4.0
94.25	1.485E-02	90.00	1.481E-02	3.0	4.0
99.23	1.017E-02	95.00	1.001E-02	3.7	4.0
104.18	7.531E-03	100.00	7.317E-03	4.0	4.0
113.99	4.664E-03	110.00	4.419E-03	4.2	4.0
123.67	4.305E-03	120.00	3.983E-03	5.1	4.0

TABLE 21. $^{14}N(p,p')^{14}N^*(3.94,(1^+;0))$, E_p = 40.0 MeV.

C.M. ANGLE (DEG.)	DIFFERENTIAL CROSS SECTION (MB/SR)	LAB. ANGLE (DEG.)	DIFFERENTIAL CROSS SECTION (MB/SR)	RELATIVE PER CENT ERROR	NORM. ERROR
10.74	1.541E+00	10.00	1.775E+00	2.1	4.0
21.46	1.161E+00	20.00	1.328E+00	2.6	4.0
32.13	1.020E+00	30.00	1.154E+00	1.2	4.0
42.74	7.715E-01	40.00	8.608E-01	2.4	4.0
53.26	4.351E-01	50.00	4.768E-01	2.2	4.0
63.68	2.566E-01	60.00	2.754E-01	2.2	4.0
74.00	1.746E-01	70.00	1.831E-01	2.1	4.0
84.19	1.118E-01	80.00	1.144E-01	2.4	4.0
94.25	5.810E-02	90.00	5.793E-02	2.9	4.0
99.23	4.462E-02	95.00	4.392E-02	2.9	4.0
104.18	3.585E-02	100.00	3.483E-02	3.4	4.0
113.99	2.437E-02	110.00	2.309E-02	3.4	4.0
123.67	2.543E-02	120.00	2.353E-02	3.0	4.0

TABLE 22. $^{14}N(p,p')^{14}N^*$(2.31 MeV) plotted against momentum transfer for E_p = 24.8 MeV (Cr 70).

MOMENTUM TRANSFER (1/F)	DIFFERENTIAL CROSS SECTION (MB/SR)	RELATIVE PER CENT ERROR
.374	3.60000E-01	41.7
.392	2.15000E-01	16.3
.488	1.45000E-01	13.8
.581	1.18000E-01	16.9
.656	9.00000E-02	11.1
.747	7.79999E-02	15.4
.853	4.80000E-02	8.3
.924	4.40000E-02	13.6
1.024	2.85000E-02	10.5
1.107	2.25000E-02	13.3
1.262	2.10000E-02	14.3
1.392	2.48000E-02	11.3
1.524	2.73000E-02	11.7
1.654	2.28000E-02	12.3
1.759	2.70000E-02	9.3
1.847	3.12000E-02	6.4
1.923	2.88000E-02	7.6
1.985	2.20000E-02	8.2
2.033	2.07000E-02	8.2
2.067	2.34000E-02	5.6

TABLE 23. $^{14}N(p,p')^{14}N^*$(2.31 MeV) plotted against momentum transfer for E_p = 29.8 MeV.

MOMENTUM TRANSFER (1/F)	DIFFERENTIAL CROSS SECTION (MB/SR)	RELATIVE PER CENT ERROR
•218	2•03580E-01	2•2
•427	1•37180E-01	1•7
•530	1•07450E-01	1•7
•633	8•15720E-02	1•1
•832	3•79270E-02	2•2
•929	2•49240E-02	3•1
1•023	1•92270E-02	2•2
1•115	1•63630E-02	3•1
1•204	1•54870E-02	2•6
1•290	1•61560E-02	3•4
1•373	1•95000E-02	2•3
1•605	2•27930E-02	8•2
1•803	2•28270E-02	6•6
1•859	1•91640E-02	2•5
2•013	1•60960E-02	3•7
2•096	9•76580E-03	5•2
2•163	5•90570E-03	11•5
2•215	9•51850E-03	7•1
2•236	1•61690E-02	5•7
2•255	2•78930E-02	7•7
2•266	3•06570E-02	4•7

TABLE 24. $^{14}N(p,p')^{14}N^*$ (2.31 MeV) plotted against momentum transfer for E_p = 36.6 MeV.

MOMENTUM TRANSFER (1/F)	DIFFERENTIAL CROSS SECTION (MB/SR)	RELATIVE PER CENT ERROR
.239	1.11940E-01	2.7
.471	8.78870E-02	2.0
.698	5.57620E-02	1.8
.810	3.01200E-02	4.6
.919	1.84250E-02	2.1
1.026	8.90130E-03	2.9
1.130	7.06800E-03	2.8
1.231	9.11210E-03	4.1
1.330	1.28030E-02	2.7
1.425	1.79890E-02	4.3
1.517	1.87950E-02	5.6
1.605	2.07290E-02	2.6
1.689	1.81740E-02	6.6
1.770	1.69240E-02	6.3
1.847	1.35350E-02	2.6
1.920	1.07020E-02	6.3
1.988	7.84620E-03	7.2
2.113	6.07580E-03	6.8
2.222	6.05870E-03	3.5
2.269	4.83370E-03	9.3
2.353	3.29190E-03	16.8

TABLE 25. $^{14}N(p,p')^{14}N^*$(2.31 MeV) plotted against momentum transfer for E_p = 40.0 MeV.

MOMENTUM TRANSFER (1/F)	DIFFERENTIAL CROSS SECTION (MB/SR)	RELATIVE PER CENT ERROR
•249	1•19760E-01	2•7
•419	1•04130E-01	2•6
•611	7•60030E-02	2•4
•845	3•25080E-02	2•6
•959	1•64120E-02	2•9
1•071	8•03970E-03	3•7
1•180	7•65070E-03	3•1
1•286	1•11490E-02	3•5
1•388	1•67460E-02	2•8
1•488	2•16300E-02	3•0
1•584	2•39610E-02	2•0
1•764	2•28100E-02	2•8
1•848	1•78580E-02	3•2
1•928	1•48540E-02	2•9
2•004	1•01710E-02	3•6
2•076	7•53090E-03	3•9
2•206	4•56400E-03	4•1
2•319	4•30470E-03	4•9

4. OPTICAL MODEL ANALYSIS

4.1 Purpose

An optical model analysis was made of the differential cross sections for elastically scattered protons by ^{14}N at incident beam energies of 24.8 (Cr 70a), 29.8, 36.6 and 40.0 MeV. One purpose was to obtain optical model parameters for DWBA analysis of the measured proton inelastic scattering data. For light nuclei this is not as straight forward an operation as it is for heavy nuclei. While it was possible to fit any one of the elastic scattering angular distributions, unrestrained mosel parameters would fluctuate widely from case to case. This sort of behavior is not unexpected since two assumptions of the optical model may not be valid for light nuclei. First the density of compound-nucleus levels is low and so nuclear structure effects not described by the model may not average out. More important for the incident proton energies involved here, is that it may not be appropriate to replace the nucleus with a potential having a simple radial form.

DWBA calculations of proton-^{14}N inelastic scattering require optical model parameters that describe proton-^{14}N elastic scattering for exit particles which have different energies than those for which angular

distributions were measured. These parameters must be obtained by interpolating between the incident energies where data is available. If the variation with energy of the optical model parameters obtained is not smooth, the intermediate parameters are uncertain. To avoid singular sets of parameters, an average set of geometrical parameters, radii and diffuseness parameters was sought that would fit all the data equally well. The potential strengths were varied to fit the data at each energy with the hope that well strength parameters would vary smoothly from energy to energy.

4.2 Elastic Scattering Data

The ^{14}N (p,p) data for incident proton energies of 29.8, 36.6 and 40.0 MeV were presented earlier (see Tables 3, 16, 19, and Figures 14, 27, 30). Data at 24.9 MeV taken by Crawley *et al.* is found in Table(22). The errors include uncertainty in overall normalization. The overall normalization was not varied as a part of the fitting procedure, although it was varied after the fitting schedule. There was negligible improvement in χ^2/N for $\pm$ 1% changes in absolute normalization.

Since the optical model was not expected to fit the angular distributions well past the second minima in the ratio to Rutherford cross sections, the errors on the points beyond that angle were about doubled during the searches.

The actual errors used in the searches are found in Tables (26) and (27) with the data. Thus these points were weighted relatively less in the search procedure. The χ^2/N values presented are for the actual experimental errors.

4.3 Optical Model Searches

The main part of the optical model analysis was done with the optical model search code GIBELUMP[+] running in the M.S.U. Cyclotron Σ-7 computer. The interaction of the two nuclei involved was represented by scattering from the one-body complex potential below:

$$V_{opt}(r) = V_C(r) - V_R f(x_R) - i\left(W_S - 4W_D \frac{d}{dx_I}\right) f(x_I) + V_{SO} \frac{\hbar^2}{(M_\pi c)^2} \frac{1}{r}\frac{d}{dr} f(x_{SO})\,(\vec{l}\cdot\vec{\sigma})$$

where:

$$V_C(r) = \frac{ZZ'e^2}{r}, r \geq R_C; = \frac{ZZ'e^2}{2R_C}\left(3 - \frac{r^2}{R_C^2}\right), r < R_C$$

$$R_C = r_C A^{1/3}$$

$$f(x) = (1 + e^x)^{-1}$$

$$x_R = \frac{r - r_R A^{1/3}}{a_R}$$

$$x_I = \frac{r - r_I A^{1/3}}{a_I}$$

$$x_{SO} = \frac{r - r_{SO} A^{1/3}}{a_{SO}}$$

[+]An optical model search code written by F. G. Perey and modified by R. M. Haybron at Oak Ridge National Laboratory.

TABLE 26. $^{14}N(p,p)^{14}N$ elastic scattering for E_p = 24.8 and 29.8 MeV with the errors used during optical model searches.

24.8 MeV			29.8 MeV		
C.M. ANGLE (DEG.)	DIFFERENTIAL CROSS SECTION (MB/SR)	ERROR (%)	C.M. ANGLE (DEG.)	DIFFERENTIAL CROSS SECTION (MB/SR)	ERROR (%)
10.66	1.608E+03	3.0	10.73	1.502E+03	4.1
16.01	9.607E+02	2.7	16.09	1.045E+03	4.1
21.35	6.950E+02	2.4	21.44	7.473E+02	4.1
26.69	4.704E+02	2.4	26.78	4.795E+02	4.1
32.01	2.778E+02	2.2	32.11	2.765E+02	4.1
37.32	1.470E+02	2.3	37.42	1.348E+02	4.1
42.61	7.268E+01	2.5	42.71	5.948E+01	4.2
47.88	3.600E+01	2.3	47.98	2.866E+01	4.2
53.13	2.350E+01	3.1	53.23	2.094E+01	4.2
58.36	2.271E+01	2.5	58.45	2.108E+01	4.2
63.56	2.522E+01	3.1	63.65	2.208E+01	4.2
68.74	2.697E+01	3.1	68.82	2.136E+01	4.3
73.89	2.510E+01	3.2	73.96	1.780E+01	4.2
79.01	2.089E+01	2.3	79.07	1.377E+01	4.3
84.09	1.746E+01	2.8	84.15	9.501E+00	4.2
89.15	1.287E+01	2.4	89.19	6.138E+00	4.5
94.17	8.780E+00	3.2	94.21	3.943E+00	4.3
99.17	5.350E+00	2.7	99.19	2.592E+00	4.5
104.12	3.395E+00	4.0	104.14	1.870E+00	4.3
109.05	2.239E+00	2.8	109.06	1.458E+00	15.0
113.95	1.545E+00	5.0	113.95	1.161E+00	15.0
118.81	1.470E+00	3.4	118.81	1.055E+00	15.0
123.64	1.785E+00	6.0	123.64	1.058E+00	15.0
128.45	2.083E+00	6.0	128.44	1.178E+00	15.0
133.22	2.455E+00	6.0	133.22	1.381E+00	15.0
137.98	3.035E+00	6.0	137.97	1.679E+00	15.0
142.70	3.288E+00	6.0	142.70	1.837E+00	15.0
147.41	3.130E+00	6.0	147.41	1.995E+00	15.0
152.09	2.999E+00	6.0	152.10	2.012E+00	15.0
156.79	2.590E+00	6.0	156.79	1.921E+00	15.0
161.42	2.322E+00	6.0	161.44	1.714E+00	15.0
			166.09	1.428E+00	15.0

TABLE 27. $^{14}N(p,p)^{14}N$ elastic scattering for E_p = 36.6 and 40.0 MeV with the errors used during optical model searches.

36.6 MeV			40.0 MeV		
C.M. ANGLE (DEG.)	DIFFERENTIAL CROSS SECTION (MB/SR)	ERROR (%)	C.M. ANGLE (DEG.)	DIFFERENTIAL CROSS SECTION (MB/SR)	ERROR (%)
16.10	9.758E+02	5.0	16.10	9.482E+02	3.0
18.78	8.380E+02	3.0	18.78	8.077E+02	3.0
21.45	6.809E+02	2.9	21.46	6.423E+02	3.0
26.79	4.050E+02	3.0	26.80	3.516E+02	2.2
32.12	2.051E+02	3.0	32.13	1.817E+02	2.8
37.43	9.556E+01	1.8	37.44	7.584E+01	1.7
42.73	3.880E+01	2.0	40.09	4.762E+01	1.7
48.00	2.110E+01	5.0	42.74	3.230E+01	1.5
53.25	1.721E+01	1.8	45.37	2.155E+01	2.0
58.47	1.717E+01	1.1	48.01	1.840E+01	1.7
63.67	1.593E+01	1.4	53.26	1.638E+01	2.7
68.84	1.299E+01	1.0	58.48	1.543E+01	2.0
73.98	9.255E+00	1.5	63.68	1.320E+01	2.6
79.09	6.159E+00	1.9	68.85	1.014E+01	1.8
84.17	3.787E+00	1.4	74.00	6.939E+00	1.4
89.22	2.375E+00	1.3	79.11	4.364E+00	2.0
94.24	1.627E+00	1.4	84.19	2.567E+00	2.1
99.22	1.274E+00	3.0	89.23	1.725E+00	1.8
104.17	1.065E+00	4.0	94.25	1.301E+00	2.1
109.09	8.833E-01	5.0	99.23	1.098E+00	5.0
113.98	7.478E-01	5.0	104.18	9.498E-01	5.0
118.83	6.106E-01	5.0	113.99	6.406E-01	5.0
123.66	4.748E-01	5.0	123.67	3.302E-01	5.0
128.46	4.208E-01	5.0			
137.99	4.850E-01	5.0			

V_C is the potential felt by a point charge Ze in the electrostatic static field of a uniformly charge sphere of radius (R_C) and charge ($Z'e$). $f(r, r_o a_o)$ is the usual Woods-Saxon form factor with radius parameter r_o and diffuseness a_o. The potentials and geometrical parameters were varied singly or in combinations and the code sought to minimize the quantity

$$\chi^2/N = 1/N \sum_i [(\sigma_{Th}(i) - \sigma_{EXP}(i))/\Delta\sigma_{EXP}(i)]^2$$

where N is the number of experimental data points, $\sigma_{Th}(i)$ and $\sigma_{EXP}(i)$ are the theoretical and experimental cross sections at angle θ_i in the center-of-mass frame and $\Delta\sigma_{EXP}(i)$ is the experimental error in $\sigma_{EXP}(i)$.

The searches began with six different sets of optical model parameters for the A = 14 mass region taken from the literature (Ca 69, Sa 70, Wa 69, Pe 63, Ki 64, Sn 69). The object was to reach different relative minima in χ^2/N space and then to choose trial average geometries from the results.

For the 24.9 and 29.8 MeV data, the spin-orbit radii tended to unrealistically large values and the diffusenesses to smaller than expected values. The effect of this was to improve the fits somewhat at angles beyond the second minima. Because the optical model does not generally fit backward angle scattering data well in the mass region of ^{14}N and because polarization data are needed to convincingly

determine the spin-orbit well, the spin-orbit geometrical parameters were set equal to those of the real potential in the geometry finally choosen.

The searches were generally two parameter searches. The pairs of parameters were usually V_R V_I, a_R a_I, r_R W_S, V_R V_{SO}, or r_I r_R.. Often the search schedule ended with a search on all the variable parameters just to see how good the model could possibly fit the data. Through trial and error an average set of geometrical parameters was obtained and the well strengths were then varied to best fit the data. The final set of parameters are found in Table (28), and the fits to the elastic scattering data, in Figures (34) and (35).

To get an idea of how sensitive the fits were to changes in the final parameters, optical model calculations for the four sets of data were made with each parameter varied + and - 5%. The resultant percent change in χ^2/N is also in Table (28). The results indicate that the fits are most sensitive to the real potential depth and geometry.

4.4 Spin-Orbit Form Factor

It is not completely clear just what form the radial part of the spin-orbit potential should have. The argument for a form factor that peaks at the nuclear surface is made on two counts. The potential is strongest for incident nuclei with large l values and these spend most of

TABLE 28. ^{14}N optical model parameters found in this work

E_p LAB (MeV)	24.8		29.8		36.6		40.0	
V_R (MeV)	51.36	(155)*	49.09	(116)	45.67	(744)	43.79	(702)
r_R (F)	1.133	(386)	1.133	(277)	1.133	(1724)	1.133	(1689)
a_R (F)	0.651	(20)	0.651	(18)	0.651	(96)	0.651	(75)
W_S (MeV)	1.56	(0)**	2.93	(2)	5.76	(42)	5.75	(61)
W_D (MeV)	4.75	(18)	3.52	(9)	1.63	(12)	1.93	(22)
r_I (F)	1.345	(72)	1.345	(74)	1.345	(632)	1.345	(886)
a_I (F)	0.509	(18)	0.509	(11)	0.509	(28)	0.509	(54)
V_{SO} (MeV)	4.24	(0)	5.31	(0)	5.60	(5)	8.61	(31)
r_{SO} (F)	r_R	(0)	r_R	(0)	r_R	(8)	r_R	(49)
a_{SO} (F)	a_R	(0)	a_R	(0)	a_R	(9)	a_R	(46)
r_C (F)	1.25		1.25		1.25		1.25	
χ^2/N	31.0		45.0		6.9		3.9	

* % change in χ^2/N for a 5% parameter change.

** To the nearest %.

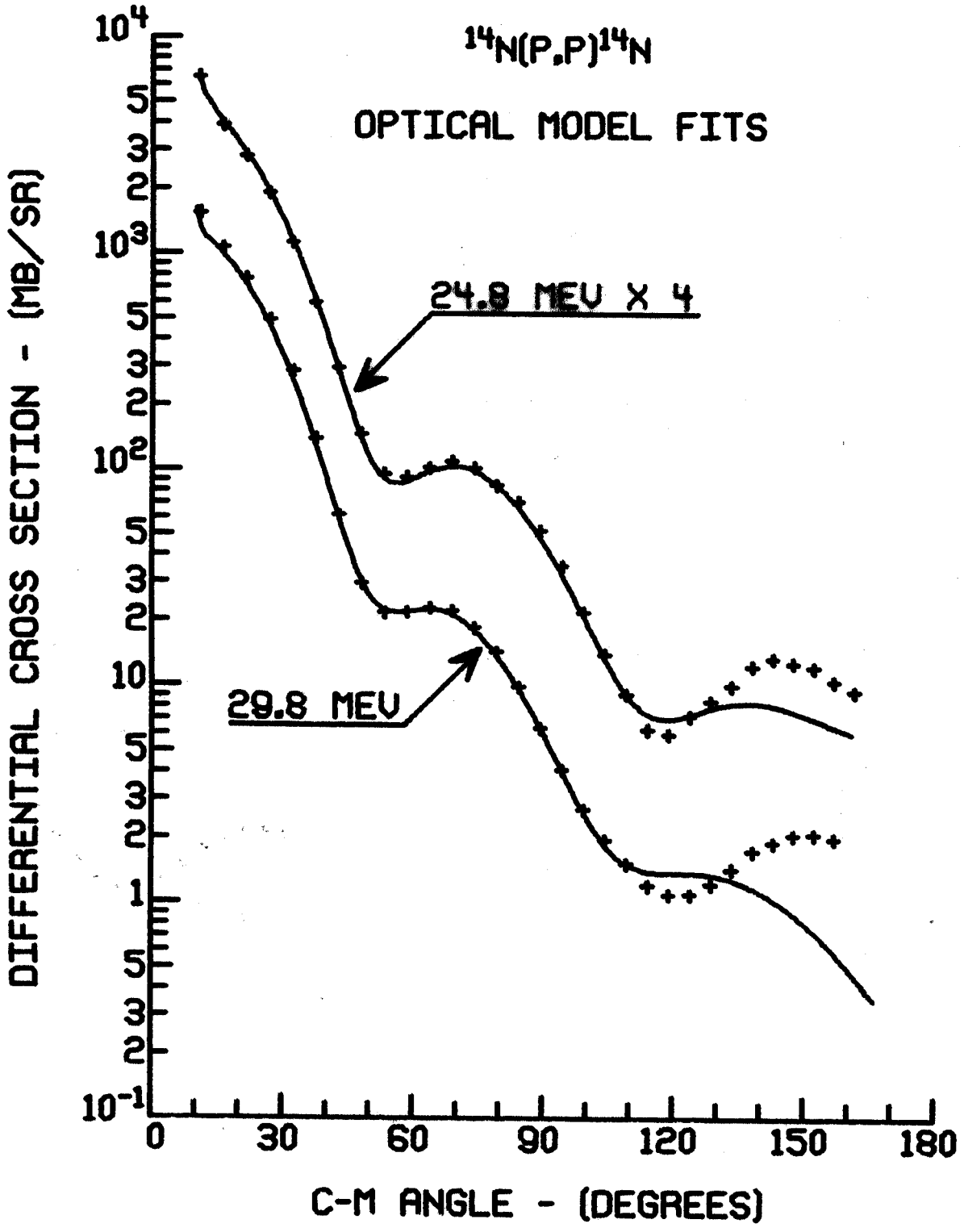

FIGURE 34. Optical model fits to the 24.8 MeV and 29.8 MeV ^{14}N elastic scattering for the optical model potential determined by this work with $r_{SO} = r_R$ and $a_{SO} = a_R$.

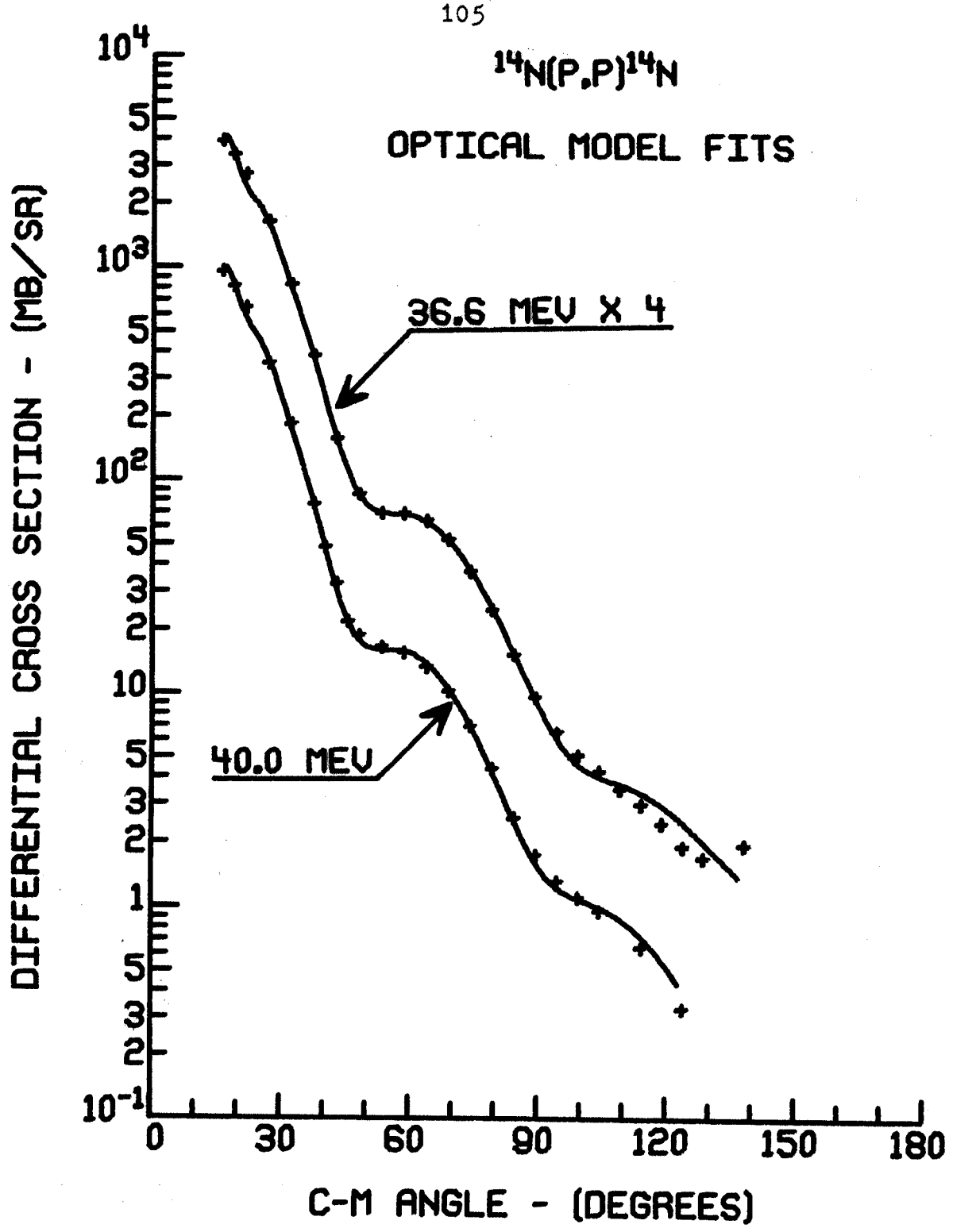

FIGURE 35. Optical model fits to the 36.6 and 40.0 MeV ^{14}N elastic scattering for the optical model of this work with $r_{SO} = r_R$ and $a_{SO} = a_R$.

their time in the vacinity of the nucleus at its surface. It is also argued that only at the surface does the nuclear matter density have a non zero gradient and only there can the incident nuclei retain some sense of its direction. The Thomas form for the potential which is used in GIBELUMP was originally added to the optical potential for heavy nuclei. For these nuclei, the radius parameter is large enough and consequently the derivative of the Woods-Saxon form is small enough near (but not at) the origin to dominate the 1/r term for all practical purposes. This is not true when the Thomas form is used for light nuclei. Here the 1/r term dominates and the potential becomes very large well out from the origin. See Figure(36. Watson, Singh and Segel, in their optical model analysis of nucleon elastic scattering from 1p-shell nuclei, used the modified spin-orbit potential below:

$$V_{SO}(r) \approx \bar{\sigma}\cdot\bar{\ell}\; V_{SO}\; \frac{\hbar^2}{(M_\pi c)^2}\; \frac{1}{(r_{SO}A^{-1/3})}\; \frac{d}{dr}\, f_{SO}(r)$$

where f (r) is the usual Woods-Saxon shape. This modified form for the geometrical parameters also is shown in Figure (36. Bob Doering at the M.S.U. Cyclotron Lab made available a version of GIBELUMP with this modified spin-orbit potential, GIBPRIME.

Using GIBPRIME it was possible to fit the four ^{14}N proton elastic scattering angular distributions with the optical model potential and parameters suggested by Watson

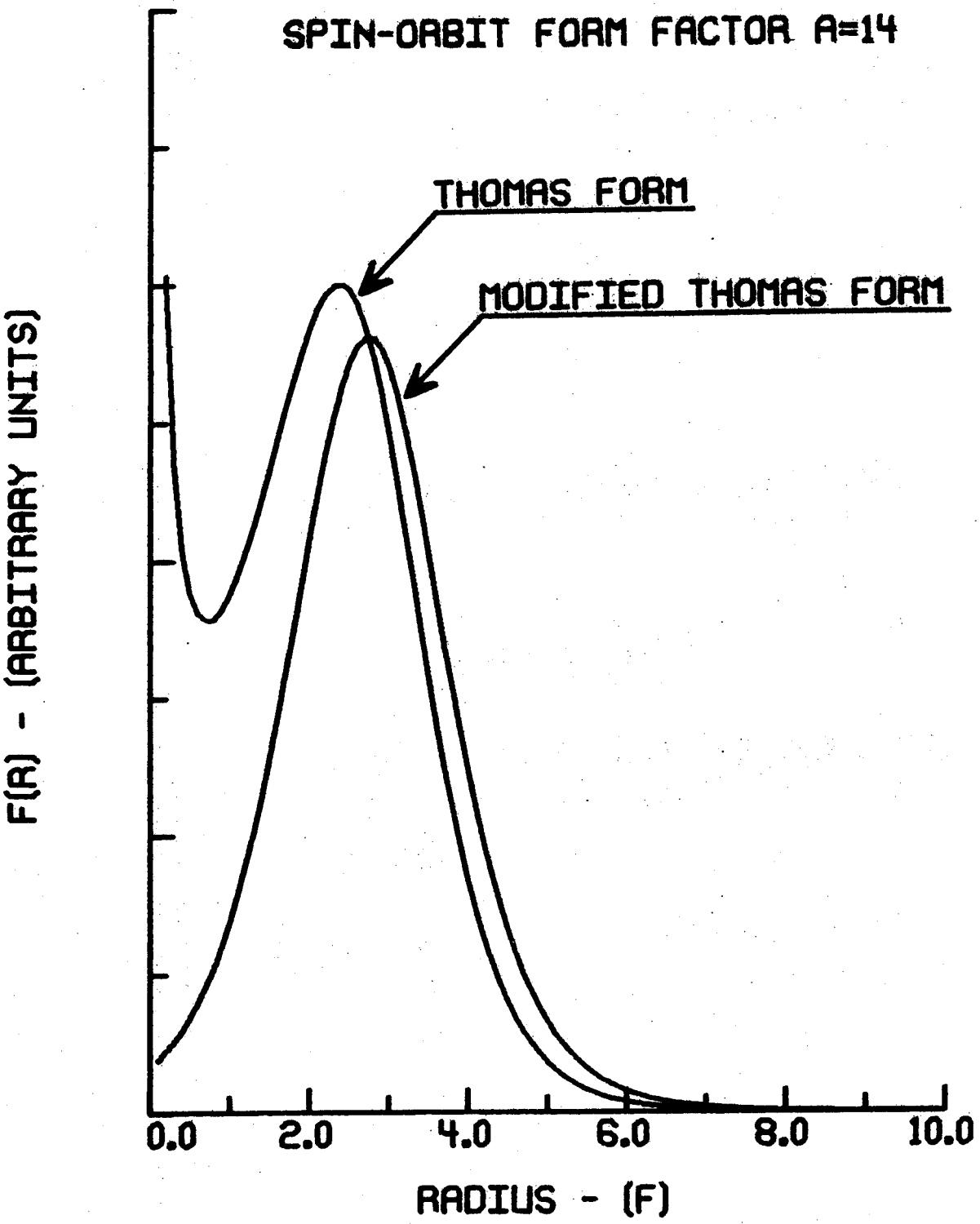

FIGURE 36. Radial dependence of the Thomas form of the spin-orbit potential and of the Thomas form as modified by Watson et al. (Wa 69) for A = 14.

et al. in their optical model analysis of nucleon scattering from a number of 1p-shell nuclei. The parameters found by Watson et al. are listed below.

V_R - (MeV) $60.0 - 0.30\ E_{CM} + 0.4Z/A^{1/3} + 27\ (N-Z)/A$

W_D - (MeV) 0, for $E_{CM} < 32.7$ MeV; $(E_{CM} - 32.7) \times 1.15$, for $32.7\ \text{MeV} \leq E_{CM} \leq 39.3$ MeV; and 7.5, for $E_{CM} > 39.3$ MeV

W_S - (MeV) $0.64\ E_{CM}$ for $E_{CM} < 13.8$ MeV; $9.6 - 0.06\ E_{CM}$ for $E_{CM} \geq 13.8$ MeV

V_{SO} - (ME) 5.5

$a_R = a_{SO} = 0.57$ (F) ; $a_I = 0.50$ F

$r_R = r_I = r_{SO} = 1.15 - 0.001\ E_{CM}$ F

The parameters are found in Table (29) and the calculated angular distributions in Figures (37) and (38). While not as good as the fits presented earlier, they do reproduce the main features of the angular distributions. The minima seem to be deeper with the Watson parameters than they are in either the data or in the fits with the parameters presented in this work.

When the 24.9 and 29.8 MeV angular distributions were fit with the average geometry parameters but free spin-orbit potential geometry parameters, the fits improved at backward angles but the well radii went to large values and the diffusenesses became small. The resultant parameters are found in Table (30) and the fits in Figure (39). Since the spin-orbit force is a short range force, radii larger than

TABLE 29. ^{14}N optical model parameters from Watson *et al.* (Wa 69)

E_p LAB (MeV)	24.8	29.8	36.6	40.0
V_R (MeV)	54.17	52.8	51.0	50.0
r_R (F)	1.127	1.122	1.116	1.113
a_R (F)	0.57	0.57	0.57	0.57
W_S (MeV)	0.0	0.0	1.6	5.28
W_D (MeV)	8.2	7.9	7.6	7.4
r_I (F)	1.127	1.122	1.116	1.113
a_I (F)	0.50	0.50	0.50	0.50
V^*_{SO} (MeV)	1000.0**	1000.0	1000.0	1000.0
r_{SO} (F)	1.127	1.122	1.116	1.113
a_{SO} (F)	0.57	0.57	0.57	0.57
r_C (F)	1.25	1.25	1.25	1.25
χ^2/N	24	25	35	43

* Modified Thomas spin-orbit potential.

** Strength for proton mass in force coefficient.

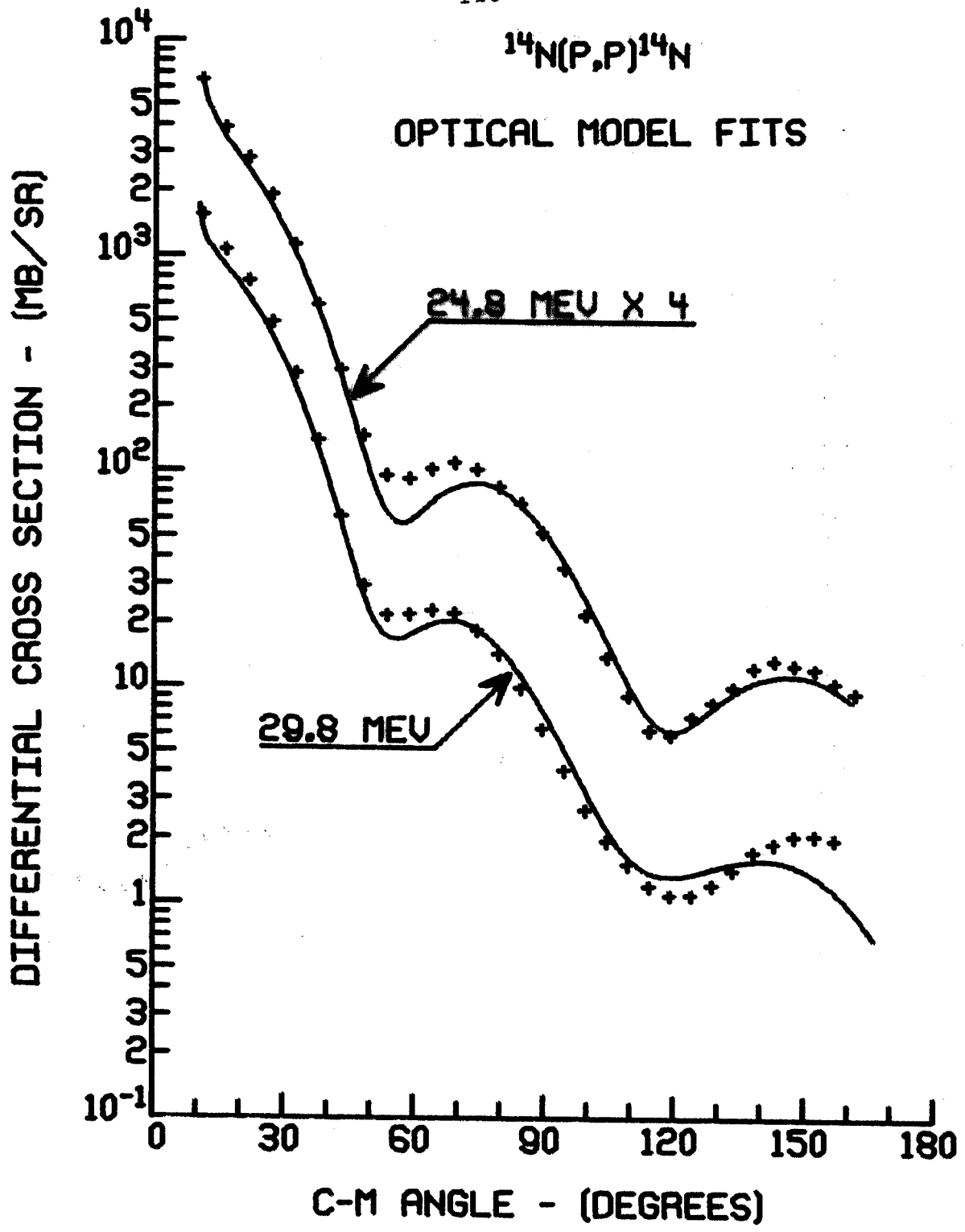

FIGURE 37. Optical model fits to the 24.8 and 29.8 MeV ^{14}N elastic scattering for the geometry and parameters from the work of Watson et al. (Wa 69).

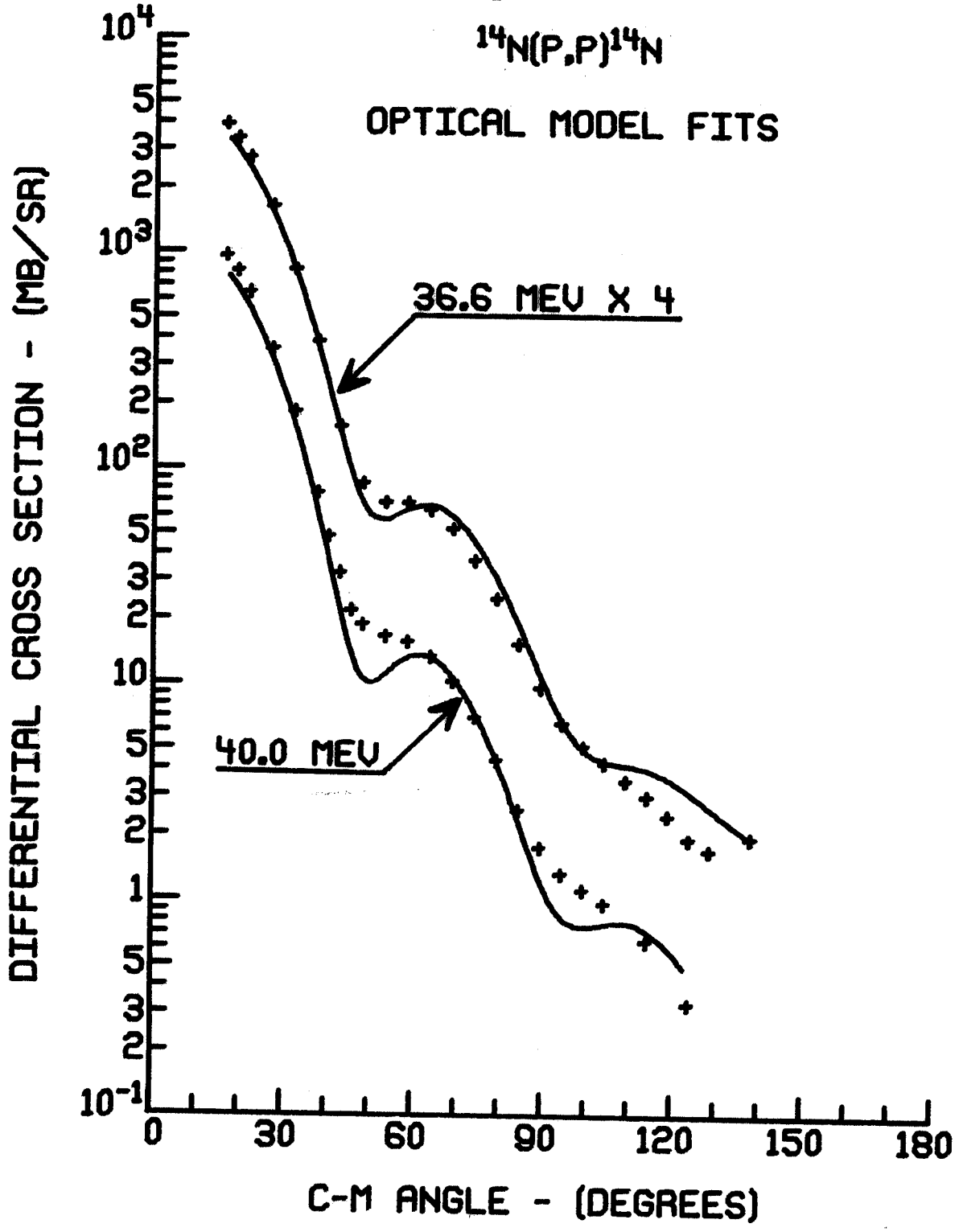

FIGURE 38. Optical model fits to the 36.6 and 40.0 MeV ^{14}N elastic scattering for the geometry and parameters from the work of Watson et al. (Wa 69).

TABLE 30. ^{14}N optical model results for free spin-orbit geometry parameters.

	GIBELUMP*		GIBPRIME**	
E_p LAB (MeV)	24.8	29.8	24.9	29.8
V_R (MeV)	52.19	49.09	52.40	49.34
r_R (F)	1.133	1.133	1.133	1.133
a_R (F)	0.651	0.651	0.651	0.651
W_S (MeV)	1.56	2.93	1.53	2.93
W_D (MeV)	4.75	3.52	4.69	3.63
r_I (F)	1.345	1.345	1.345	1.345
a_I (F)	0.509	0.509	0.509	0.509
V_{SO} (MeV)	4.20	5.29	3.91	5.08
r_{SO} (F)	1.42	1.35	1.30	1.33
a_{SO} (F)	0.449	0.450	0.394	0.350
r_C (F)	1.25	1.25	1.25	1.25
χ^2/N	6.7	20.0	6.4	14.0

* Thomas spin-orbit form.

** Modified Thomas spin-orbit form.

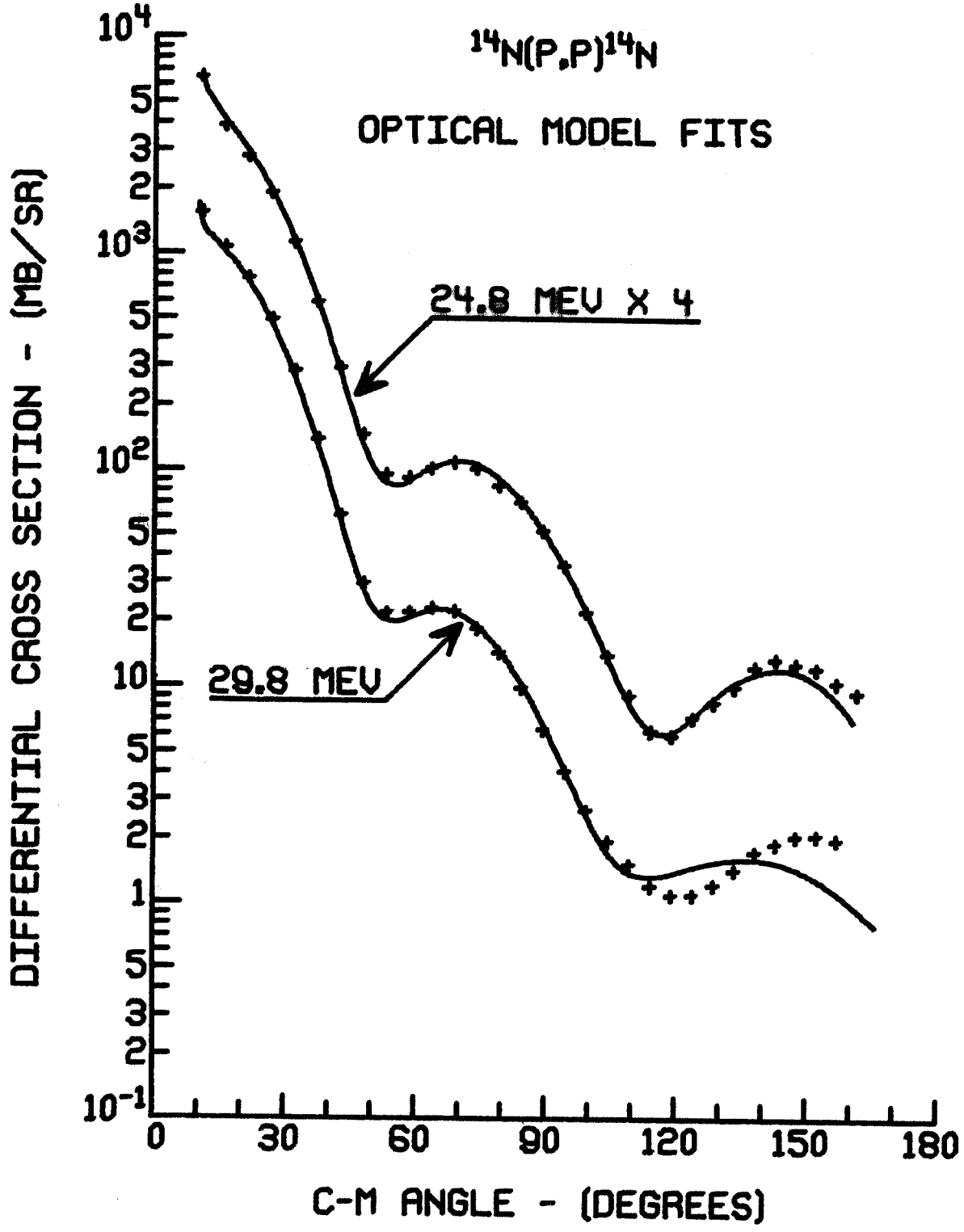

FIGURE 39. Optical model fits to the 24.8 and 29.8 MeV ^{14}N elastic scattering. The spin-orbit potential has the Thomas form with parameters varied to best fit the data.

that of the real well seem unrealistic. It seemed possible that the large radii and small diffusenesses were choosen by the search procedure because they would minimize the singularity at the origin and more nearly reproduce the form for the spin-orbit potential that results for large A nuclei.

The 24.9 and 29.8 MeV data were also fit with free spin-orbit geometry parameters and the code GIBPRIME. As the results in Table(30) indicate the spin-orbit radii that best fit the data were again much larger than the real well radius although not as large as with the unmodified Thomas form for the spin-orbit well. The fits obtained with GIBPRIME were only moderately better.

4.5 Variation of Well Strengths with Energy

In Figure(40) the potential strengths are plotted as a function of incident proton energy in the laboratory. The real well depth decrease with bombarding energy and the slope of a least squares fit to a straight line is -0.50. The depth of the surface imaginary well decreases with increased bombarding energy and that of the volume imaginary well increases. This is as expected from other optical model analyses.

The real well geometry found in this work is similar to that used by Snelgrove and Kashy (Sn 69) to fit proton elastic scattering from ^{15}N at 39.84 MeV. The slope of the

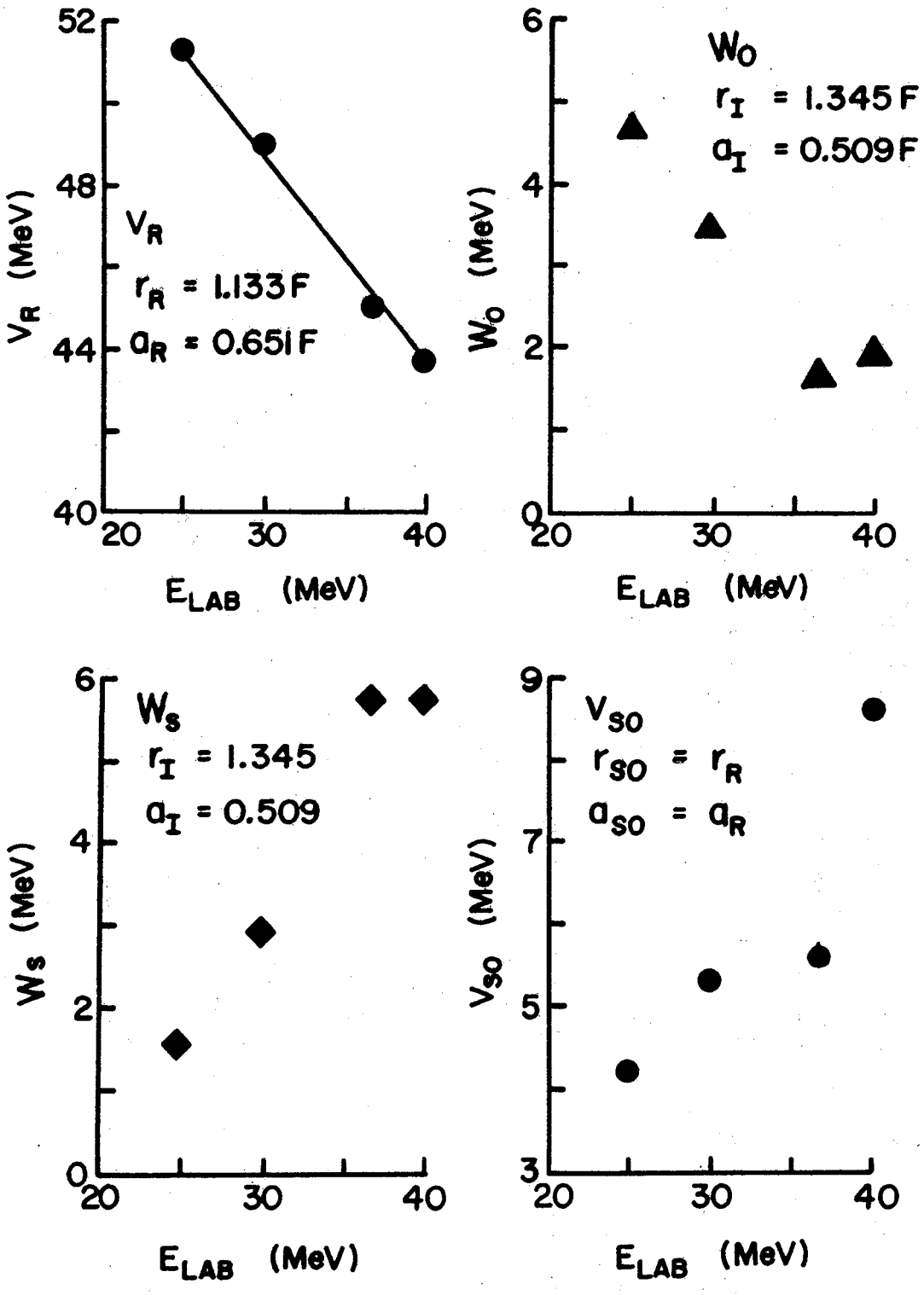

FIGURE 40. Variation of the strengths of the optical model potential found in this work as a function of energy.

real well depth vs. proton incident energy plot for this analysis is closer to that found by Perey (Pe 63) in an optical model analysis of proton elastic scattering on target nuclei between ^{27}Al and ^{197}Au (-0.55) than it is to that found by van Oers and Cameron (Oe 69) in an analysis of 23-50 MeV protons on ^{16}O (-0.29) or that found by Watson et al. (Wa 70) in an analysis of 20-50 MeV protons on a number of 1p-shell nuclei (-0.30 for incident proton energy measured in the c. m. frame).

5. MICROSCOPIC MODEL CALCULATIONS

5.1 DWBA 70A

The microscopic model DWBA calculations made for this work were done with the code DWBA 70A (Sc 70). The nuclear force can include tensor and spin-orbit terms and the exchange amplitude can be included exactly. The required spectrocopic amplitudes, equivalent to those described by Madsen (Ma 66) were calculated with the code MULTISCAT, part of the Oak Ridge-Rochester (Fr 69) shell model code modified by Duane C. Larson.

DWBA 70 used the neutron-proton formalism for the interaction. For a proton incident on a proton the force is:

$$V_{pp} = V^1_p + V^2_p \quad Y(r, \mu_1) + V^3_p \quad Y(r, \mu_2)\ (\vec{\sigma}_1 \cdot \vec{\sigma}_2) + V^4 \quad Y(r, \mu_3)\ \vec{L}\cdot\vec{S} + V^5_p\ r^2 \quad Y(r, \mu_4)\ S_{12}$$

and for a proton incident on a neutron:

$$V_{pn} = \quad V^2_n \quad Y(r, \mu_1) + V^3_n \quad Y(r, \mu_2)\ (\vec{\sigma}_1 \cdot \vec{\sigma}_2) + V^4_n \quad Y(r, \mu_3)\ \vec{L} \cdot \vec{S} + V^5_n\ r^2 \quad Y(r, \mu_4)\ S_{12}$$

V^1_p is the coulomb potential and S_{12} is the usual tensor operator. The $Y(r, \mu_i)$'s are Yukawa's

$$Y(r, \mu_i) = \frac{e^{-r/\mu_i}}{r/\mu_i}$$

5.2 Wave Functions

There is evidence that the tensor force plays an important role in the A-14 system. The ^{14}C beta decay is allowed by selection rules, but is suppressed because of the particular nature of the wave functions involved. Visscher and Ferrell (Vi 57) have shown that suppression of the ^{14}C beta decay can be obtained with 1p shell wave functions only if they are generated with a residual interaction that includes a tensor term. Also Rose et al. (Ro 68) have shown that expanding the model space into the 2s-1d shell will not eliminate the need for including the tensor force.

Available ^{14}N shell model wave functions fall into two classes depending on the model space used. There are the wave functions of Visscher and Ferrell (Vi 57) and those of Cohen and Kurath (Co 65) that assume a closed ^{4}He core and 8 particles in the 1p shell, and there are the wave functions of True (Tr 63) and those of Reehal, Wildenthal, and McGrory (Re 72) that assume a ^{12}C closed core and two particles distributed among the $1p_{\frac{1}{2}}$ orbital and orbitals of the 2s,1d shell. A better space for ^{14}N would be a combination of the two, that is the latter space with two or four holes in $1p_{3/2}$ orbital. Such a space would be very large but there is some hope of doing such calculations at least for the 0+ states.

5.2.1 1 P Shell Wave Functions

The 1p shell space used by Visscher and Ferrell (V-F) and by Cohen and Kurath (C-K) contains the dominant configurations of the ground state and the excited states at 2.31, 3.95, and 7.03 MeV (Ma 68) (see Table 31). In the V-F calculation, the tensor force and the L•S force are explicitly included in the residual interaction while uncertainties in the central potential are removed by fitting the energy levels of the first three states in ^{14}N and the ^{14}C beta decay rate. In the C-K calculation the 15 two body matrix elements and the two single particle energies needed were obtained by fitting energy levels and binding energies of the ground states with respect to the $(1s)^4$ core. One set of parameters was obtained using energy levels in nuclei between A=6 and A=16 and another set using energy levels in nuclei between A=8 and A=16. Because the results for A=6 and 7 were not as good as those for the other nuclei fit, the latter set of parameters was judged best for ^{14}N. The wave functions generated with this set of parameters gave a log ft for ^{14}C Gamow-Teller beta decay of 5.42 compared to the experimental value of 9.02 (Ba 66). Although there are 4 orders of magnitude difference between the two numbers both values represent a decay rate that is strongly suppressed. Only wave functions that reproduce the suppression of this beta decay rate are of any value in the study of the

TABLE 31. ^{14}N wave functions.

Energy (MeV)	Reference	Calculated Energy (MeV)						
0.0			$(P_3)^{-2}$	$(P_3, P_1)^{-1}$	$(P_1)^{-2}$			
$(1^+, 0)$	C - K (1)	0.0	0.027	0.313	0.949			
	V - F (2)	0.0	0.119	0.362	0.926			
			$(P_1)^2$	$(S_1)^2$ $(D_5)^2$		(S_1, D_3)	(D_3, D_5)	$(D_3)^2$
	TRUE (3)	0.0	0.967	0.064 0.184		0.101	0.011	-0.132
	R-W-M (4)	0.0	0.987	-0.117 0.136				
2.31			$(P_3)^{-2}$	$(P_1)^{-2}$				
$(0^+, 1)$	C - K	2.47	0.384	0.923				
	V - F	(2.40)	0.250	0.968				
			$(P_1)^2$	$(S_1)^2$	$(D_5)^2$		$(D_3)^2$	
	TRUE	2.94	-0.950	-0.122	-0.263		0.114	
	R-W-M	2.75	0.896	-0.158	-0.415			
3.94			$(P_3)^{-2}$	$(P_3, P_1)^{-1}$	$(P_1)^{-2}$			
$(1^+, 0)$	C - K	3.91	0.364	-0.888	0.282			
	V - F	3.14	0.043	0.931	-0.367			
4.91			(P_1, S_1)					
$(0^-, 0)$	TRUE	3.31	1.000					
	R-W-M	4.48	1.000					
5.11			(P_1, D_5)	(P_1, D_3)				
$(2^-, 0)$	TRUE	4.83	0.983	0.184				
	R-W-M	4.75	1.000					
5.69			(P_1, S_1)	(P_1, D_3)				
$(1^-, 0)$	TRUE	4.90	0.993	0.117				
	R-W-M	5.63	1.000					

TABLE 31 (con't.)

5.83			(P_1, D_5)					
$(3^-, 0)$	TRUE	5.60	1.000					
	R-W-M	5.69	1.000					
6.20			$(P_1)^2$	$(S_1)^2$	$(D_5)^2$	(S_1, D_3)	(D_3, D_5)	$(D_3)^2$
$(1^+, 0)$	TRUE	6.34	0.130	-0.873	-0.327	0.020	-0.331	0.063
	R-W-M	4.82	0.039	0.878	0.474			
6.44			(S_1, D_5)	$(D_5)^2$	(D_3, D_5)	$(D_3)^2$		
$(3^+, 0)$	TRUE	7.61	-0.897	-0.408	-0.167	0.031		
	R-W-M	6.36	0.841	0.542				
7.03			$(P_3, P_1)^{-1}$					
$(2^+, 0)$	C - K	7.05	1.000					
7.97			(P_1, D_5)	(P_1, D_3)				
$(2^-, 0)$	TRUE	7.89	0.184	-0.983				
8.06			(P_1, S_1)	(P_1, D_3)				
$(1^-, 1)$	TRUE	7.26	-0.995	0.105				
	R-W-M	8.14	1.000					
8.49			$(P_3)^{-1}, (P_1)^2, (D_5)$					
$(4^-, 0)$	Ma 68		1.000					

1) Co 65
2) Vi 57
3) Tr 63
4) Re 72
5) $P_3 = P_{3/2}$, $P_1 = P_{1/2}$, $D_5 = D_{5/2}$, $S_1 = 2\,S_{1/2}$, $D_3 = D_{3/2}$

^{14}N ($p_{\frac{1}{2}}p^{\frac{1}{2}}$) $^{14}N^*$ (E_X = 2.31) reaction.

5.2.2 ^{12}C Core Plus sd Shell Wave Functions

The model space used in the shell model calculation for ^{14}N published by True consists of a ^{12}C core and two nucleons free to move in the $1p_{1/2}$ $2s_{1/2}$, $1d_{5/2}$, or $1d_{3/2}$ orbitals. The single particle energies are taken from the energies of levels in ^{13}C and ^{13}N and the residual interaction between the valance neutron and proton is taken as a central force made up of singlet-even and triplet-even components. The radial dependence of the force is Gaussian with strength and range chosen so that the singlet-even force is the same as that used successfully by True and Ford in ^{208}Pb. Two parameters, the ratio of the triplet-even force to the singlet-even force and the harmonic oscillator parameter of the single particle wave functions were chosen to obtain the best fit to the levels in ^{14}N. The model space contained the dominant configurations of all the states in ^{14}N below 8.49 MeV in excitation except for the 3.95, 7.03 and 8.49 MeV states.

In the shell model calculation by Reehal, Wildenthal and McGrory (Re 72) ^{12}C is taken as a closed core and the valence nucleons are free to populate the $1p_{1/2}$, $2s_{1/2}$, and $1d_{5/2}$ orbitals. The single particle energies and the two body matrix elements were obtained by fitting energy levels

of states in nuclei between A=13 and A=22 that should be reproduced within the model space. These calculations would not be expected to reproduce the ^{14}C beta decay and so their wave functions for the 2.31 MeV state would not be expected to reproduce inelastic scattering.

5.3 Coupled Channels Calculations

The DWBA approach to inelastic scattering is essentially a peturbation approach that assumes that elastic scattering is the dominant process and that it is sufficient to treat inelastic scattering as a first order peturbation. If there are other channels that can compete strongly with the elastic scattering, DWBA is not valid. DWBA will also fail to describe interactions for which higher than first order processes are important. An alternative for such cases is the coupled-channels approach (Ta 65) in which the total wave function is expanded in terms of wave functions for all the important channels. In the coupled channels approach the interaction is not treated to first order only but to infinite order within the space defined by the channels included (Ta 65).

It was not practical to do a coupled channels calculation here, but there is evidence that such a calculation would not be a great improvement over DWBA for the ^{14}N (p,p') $^{14}N^*$ (2.31 MeV) reaction for the incident proton

energies involved here. F. A. Schmittroth (Sc 68) did a coupled channels calculation for the A-14 system and compared the results to DWBA for the reaction $^{14}C\ (p,n)\ ^{14}N$ for 14.1 MeV incident proton energy. This reaction is the parallel to the $^{14}N\ (p,p')\ ^{14}N$ (2.31 MeV) reaction. The channels coupled were $^{14}C + p$, $^{14}N + n$, $^{14}N^*$ (2.31) + n, and $^{14}N^*$ (3.95) + n. For the $^{14}N\ (p,p')\ ^{14}N$ (2.31 MeV) reaction the appropriate channels to couple would be $^{14}O + n$, $^{14}N + p$, $^{14}N^*$ (2.31) + p, and $^{14}N^*$ (3.95) + p. To within the 20% accuracy of the DWBA calculation there was no effect on the $^{14}C\ (p,n)\ ^{14}N$ transition due to coupling. Since the effects of coupling should decrease with increasing proton bombarding energy (Ma 71), coupling should not be important for the $^{14}N\ (p,p')\ ^{14}N$ (2.31 MeV) reaction at the energies of this work.

5.4 Two-Step Processes

For a relatively weak interaction like the $^{14}N\ (p,p')\ ^{14}N^*$ (2.31 MeV) reaction [its strength is 1/10 that of $^{14}N\ (p,p')\ ^{14}N^*$ (3.95 MeV)] the contribution of the two-step processes such as $^{14}N\ (p,d)\ ^{13}N\ (d,p)\ ^{14}N^*$ (2.31 MeV) should be considered. Calculation of such processes are very difficult. No proven computer code was available for such a calculation at M.S.U. and so we did not have the opportunity to look into such processes.

5.4 Nuclear Forces

A number of different combinations of central, tensor, and spin-orbit forces were tried in DWBA calculations for the 2.31 MeV state inelastic scattering. Since the shape of the calculated cross section is controlled by the interplay of the central and tensor force, central and tensor forces that had some connection to realistic forces were favored. Thus most of the calculations were in some sense apriori.

5.4.1 Fitting Central Interactions to the Yukawa Radial Form

Where necessary the strength and range of the Yukawa potential corresponding to a given central potential was found by matching the volume integral and r^2 integral of that given force to those of the corresponding Yukawa. The ranges for different terms of a given potential and for the corresponding Yukawa's terms were often different (see Table 32). It was generally possible to choose some average range for the Yukawa potentials and calculate the strength from the volume integrals. This cut down calculation time. Check calculations were made to insure that the cross sections predicted by the average range potentials did not differ greatly from those predicted by the original potentials.

5.5.2 Serber Central Potential (S)

A Serber central interaction(S) (V_{00}: V_{01}: V_{10}: V_{11} = -3:1:1:1) with a V_{11} strength of 3.47 MeV was taken from the work of Love et al. (Lo 70a). The range, μ, had been taken to be the pion wavelength (1.415 F) and the strength chosen to best describe the small momentum components of the truncated Hamada-Johnston potential. Contributions to V_{00} central forces arising from second order tensor force terms were included.

5.5.3 Even State Hamada-Johnston Central Potential (HJ)

A central force with a non-Serber mixture was obtained from the even parts of the Hamada-Johnston (Ha 62) potential (HJ). The volume and r^2 integrals were done following the Moszkowski-Scott separation procedure with a cut off distance of 1.05 F. The results are found in Table(32).

5.5.4 Even State Hamada-Johnston Potential Plus ^1P State Gaussian Potential (HJ-G)

The Moszkowski-Scott separation procedure applies only to the even parts of the Hamada-Johnston potential. Owen and Satchler (Ow 70) replaced the ^1P state Hamada-Johnston potential by a repulsive Gaussian [V = 120 exp

TABLE 32. Central and tensor forces.

Potential	S	HJ	HJ μ = 1.0	G	G μ = 1.0	BJ	SMA	HJ-T cut-off= 0.49F	OPEP
V_{00} (MeV)	-10.41	-24.8	-29.6	+138.2	+ 4.51	-16.85	-28.0		
μ_{00} (F)	1.415	1.06		0.327		1.359	1.0		
V_{01} (MeV)	3.47	12.8	12.2	-138.2	- 4.51	7.28	11.0		
μ_{01} (F)	1.415	0.98		0.327		1.359	1.0		
V_{10} (MeV)	3.47	4.6	7.5	-138.2	- 4.51	3.95	11.0		
μ_{10} (F)	1.415	1.18		0.327		1.359	1.0		
V_{11} (MeV)	3.47	8.3	9.9	+138.2	+ 4.51	5.62	11.0		
μ_{11} (F)	1.415	1.06		0.327		1.359	1.0		
V_T^* (MeV)								-0.40	0
μ_T (F)								0.843	0.8159
$V_{T\lambda}^{**}$ (MeV)								8.1	11.01
$\mu_{T\lambda}$ (F)								0.843	0.8159

* Isospin transfer = 0
** Isospin transfer = 1

$(-0.78\ r^2)$ MeV] adjusted to fit the ^1P phase shifts. The ^3P state potential was taken as zero. The volume and r^2 integrals for the Gaussian potential were calculated and used together with those for the even state Hamada-Johnston to produce a composite central interaction containing odd state interactions (HJ-G).

5.5.5 Blatt-Jackson Central Potential (BJ)

And finally the Blatt-Jackson even state nucleon-nucleon interaction was used. This potential has the form

$$V = + V_0 \frac{e^{-r/\mu}}{r/\mu}$$

with the following parameters

for $^1S_0$: $V = -32.5$ MeV, $\mu = 1.435$ F

for $^3S_0$: $V = -67.8$ MeV, $\mu = 1.241$ F

The virtue of this potential is that it has a Yukawa radial form and so it can be used directly.

5.5.6 Effective Average Effective Central Interaction (SMA)

Another central interaction that was used came from a survey of inelastic proton scattering by Sam Austin (SMA) (Au 70). The strengths of V_{00} and V_{11} are fairly well defined, but those of V_{10} and V_{01} are not so certain. Thus V_{10} and V_{01} were taken to be equal to V_{11}.

Since nuclear interactions are presented in a number of different expansions, the transformations from the odd-even, singlet-triplet formalism to spin-isospin formalism and to the neutron-proton formalism used by DWBA 70 are found in Appendix A2.

5.5.7 Tensor Forces

Calculations with two tensor forces were considered. The one-pion-exchange-potential (OPEP)

$$V_T(r) = V_{T\tau}\ \vec{\tau}_1 \cdot \vec{\tau}_2\ S_{12}\ f(\alpha)$$

$$f(\alpha) = \left(1 + \frac{3}{\alpha r} + \frac{3}{(\alpha r)^2}\right) \frac{e^{-\alpha r}}{\alpha r}$$

$$S_{12} = 3(\vec{\sigma}_1 \cdot \vec{r})(\vec{\sigma}_2 \cdot \vec{r}) - \vec{\sigma}_1 \cdot \vec{\sigma}_2$$

where $\alpha^{-1} = \left(\frac{\hbar}{M_\pi c}\right) = 1.415$ F is the Compton wavelength of the pion and $V_{T\tau} = 3.76$ (Co 65) was one of these. The second was taken from the Hamada-Johnston potential (Ha 62)

$$V_T = 3.76\ (\vec{\tau}_1 \cdot \vec{\tau}_2)\ Z(r) \cdot [1 + a_T\ Y(r) + b_T\ Y^2(r)] \cdot S_{12}$$

$\mu^{-1} = 1.415$ F the Compton wavelength of the pion

$$Z(r) = (1 + 3\mu/r + 3\mu^2/r^2)\ Y(r)$$

$$Y(r) = \frac{e^{-r/\mu}}{r/\mu}$$

The quantities a_T and b_T determine the difference of the potential from OPEP for small r and have the values $a_T = -0.5$ and $b_T = .2$ for the triplet even tensor force and $a_T = -1.29$ and

b_T = +0.55 for the triplet odd.

DWBA 70A has a r^2 - Y tensor radial form built in, however it has been shown that the first two terms of the Fourier transform of the tensor and spin-orbit forces are proportional to the integrals (Sc 71).

$$J_4 = \int r^4 \; V(r) \; dr$$

$$J_6 = \int r^6 \; V(r) \; dr$$

These integrals were used to estimate the strengths and ranges of the r^2 - Y forms of the tensor forces that correspond to the OPEP and the long range part of the Hamada-Johnston potential. For OPEP the lower limit of the integration was r = o but for the hard core Hamada-Johnston tensor potential the integrals went in to r = 0.49 F. This was as close to the hard core radius (0.485 F) as it was possible to conveniently integrate. The tensor force is nearly independent of this choice and is similar to OPEP, in that $V_{T\tau}$ (the strength for a ΔT=1 reaction) is much greater than V_T (the strength for a ΔT=0 reaction). (See Table 32.)

5.5.8 Spin-Orbit Potential

A spin-orbit potential was derived from the Hamada-Johnston spin-orbit potential by matching the J_4 and J_6 integrals of the two terms of this potential to the same integrals of two Yukawas. Perhaps the best estimate of the strength was obtained for a cut of distance of 0.49 F. In

Table (33) are listed the J_4 integrals for a number of spin-orbit potentials taken from the literature (Au 72). The strength of the Hamada-Johnston spin-orbit force with a 0.49 F cut off radius is in good agreement with the forces used by Love and that used by Austin. While the J_4 integral for the spin-orbit potential implied by the empirical optical model is larger, it is difficult to estimate the effect of exchange for this potential.

5.5.9 "Complete" Hamada-Johnston

J.-L. Escudie, F. G. Resmini, and Y. Terrien (Es 72) have made an attempt to fit the Fourier transform of the long range part of the complete Hamada-Johnston potential except for the quadratic spin-orbit term to Yukawa's and r^2 - Yukawa's using three separate ranges for the Yukawas. The central potential is for a separation distance of 1.05 F and corrections for 2nd order tensor terms are included. The cutoff for determining the tensor force was 0.5 F and for the LS force 0.7 F. Thus one expects that their L·S force is perhaps too weak. The method of conversion was by fitting Fourier Transforms in a manner similar to that described earlier.

TABLE 33. Values of the spin-orbit force.*

Determination	J_4 (T = 0) (MeV - F^5)	J_4 (T = 1) (MeV - F^5)
Optical Model		
V_{SO} = 6.7 MeV [a]	-80	—
Love ^{90}Zr (p,p') [b]	-37.6	-15.2
^{16}O(p,p') ^{16}O (8.87, 2^-, 0) [c]	-50.8	-32.2
HJ [d] r_C = 1.0 F	- 7.3	- 6.5
r_C = 0.6 F	-27.7	-13.7
r_C = 0.49	-34.9	-16.2

a) Ref Gr 68

b) Ref Lo 71

c) Ref Au 72

d) Sc 71

*LS form: $V_{LS} = [V_{LS}(T = 0) + V_{LS}(T = 1)\ \vec{\lambda}_1 \cdot \vec{\lambda}_2]\ \vec{l} \cdot \vec{s}$

5.5.10 Central Potential for Inelastic Scattering to States other than the 2.31 MeV State

For calculations for inelastic scattering to states other than the 2.31 MeV state a Serber central force with V_{11} = 3.47 MeV and range 1.415 was used. Here the test was of the wave functions and reaction theory.

6. RESULTS

6.1 Results for Calculations of Inelastic Scattering to the 2.31 MeV State

The results of DWBA 70 calculations for the central plus tensor forces described earlier are found in Figures (43 to 47). Certain characteristics are general to all these results. It is clear that central forces alone cannot reproduce the shape of the 2.31 MeV angular distribution. In Figure 47 we have the results for the Serber central force, S, direct and with exchange. These results are typical. The calculated shape is too broad with too gentle a slope at forward angles. The tensor force alone also cannot reproduce the shape of the data. The angular distributions calculated for OPEP alone are found in Figure (41). At 24.9 and 29.8 MeV these calculations overstate the shape of the experimental cross sections. At 36.6 and 40.0 MeV the situation is complicated. While OPEP alone does not fit the data, it seems to do slightly better at forward angles than central plus OPEP calculations. See Figure (47). The results for OPEP are very similar to those for the tensor force derived from the Hamada-Johnston tensor force (HJ-T). See Figure (42).

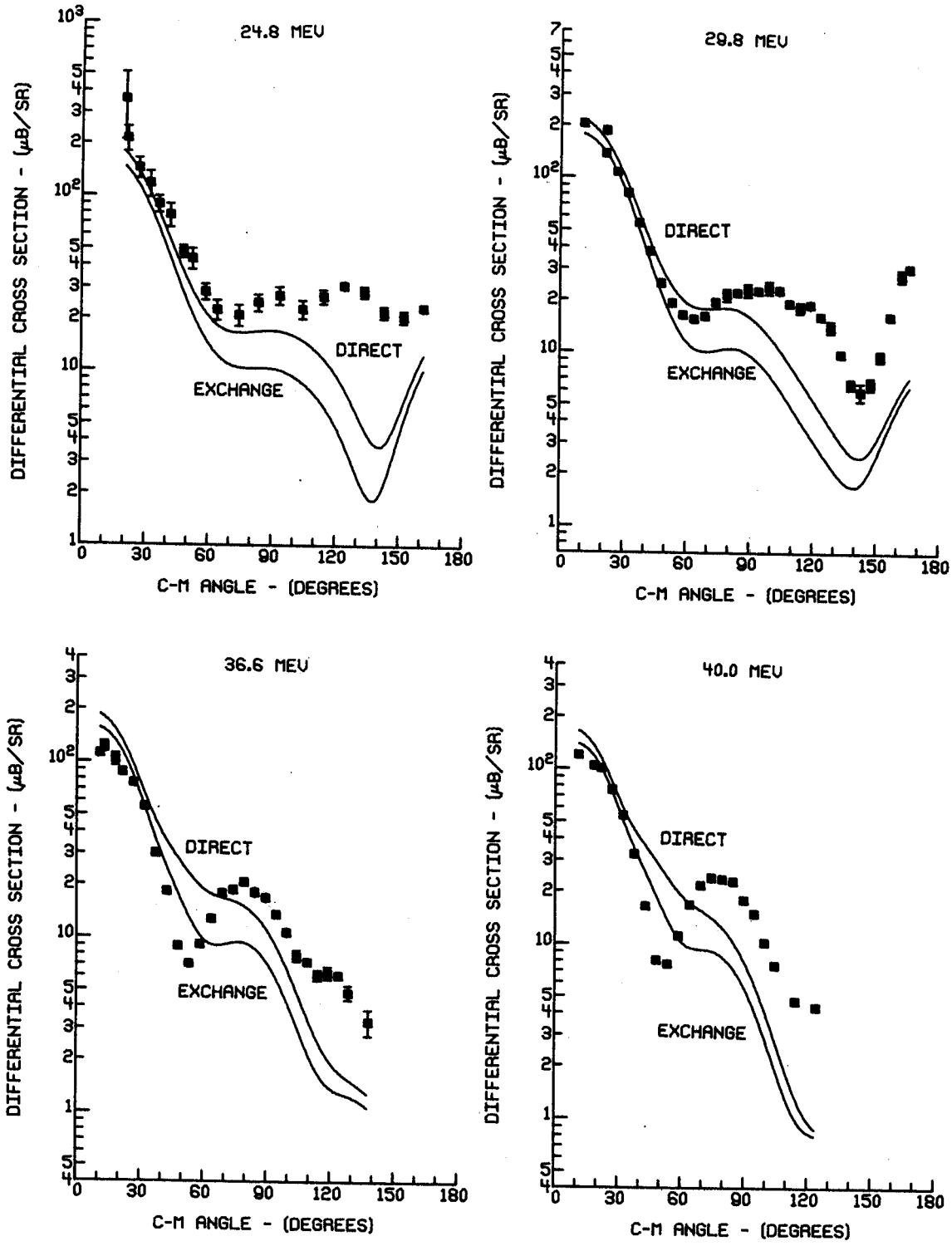

FIGURE 41. $^{14}N(p,p')^{14}N^*$ (2.31 MeV) calculations with OPEP alone.

While the final calculations were made with the Cohen-Kurath wave functions and optical model parameters obtained as part of this work, Visscher-Ferrell wave functions and other reasonable sets of optical model parameters yield essentially the same results. Calculations for Visscher-Ferrell wave functions are compared to those for the Cohen-Kurath wave functions at 29.8 and 40.0 MeV and calculations for the optical model used by Crawley et al. (Ca 70) are compared to those for the optical model parameters of the present work at the above energies in Figure(42).

The shape of the resultant calculations and the degree to which they agree with the data is mainly a function of the interplay of the central and tensor forces and the strength or range of the central force. At 24.8 and 29.8 MeV the central plus tensor direct calculations overstated the shapes of the experimental angular distributions. The rise at forward angles and the height of the second maxima in the calculated angular distributions were too great. In calculations with exchange at 24.8 and 29.8 MeV the shape is either reproduced well or washed out depending on the strength or range of the central interaction. For central plus tensor calculations at 36.6 and 40.0 MeV the direct results come closest to reproducing the tensor only shape and thus the data. With exchange included the shape of the results deteriorate in general except when the central interactions are weak. The inclusion of the spin-orbit force does not

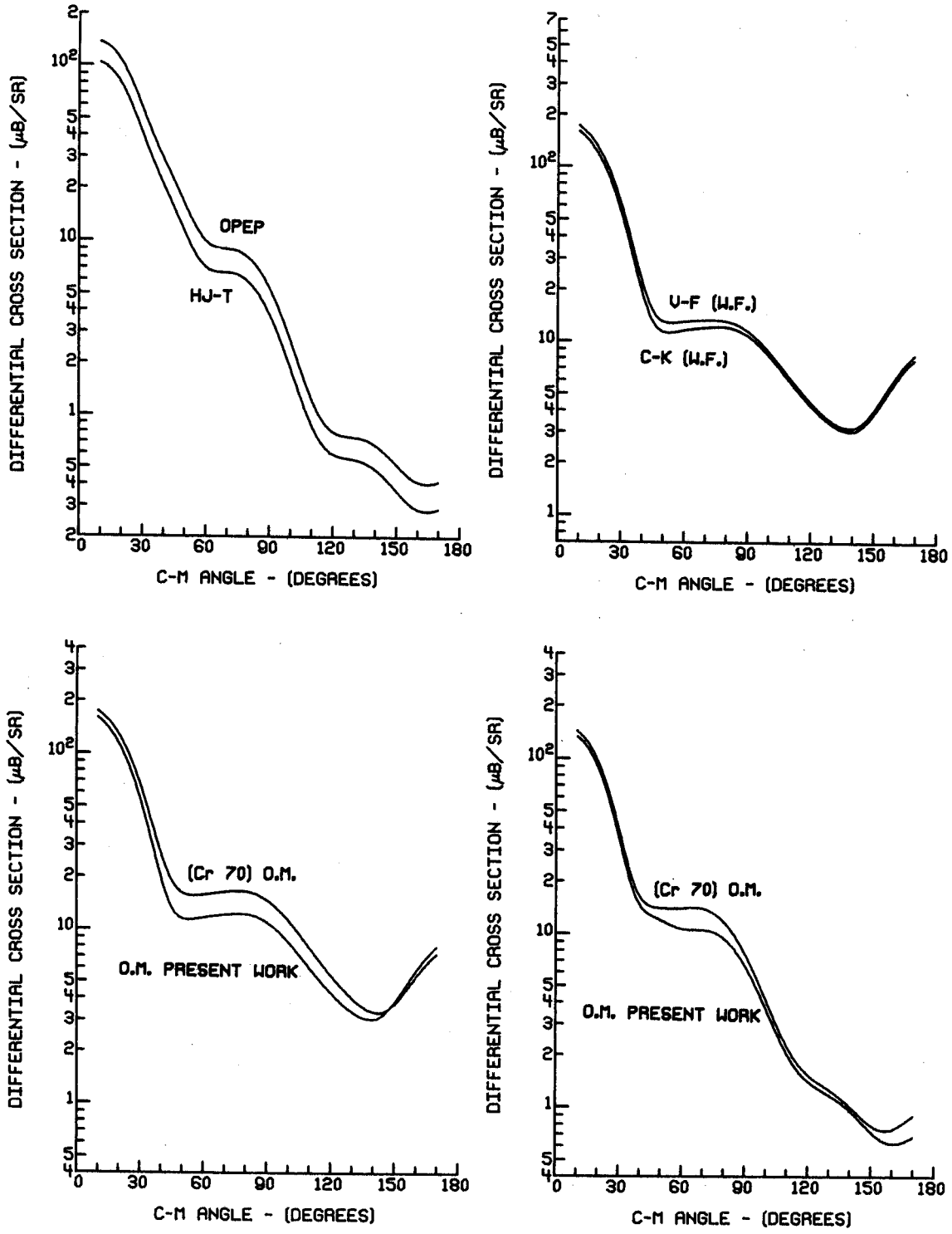

FIGURE 42. $^{14}N(p,p')^{14}N^*$ (2.31 MeV) calculations with: OPEP and HJ-T alone at 40.0 MeV (A); V-F and C-K wave functions with S + OPEP at 29.8 MeV (B); and optical model parameters of Cr 70 and this work with S + OPEP at 29.8 MeV (C) and 40.0 MeV (D).

TABLE 34. Comparison of central forces.

Central Force	HJ	HJ-G	BJ	SMA	S
Range (F)	1.0	1.0	1.359	1.0	1.415
σ_T calculated with exchange (mb) (E_p = 29.8 MeV)	0.483	0.217	0.492	0.536	0.214
Ordered by goodness of central + OPEP fit with exchange [a]	4	3	2	5	1

a) Fits to data rated by eye (1 = best)

change the shape of the results greatly. See Figure (48).

Of the central forces tried those most directly related to realistic forces were those taken from the even parts of the Hamada-Johnston potential (H-J); the central force made up of the H-J potential plus a Guassion singlet odd potential (HJ-G); and the central Blatt-Jackson potential (B-J). The results for the H-J and HJ-G plus the Hamada-Johnston tensor force (HJ-T) are found in Figures (43) and (44). The HJ-G potential was put together to see if a force with both odd and even components would make a noticeable difference. The HJ-G central is weaker than the H-J potential in calculation with exchange. The total cross section for the H-J at 29.8 MeV is 0.483 mb and that for the HJ-G is 0.217 mb. See Table (34). The HJ-G thus fits the shapes somewhat better, but the improvement is not great, and is probably due to the relative weakness of the force.

The results for the B-J potential plus OPEP are found in Figure (45). The H-J and B-J potentials are about equal in strength. The range of the B-J potential however is longer, μ = 1.359 F than the 1.0 F range H-J central. For the H-J plus HJ-T force the shape of the cross section for calculations with exchange is in poor agreement with the data at all energies, while for the B-J plus OPEP calculations the shape at 24.8 and 29.8 MeV is in good agreement with the data. The B-J central plus OPEP interaction does not do as well at 36.6 and 40.0 MeV.

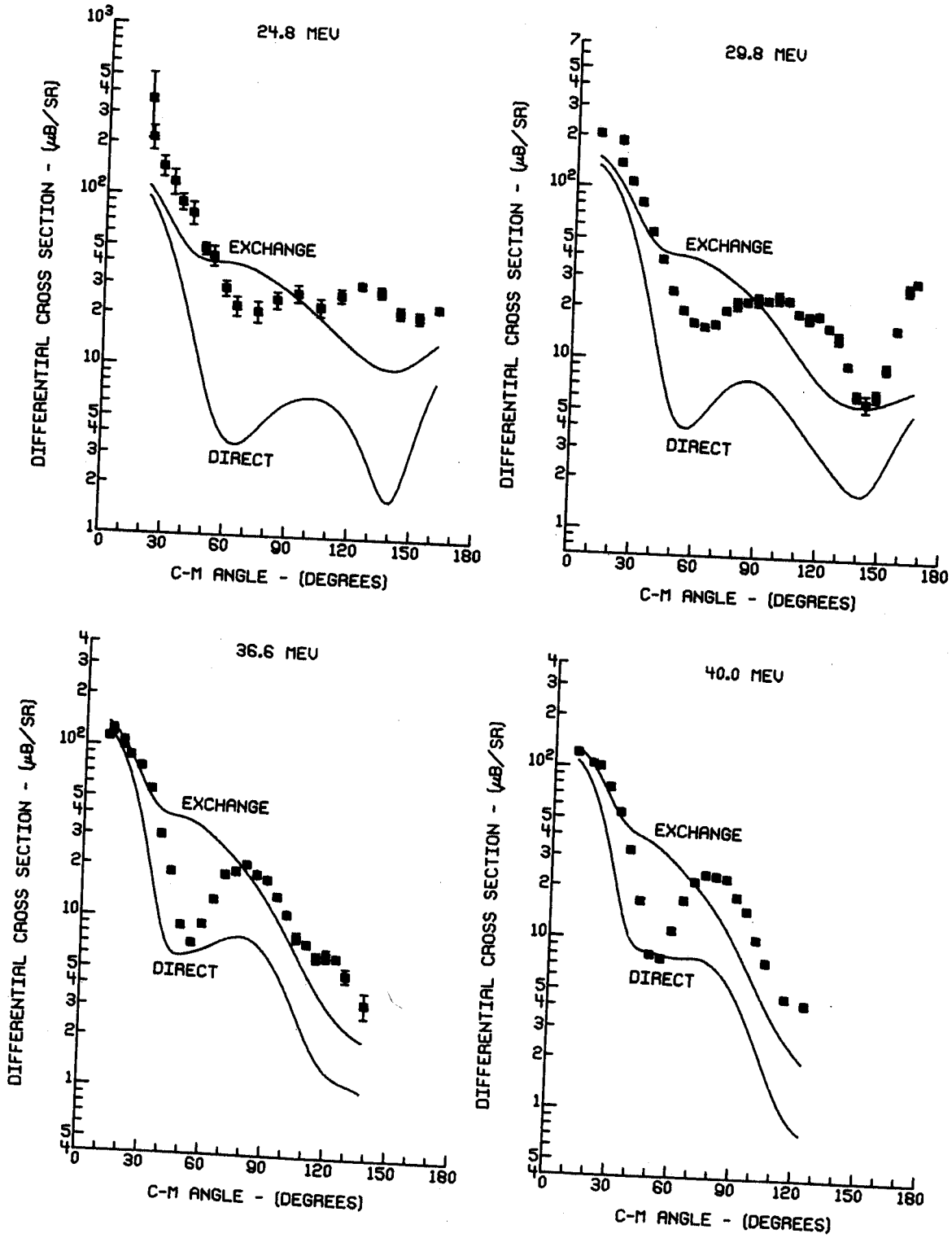

FIGURE 43. $^{14}N(p,p')^{14}N^*$ (2.31 MeV) calculations for HJ central plus HJ-T.

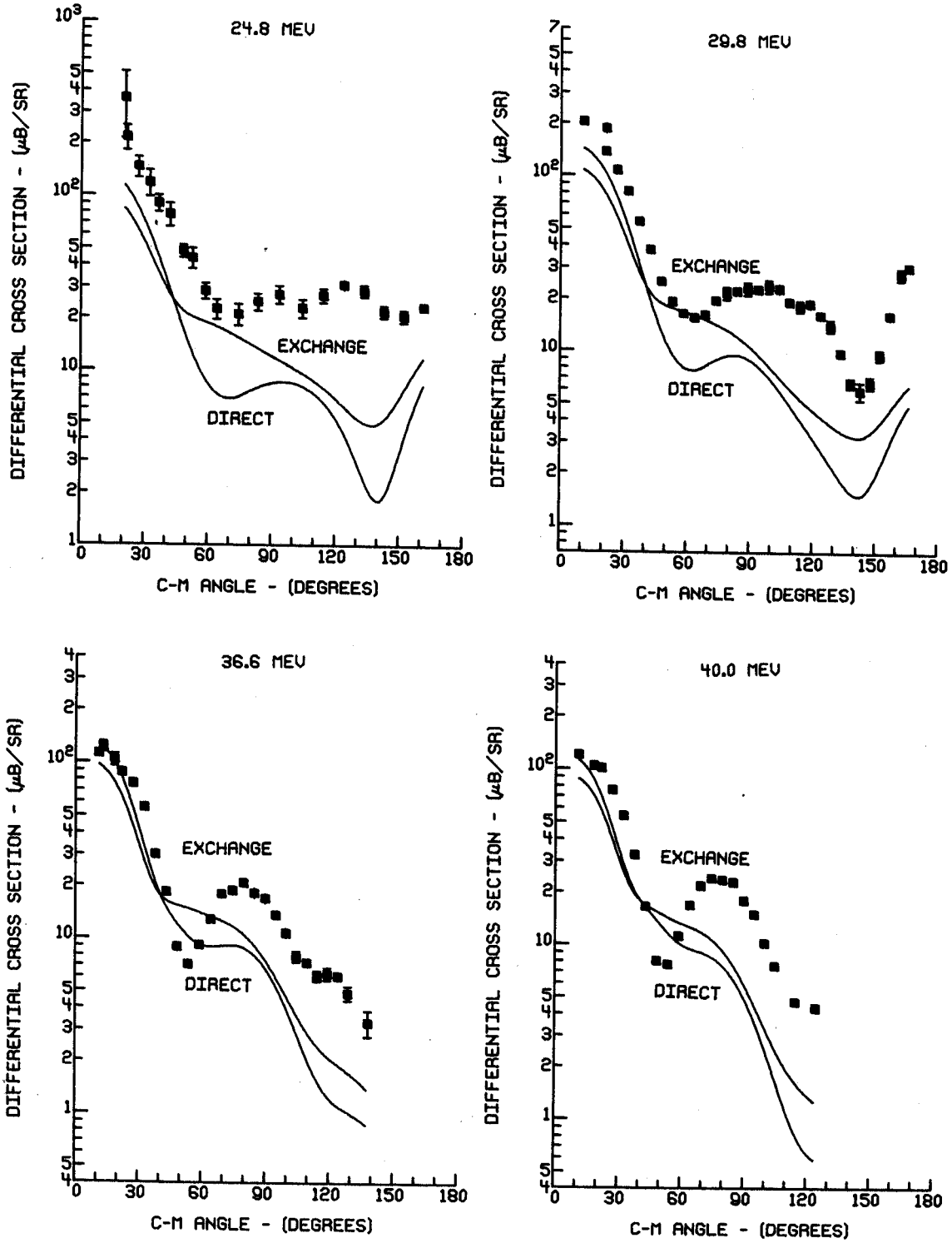

FIGURE 44. $^{14}N(p,p')^{14}N^*$ (2.31 MeV) calculations for HJ-G central plus HJ-T.

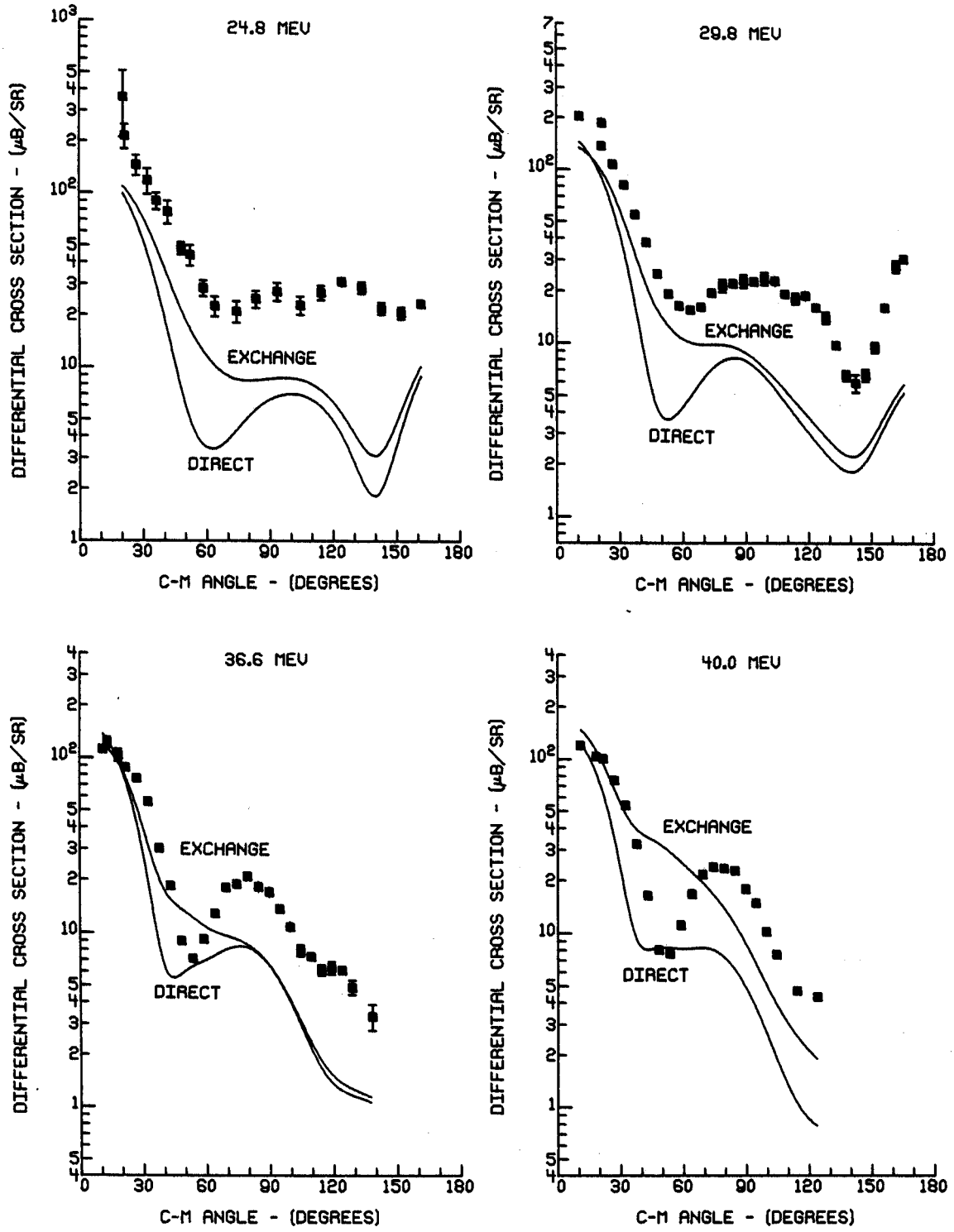

FIGURE 45. $^{14}N(p,p')^{14}N^*$ (2.31 MeV) calculations for BJ central plus OPEP.

The results for the central potential taken from the survey by Sam Austin (SMA) plus OPEP are shown in Figure (46). The 1.0 F range SMA central force yields a total cross section for the 29.8 MeV inelastic scattering to the 2.31 state of 0.536 mb. This is slightly stronger than the H-J central potential, and it fits the data about as well as the H-J potentials.

The conclusion that these results lead to is that the best central force to use should be relatively weak in strength and long in range (see Table 34). Of the central forces tried here, the weakest and longest range force that still was derived from a realistic force, was the Serber central force (S) with V_{11} strength 3.47 MeV and range 1.415 F. The results of the calculations with S + OPEP are found in Figure (47). This central force plus OPEP probably best reproduced the shape of the data at the four energies considered. The S central interaction seems like the best central force to use in drawing conclusions about the strength of the tensor force.

When the 0.49 cutoff radius Hamada-Johnston spin-orbit potential was added to S + OPEP, the total cross sections decreased by about 25% and changed somewhat in shape. See Figure (48). Since it was felt that this was a good estimate of the spin-orbit potential, it was decided to include this potential when extracting the strength of the tensor force.

The force of J-L Escudie *et al*. produced the results

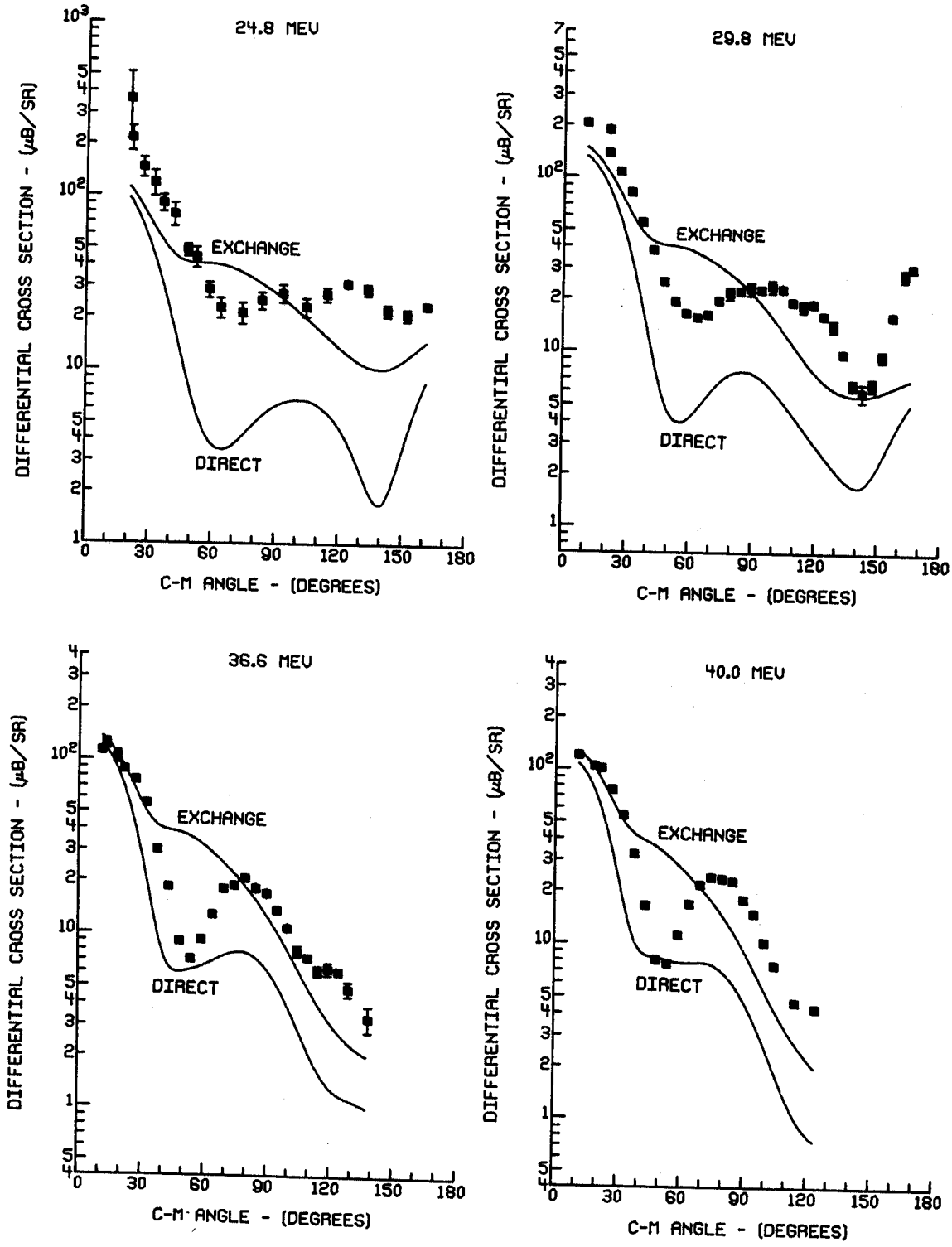

FIGURE 46. $^{14}N(p,p')^{14}N^*$ (2.31 MeV) calculations for SMA central plus OPEP.

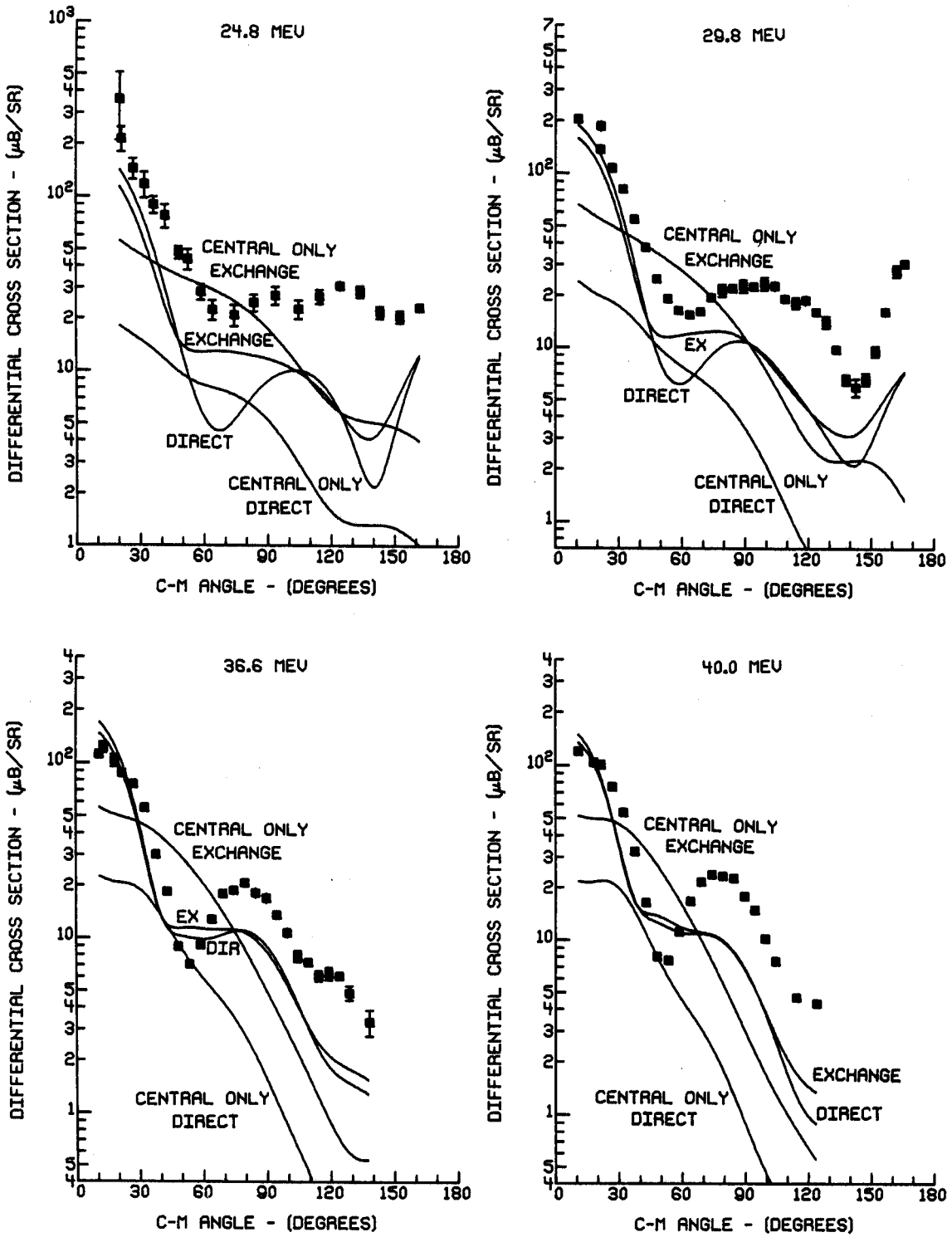

FIGURE 47. $^{14}N(p,p')^{14}N^*$ (2.31 MeV) calculations for S central plus OPEP and S central alone.

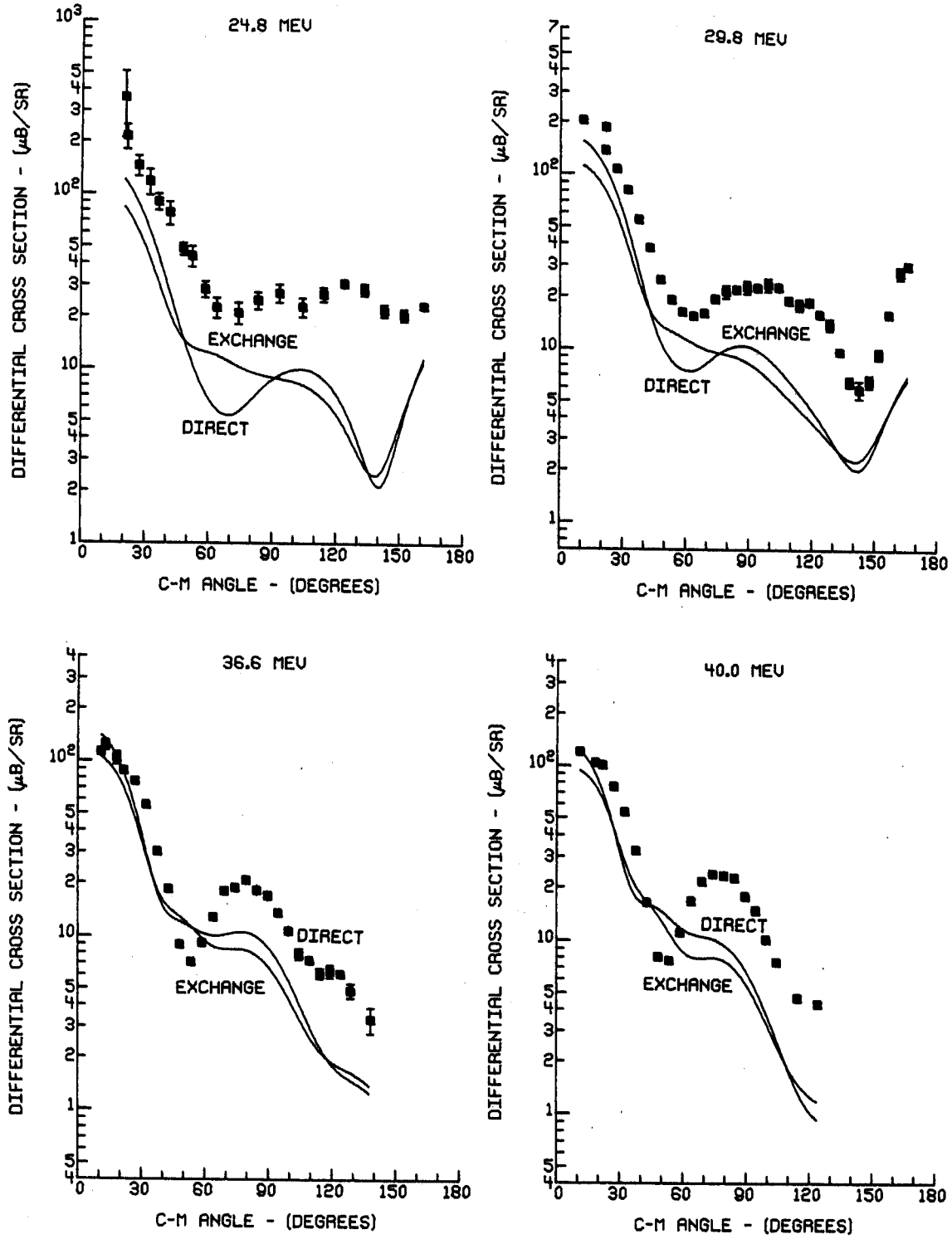

FIGURE 48. $^{14}N(p,p')^{14}N^*$ (2.31 MeV) calculations for S central plus HJ-LS and OPEP.

in Figure (49). The shape is reasonable for lower energies but deteriorates rapidly as one goes to higher energies.

There is also evidence that other than direct processes are contributing to the 24.8 MeV angular distribution at backward angles. Central plus tensor forces that reproduce the dip at about 140° C. M. in the 29.8 MeV data also predict a dip for the 24.8 MeV cross section. There is no dip in the data. See Figure (47) for example.

After it was established that the best essentially apriori fit to the 2.31 MeV state data is obtained with the Serber central force plus OPEP and the Hamada-Johnston spin-orbit potential (r_c = 0.49 F), calculations were made in which the strength of OPEP was varied to see what ratio of central strength to OPEP strength would best reproduce the shape of the experimental data. The results for the Serber central plus the Hamada-Johnston spin-orbit plus OPEP; OPEP with a 25% increase in strength (1.25 x OPEP); and OPEP with a 40% increase in strength (1.4 x OPEP) are found in Figures 50, 51, and 52. These calculations were scaled to best fit the data, with emphasis on the foreward angle data. The scale factors are found in Table (35). Of the three tensor forces used, the 1.25 x OPEP force best fits the data overall. At 24.8 and 29.8 MeV the calculations with 1.25 x OPEP are a definite improvement over those with OPEP. The distinction is not so clear at 36.6 and 40.0 MeV, but the calculations

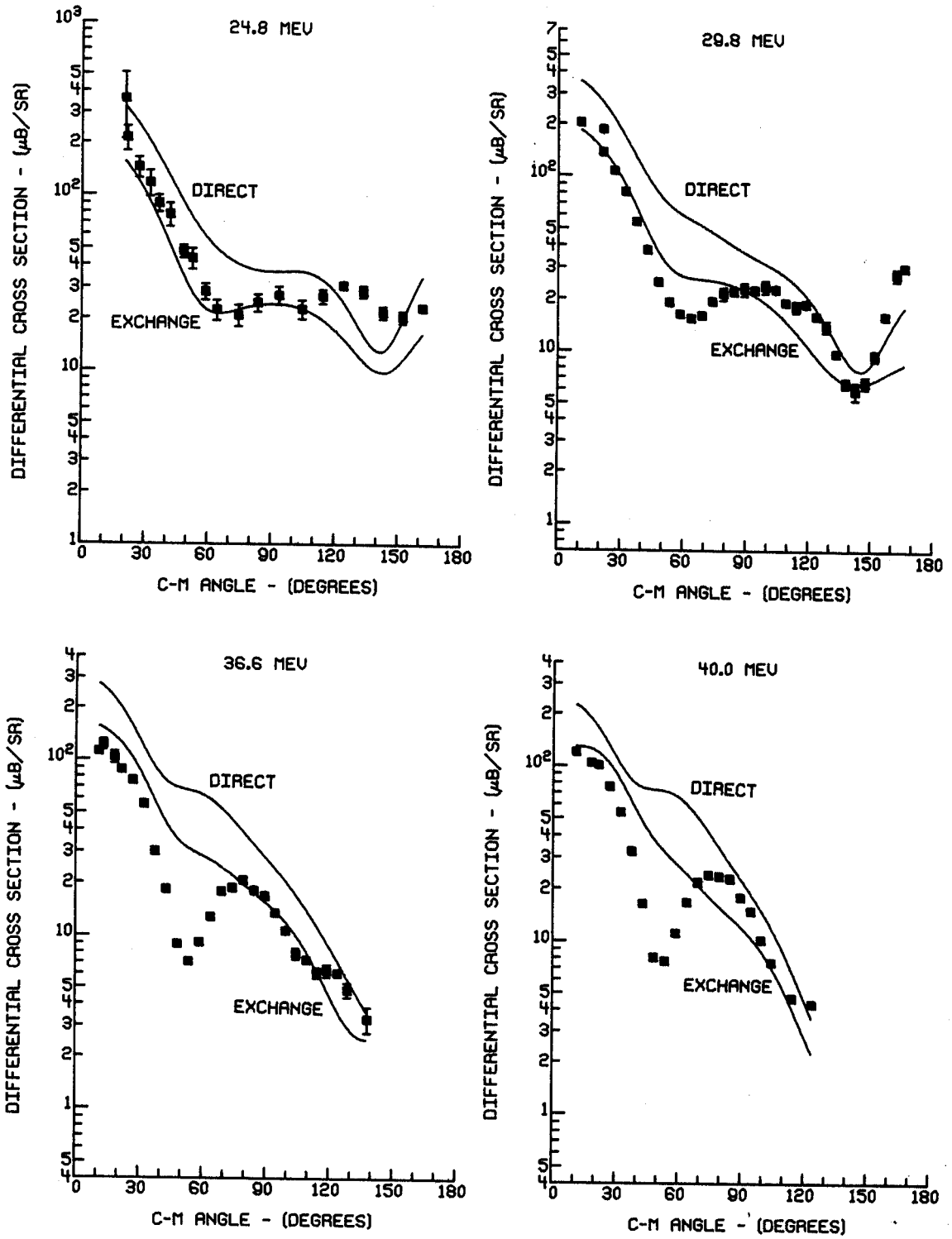

FIGURE 49. $^{14}N(p,p')^{14}N^*$ (2.31 MeV) calculations for the complete Hamada-Johnston potential as put into Yukawa form by Escudie et al. (Es 72).

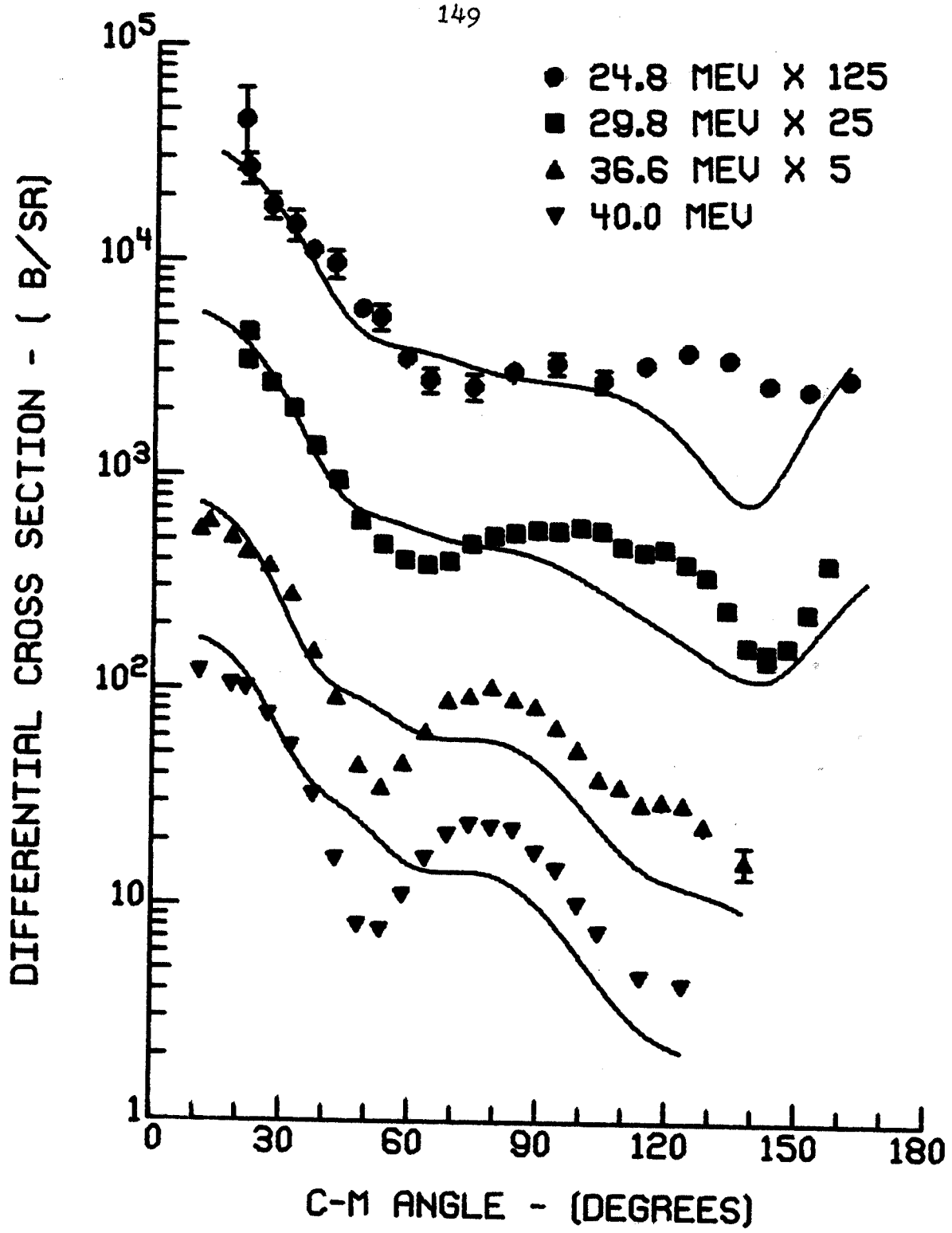

FIGURE 50. $^{14}N(p,p')^{14}N^*$ (2.31 MeV) calculations for S central plus HJ-LS plus OPEP. Calculations are normalized to best fit the data at forward angles.

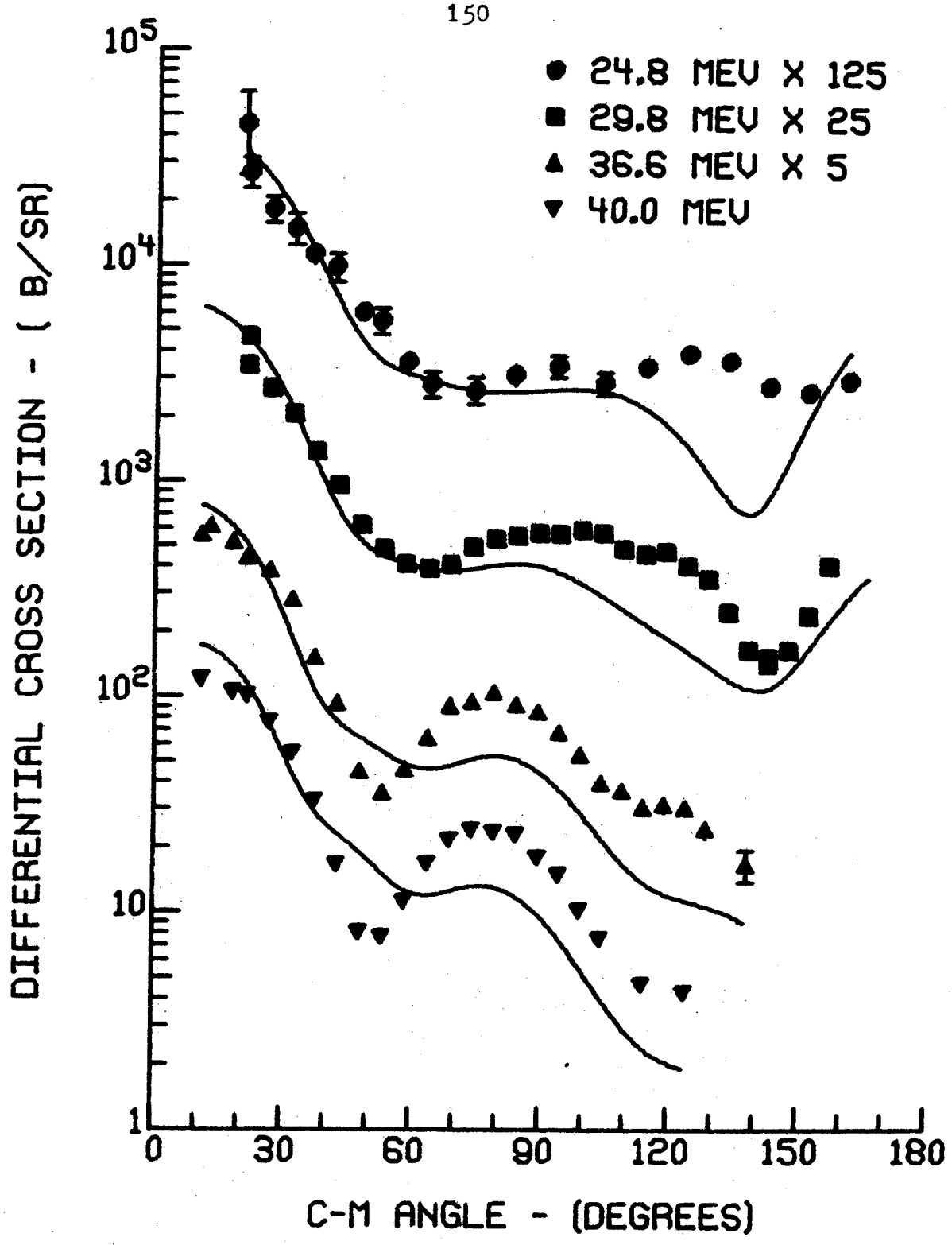

FIGURE 51. $^{14}N(p,p')^{14}N^*$ (2.31 MeV) calculations for S central plus HJ-LS and 1.25 x OPEP. Calculations are normalized to best fit the data at forward angles.

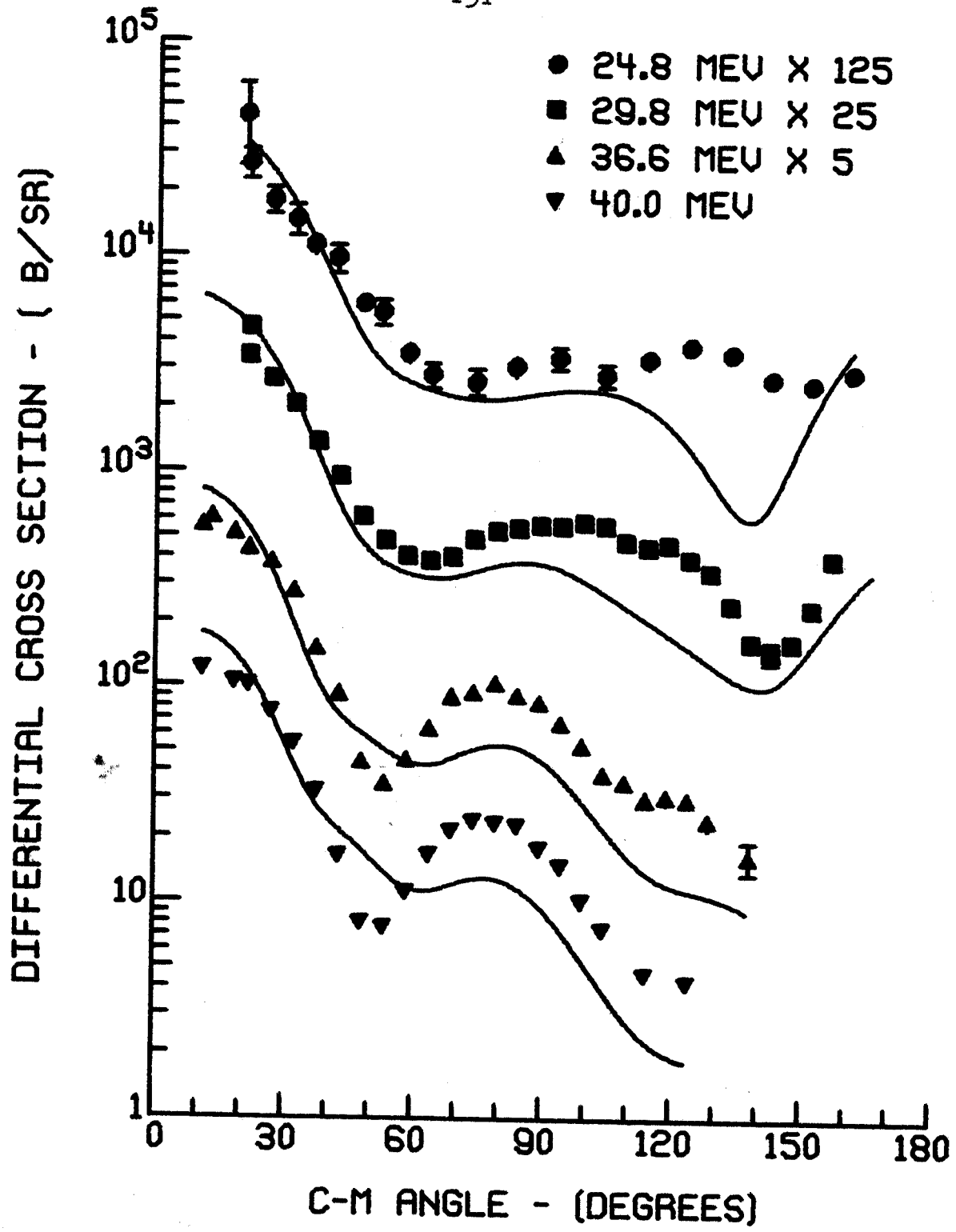

FIGURE 52. $^{14}N(p,p')^{14}N^*$ (2.31 MeV) calculations for S central plus HJ-LS and 1.4 x OPEP. Calculations are normalized to best fit the data at forward angles.

TABLE 35. Calculation normalization factors.

Interaction	Proton Energy (MeV)	Normalization Factor
S + L : S (HJ; r_c = 0.49 F) + OPEP	24.8	2.5
	29.8	2.0
	36.6	1.4
	40.0	1.8
S + L : S (HJ; r_c = 0.49 F) + 1.25 x OPEP	24.8	1.95
	29.8	1.40
	36.6	0.93
	40.0	1.18
S + L : S (HJ; r_c = 0.49 F) + 1.4 x OPEP	24.8	1.50
	29.8	1.12
	36.6	0.88
	40.0	0.95

With 1.25 x OPEP fit the data over a slightly larger range of forward angles than do those with OPEP. There is almost no difference between 1.25 x OPEP and 1.4 x OPEP for the 36.6 and 40.0 MeV data and at 24.8 and 29.8 MeV, 1.25 x OPEP yields slightly better fits than does 1.4 x OPEP. The 1.4 x OPEP calculations overstate the forward angle drop of the experimental angular distributions at 24.8 and 29.8 MeV.

Comparison of the 24 MeV, $^{14}N(p,p')^{14}N^*$ (2.31 MeV) asymmetry data of Escudie et al. (es 70) with our calculations for 24.8 MeV incident protons indicates better agreement when the spin-orbit force is included.

6.2 Results for Calculations of Inelastic Scattering to States Other than the 2.31 MeV State

Of the measured inelastic scattering angular distributions to the other states in ^{14}N only those to the 3.94 and 7.03 MeV states are expected to be properly described by Cohen and Kurath wavefunctions and consequently only these were analyzed in any detail. For both of these cases, the calculated total cross sections for $\vec{J} = 2$ dominate those for the other possible $\vec{J}$ transfers. It is expected that these transitions are mainly S = 0, L = 2 and so the calculated cross sections were enhanced by a factor equal to the ratio of the experimental E2 reduced transition probability to the reduced transition probability calculated with Cohen-Kurath wave functions. The experimental E2

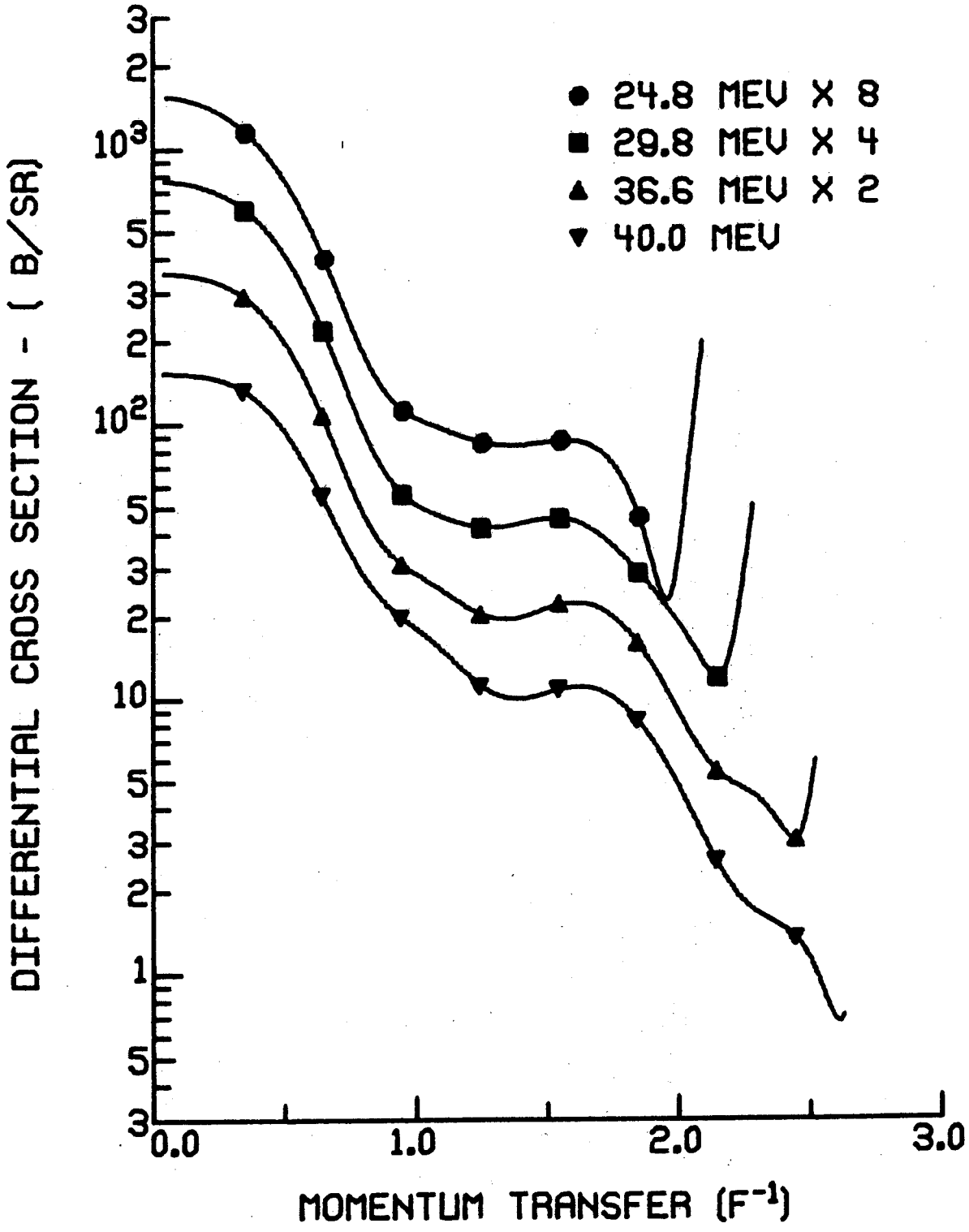

FIGURE 53. $^{14}N(p,p')^{14}N^*$ (2.31 MeV) calculations for S central plus HJ-LS and OPEP plotted as a function of momentum transfer. The symbols are for identification only.

reduced transition probability for the 3.94 to g.s. transition was taken to be 9.0 ± 0.6 e^2F^4 (Ol 67) and for the 7.03 to g.s. transition, 3.4 ± 0.9 e^2F^4 (Ol 67). The respective calculated reduced transition probabilities were 1.7 and 0.8 e^2F^4. The enhancement ratios were 5.3 and 4.3. The angular distributions were calculated the Serber central interaction (S). For the 3.94 MeV state, the enhanced calculated cross sections are of the correct magnitude. (See Figure 54.) This is not the case for the 7.03 MeV state. (See Figure 55.)

While the remaining inelastic scattering data is yet to be analyzed in detail, it should be pointed out that the calculations with the ^{14}N wave functions of True (Tr 63) and those with ^{14}N wave functions from the work of Reehal et al. (Re 72) produce the same results.

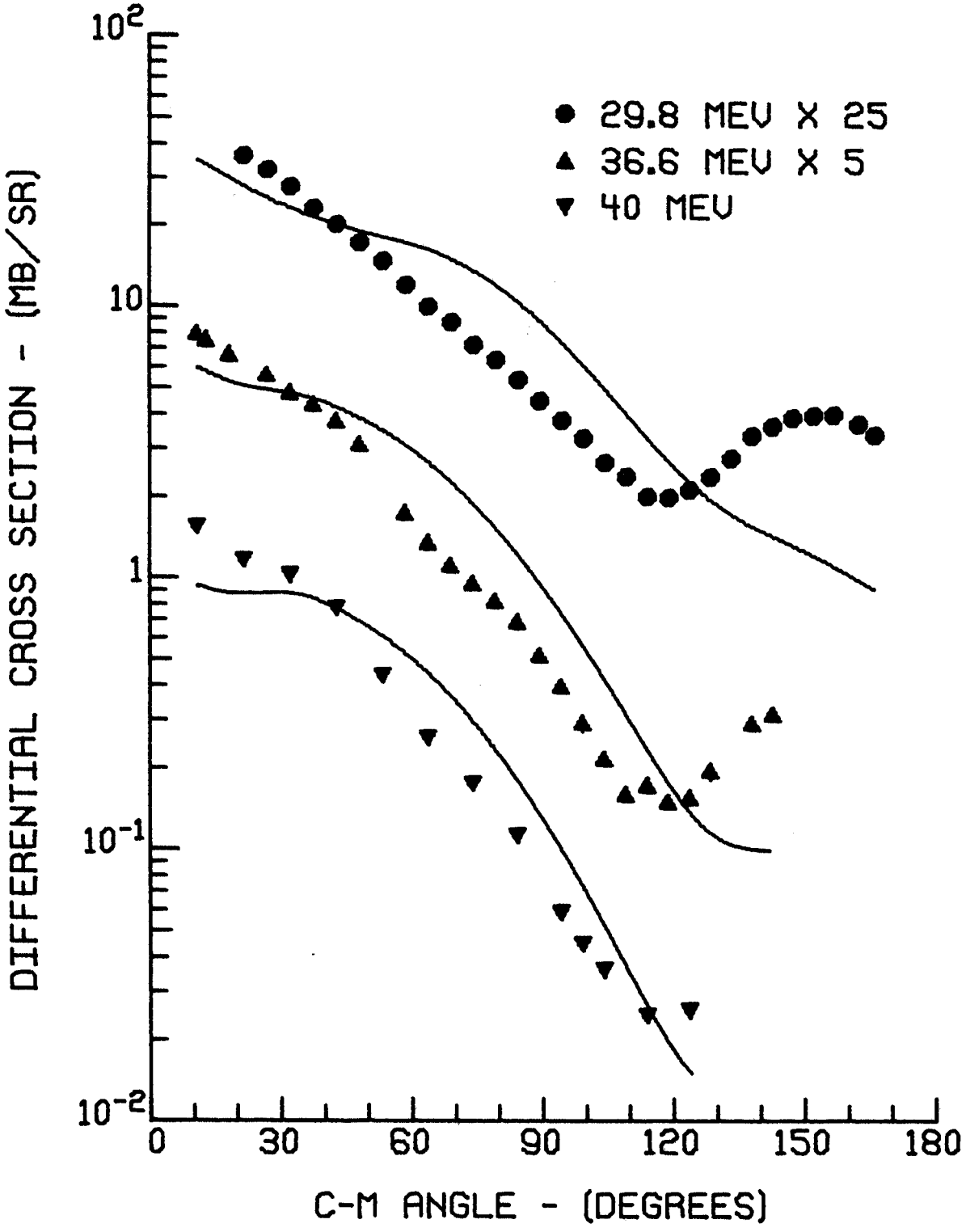

Figure 54. $^{14}N(p,p')^{14}N^*$ (3.94 MeV) calculations for S central and C-K wave functions normalized by the experimental to calculated E2 transition ratio.

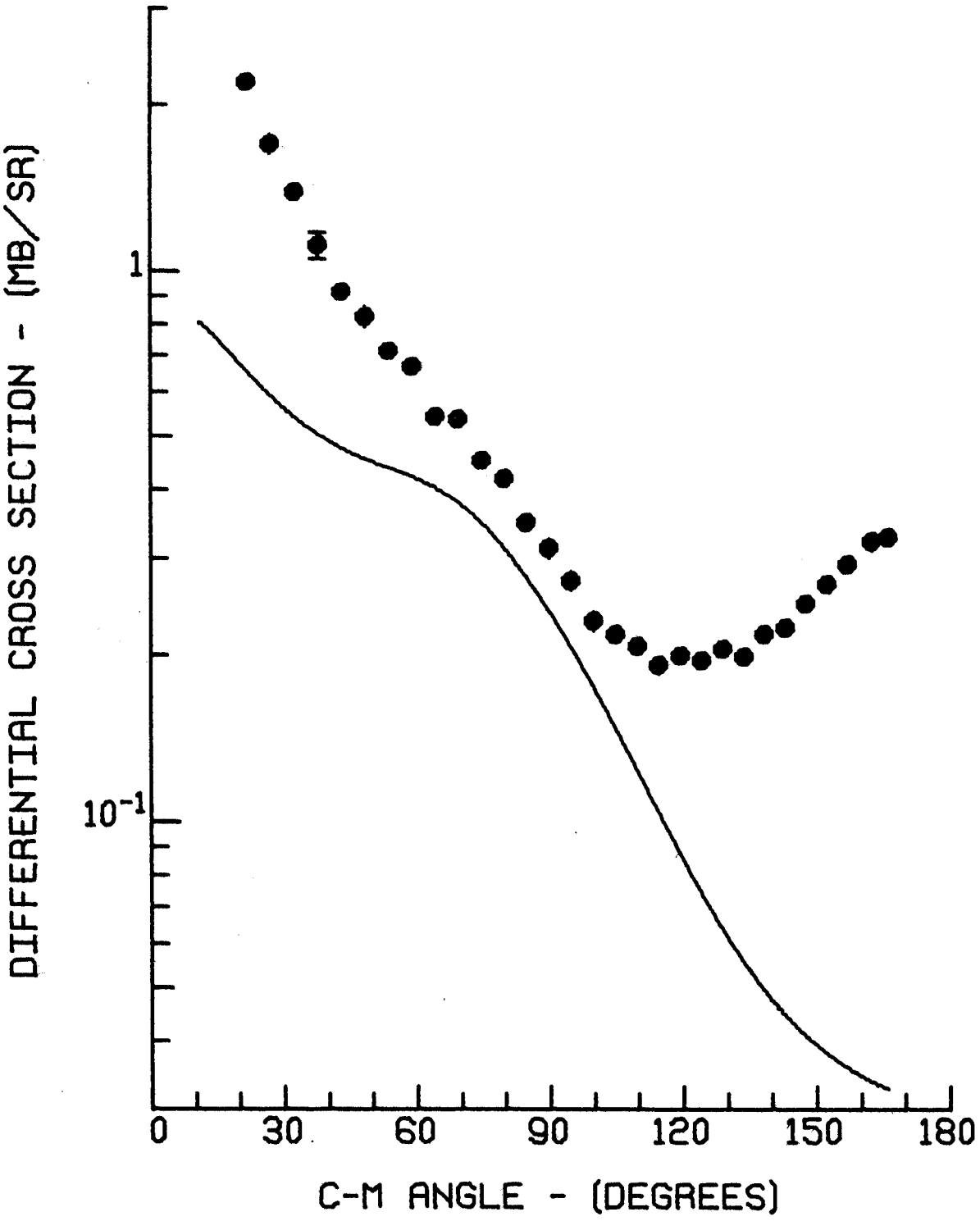

Figure 55. $^{14}N(p,p')^{14}N^*$ (7.03 MeV) calculations for S central and C-K wave functions normalized by the experimental to calculated E2 transition ratio.

7. CONCLUSIONS

The interaction that best fits the shape of the inelastic scattering to the 2.31 MeV state in ^{14}N at 24.8, 29.8, 36.6, and 40.0 MeV was a Serber central interaction plus the Hamada-Johnston spin-orbit potential (r_c = 0.49 F) and OPEP with a 25% increase in strength. The overall normalization factors for the calculated angular distributions with this force are found in Table (35). The J_4 integrals of the tensor potentials implied by these results are found in Table (36) along with other estimates of the strength of the tensor force as compiled by Sam Austin (Au 72). The tensor strength obtained by this analysis of inelastic scattering to the 2.31 MeV state in ^{14}N (probably the most complete to date) seems to be greater than that of earlier works. One must keep in mind that the spin-orbit potential was included in this analysis, but not in the other results in Table (36). Inclusion of the Hamada-Johnston spin-orbit potential resulted in a 25% reduction in the calculated total cross section and a 12% increase in the required tensor strength. The results of this work also included the effects of exchange. It is not clear how exchange effects the strength of the extracted tensor force. In calculations made for this work with OPEP alone, the direct calculated total cross sections were about 25% greater than those with exchange. On the

TABLE 36. Values of the tensor force.

Determination	$V_{T\lambda}$ (MeV)	α (F^{-1})	β(F^{-1})	J_4 (MeV-F^5)
^{14}N (p,p') ^{14}N (a)				
(2.31 MeV, 0^+, 1)				
E_p = 24.8	6.56	1.23	—	555*
29.8	5.70	1.23	—	470*
36.0	4.70	1.23	—	397*
40.0	5.35	1.23	—	454*
^{14}C (p, n) ^{14}N (g.s) (b)				
E_p = 10.4 MeV	5.4	0.707	4.0	444
12.7	5.1	0.707	4.0	420
13.3	5.1	0.707	4.0	420
18.3	3.9	0.707	4.0	321
^{12}C (p,p') ^{12}C				
(15.1 MeV, 1^+, 1) (c)				
E_p = 45.5	2.35	0.707	—	200*
^{14}N (p,p') ^{14}N				
(2.31 MeV, 0^+, 1) (d)				
E_p = 24.8 MeV	3.9	0.707	2.0	290
29.8	14.6	1.23	—	421*

TABLE 36 (con't.)

$1p$ - shell, two body [e] matrix elements	5.1	0.707	4.0	420
OPEP				318
HJ[f] (r_C = 1.0 F)				288
(r_C = 0.6 F)				294
(r_C = 0.49 F)				295

a) Present work; only the present work includes the spin-orbit potential. Results including exchange are marked (*).

b) Reference Wo 71: uses ROPEP form:

$$V_T(r) = (V_m + V_{T\lambda}\vec{\lambda}_1 \cdot \vec{\lambda}_2) S_{12} \left[f(\alpha) - \frac{\beta^3}{\alpha^3} f(\beta)\right]$$

where $f(\alpha) = 1 + \frac{3}{\alpha r} + \frac{3}{(\alpha r)^2}) \frac{e^{-\alpha r}}{\alpha r}$

c) Reference Lo 70c. OPEP form.

d) 24.8 MeV: Reference Cr 70, ROPEP form.
29.8 MeV: Reference Fo 71, r^2 - Y form.

e) Reference Sc 68, determined by Schmittroth from Cohen-Kurath $1p$-shell two body matrix elements involving the 1^+, T=0 and 0^+, T=1 states only.

f) Reference Sc 71. For the part of the Hamada-Johnston potential with $r \geq r_C$.

other hand, for central force calculations the exchange total cross sections were greater that the direct. For Serber central potential plus OPEP, the direct total cross section was larger than that with exchange.

It is not clear that the results of the present analysis can be directly compared to the earlier works listed in Table (36). The ^{14}C (p,n) ^{14}N (gs) works were at proton energies for which compound nuclear effects can be important. Evidence for other than direct effects in the 24.8 MeV data has already been discussed (Section 6.1). The ^{14}N (p,p') analysis of Reference Cr 70 at 24.8 MeV used a tensor force quite different in form from OPEP.

It might be pointed out that there is something of a trend toward decreasing tensor strength with increasing proton energy in the results of this analysis. It is most clear for E_p = 24.8 and 29.8 MeV where the fits to the data were more conclusive than at 36.6 and 40.0 MeV.

8. SUMMARY

The work of extracting the strength of the tensor force from calculations of inelastic scattering of protons from the 2.31 MeV state of ^{14}N is not complete. While this is the most complete analysis to date, the fits to the data, especially at 36.6 and 40.0 MeV are not as good as one would like. The fact that OPEP alone seems to reproduce the shapes of the angular distributions better than the complete force, indicates that perhaps the wave functions are not reproducing completely enough the cancellation of the L = 0 central amplitudes. Because of the small cross section, two step processes may be very important. P. D. Kunz is now making calculations that may clear up this point. It is possible that contributions from the interior of the nucleus are too large since we did not take into account the non-locality of the Optical Model Potential, or possible density dependence of the effective force. Damping of the contributions from the nuclear interior have been shown to improve distorted wave fits to (p, d) reactions in this mass region (Pr 70).

LIST OF REFERENCES

REFERENCES

At 70. J. Atkinson and V. A. Madsen, Phys. Rev. C1 (1970) 1377.

Au 70. R. Au and D. Bayer, unpublished.

Au 72. S. M. Austin, The Two Body Force in Nuclei, Plenium Publishing Corporation, New York, (1972) 285.

Ba 66. J. N. Bahcall, Nucl. Phys. 75 (1966) 10.

Ba 71. D. L. Bayer, MSUCL-34, Michigan State University Cyclotron Laboratory (1971).

Ba 71a. D. L. Bayer, MSUCL-34, Michigan State University Cyclotron Laboratory (1971).

Ca 70. T. A. Cahill, F. P. Brady, S. Corbett, W. Hammontree, K. Isaacs and E. Young, Nucl. Instr. and Meth. 87 (1970) 151.

Co 65. S. Cohen and D. Kurath, Nucl. Phys. 73 (1965) 1.

Cr 70. G. M. Crawley, S. M. Austin, W. Benenson, V.A. Madsen, F. A. Schmittroth and M. J. Stomp. Phys. Lett. 32B (1970) 92.

Cr 70a. G. M. Crawley, private communication.

Da 69. Guide to the Selection and Use of Position Sensitive Detectors, Nuclear Diodes, ed. by W. W. Daehnick (1969).

En 67. H. A. Enge and J. E. Spencer, Split Pole Magnetic Spectrograph for Precision Nuclear Spectroscopy, Nucl. Inst. and Meth. 49 (1967) 181.

Es 72. J.-L. Escudie, F. G. Resmini and Y. Jerrien, private communication and Birmingham Conf. April 1972.

Es 70. J.-L. Escudie, A. Farrats and J. Raynal, Polarization Phenomena in Nuclear Reactions (University of Wisconsin Press, Madison, 1970) 705.

Fo 71. S. H. Fox, S. M. Austin, and D. Larson, B.A.P.S. 16 (1971) 1163.

Fr 69. F. B. French, E. C. Halbert, J. B. McGrory and S. S. M. Wong, Advances in Nuclear Physics, Vol III eds. M. Baranger and E. Vogt (Plenum Press, New York, 1969).

Go 59. T. J. Gooding, Nucl. Phys. 12 (1959) 241.

Gr 68. G. W. Greenlees, G. J. Pyle, and Y. C. Tang, Phys. Rev. 171 (1968) 1115.

Ha 62. T. Hamada and L. D. Johnston, Nucl. Phys. 34 (1962) 382.

Ki 64. C. C. Kim, S. M. Bunch, D. W. Devins and H. H. Forster, Nucl. Phys. 58 (1964) 32.

La 71. H. W. Laumer, Ph.D. Thesis, M.S.U. (1971) 22.

Lo 71. W. G. Love, Phys. Lett. 35B (1971) 371.

Lo 70. See for example W. G. Love and G. R. Satchler, Nucl. Phys. A159 (1970) 1.

Lo 70a. W. G. Love, L. J. Parish and A. Rickter, Phys. Lett. 31B (1970) 167.

Lo 70b. W. G. Love and G. R. Satchler, Nucl. Phys. A159 (1970) 1.

Lo 70c. W. G. Love and L. J. Parish, Nucl. Phys. A157 (1970) 625.

Ma 67. G. H. MacKenzie, E. Kashy, M. M. Gordon and H. G. Blasser, IEEE Transactions on Nuclear Science, NS-14 3 (1967) 353.

Ma 71. V. A. Madsen, private communication.

Ma 66. V. A. Madsen, Nucl. Phys. 80 (1966) 177.

Ma 64. M. Q. Makino, C. N. Waddell and R. M. Eisberg, Nucl. Phys. 50 (1964) 145.

Ma 68. See for example N. F. Mangelson, B. G. Harvey and N. K. Glendenning, Nucl. Phys. A117 (1968) 161.

Ma 68. N. F. Mangelson, B. G. Harvey and N. K. Glendenning, Nucl. Phys. A117 (1968) 161.

Mi 54. E. A. Milne, Phys. Rev. 93 (1954) 762.

Oe 69. W. T. H. van Oers and J. M. Cameron, Phys. Rev. 184 (1969) 1061.

Ol 67. J.W. Olness, A.R. Poletti, E.K. Warburton, Phys. Rev. 154 (1967) 971.

Ow 70. L. W. Owen and G. R. Satchler, Phys. Rev. Lett. 25 (1970) 1720.

Pr 70. B. M. Preedom, J. L. Snelgrove, E. Kashy, Phys. Rev. C1 (1970) 1132.

Pe 63. F. G. Perey, Phys. Rev. 131 (1963) 745.

Pi 70. W. L. Pickles, Ph.D. Thesis, M.S.U. (1970) 25.

Pi 70a. W. L. Pickles, Ph.D. Thesis, M.S.U. (1970) 34.

Pi 70b. W. L. Pickles, Ph.D. Thesis, M.S.U. (1970) 44.

Pi 70c. W. L. Pickles, Ph.D. Thesis, M.S.U. (1970) 14.

Re 72. B. S. Reehal, G. H. Wildenthal and J. B. McGrory, to be published.

Ro 71. C. W. Rogers, Ph.D. Thesis, Oregon State University (1971).

Ro 68. H. J. Rose, O. Hausser and E. K. Warburton, Rev. Mod. Phys. 40 (1968) 591.

Ro 69. SAMPO J. T. Routi and S. G. Prussin, Nucl. Instr. and Meth. 72 (1969) 125.

Sa 70. H. S. Sandhu, Nucl. Phys. A146 (1970) 163.

Sa 66. See for example G. R. Satchler, Nucl. Phys. 77 (1966) 481.

Sc 71. R. Schaeffer and S. M. Austin, private communications.

Sc 70. R. Schaeffer and J. Raynal, unpublished.

Sc 68. F. A. Schmittroth, Ph.D. Thesis, Oregon State University (1968).

Se 52. J. D. Seagrave, Phys. Rev. 85 (1952) 197.

Si 59. E. A. Silverstein, Nucl. Inst. and Meth. 4 (1959) 53.

Sn 69. J. L. Snelgrove and E. Kashy, Phys. Rev. 187 (1969) 1259.

Sn 67. J. L. Snelgrove and E. Kashy, Nucl. Instr. and Meth. 52 (1967) 153.

Ta 65. T. Tamura, Rev. Mod. Phys, 37 (1965) 679.

Th 67. K. M. Thomson, C. R. Gruhn and J. Frink, Phys. Lett. 24B (1967) 503.

Tr 70. G. F. Trentelman and E. Kashy, Nucl. Instr. and Meth. 82 (1970) 304.

Tr 70a. G. F. Trentelman, Ph.D. Thesis, M.S.U. (1970) 17.

Tr 63. W. W. True, Phys. Rev. 130 (1963) 1530.

Vi 57. W. M. Visscher and R. A. Ferrell, Phys. Rev. 107 (1957) 781.

Wa 69. B. A. Watson, P. P. Singh and R. E. Segel, Phys. Rev. 182 (1969) 977.

Wo 71. C. Wong, J. D. Anderson, V. A. Madsen, F. A. Schmittroth and M. J. Stomp, Phys. Rev. C3 (1971) 1094.

Wo 67. C. Wong, J. D. Anderson, J. McClure, B. Pohl, V. A. Madsen and F. A. Schmittroth, Phys. Rev. 160 (1967) 769.

Wo 53. H. H. Woodbury, R. B. Day and A. V. Tollestrup, Phys. Rev. 92 (1953) 1199.

APPENDICES

A1. GAS TARGET GEOMETRICAL CONSIDERATIONS

A1.1 G-Factor Estimation

As stated in the text the G factor that appears in the expression for the differential cross section is just the integral of the solid angle from any point along the beam over the length of the beam that the slits define as the target. If one assumes that the cross section is flat, that the back aperture is a rectangle, that the front and back slits are of equal width, that the difference between θ, θ', and θ'' in Figure(3) can be neglected, and that the distance between some point along the line source and some point on the back aperture does not change with the height of that point on the back aperture, the integration is simple and results in the following formula for G.

$$G = \frac{C^2 h}{ba}$$

where C = the front and back slit widths

b = the distance between the front and back slits

a = the distance of the back slit from the center of the gas cell

h = the height of the rear aperture

For $\frac{d\sigma}{d\theta}$ and $\frac{d^2\sigma}{d\theta^2}$ set to zero, for slits meeting the

conditions above, and for $\theta = 90°$ agreement between the program G-FACTOR and the above formula was good to 3%.

A1.2 Kinematic Broadening Estimate

The analysis that leads to the full-width at half maximum (f.w.h.m.) of detected peaks first due to kinematic broadening and the acceptance angle of the slit system is most straight forward at $\theta = 90°$. Since kinematic broadening is near its maximum at this angle, this estimate is quite useful. It is carried out here only for telescopes with front and back slits of equal width. Figure (A1) shows the geometry involved. The height of the peak due to particles scattered at $\theta_L = 90°$ will be proportional to the length C. Particles scattered at slightly larger or smaller angles than 90° and allowed by the slits to be detected must come from slightly shorter lengths of bombarded gas. The angles that correspond to particles from lengths of gas C/2 will correspond to the half height points of the peak. The dashed lines in Figure (A1) represent this situation and from this figure it is easy to see that the $\Delta\theta$ corresponding to the half heighth of the peak on one side is arc $\tan \frac{C}{2b}$. The angle corresponding to the energy spread between the two half height points is just $2\Delta\theta$ or 2arc $\tan \frac{C}{2b} \approx \frac{C}{b}$.

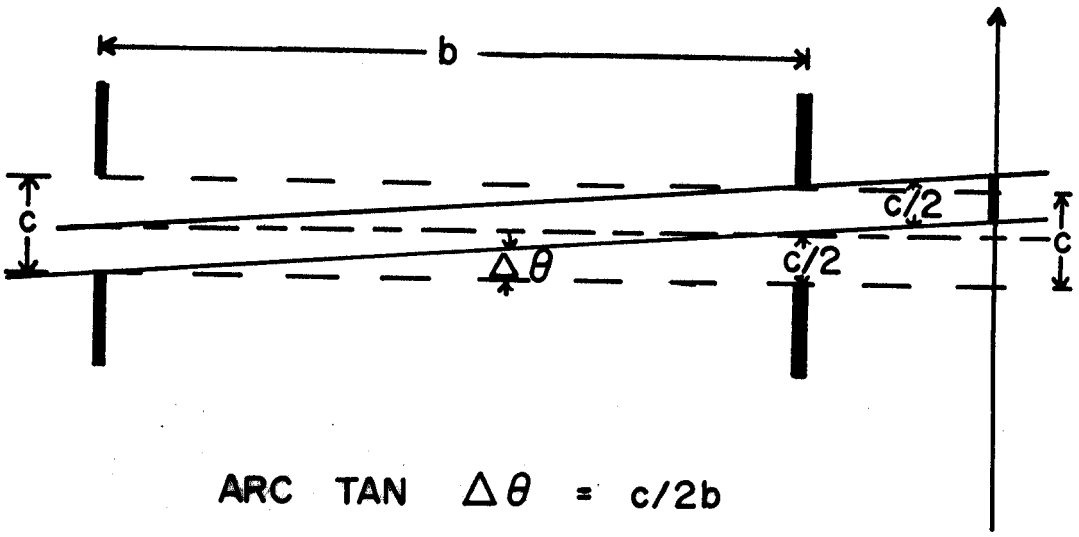

FIGURE A1. Collimation slits defining the line source at 90° in the Lab.

A2. TRANSFORMATIONS OF NUCLEAR FORCES FROM ODD-EVEN, SINGLET-TRIPLET FACTORIZATION TO SPIN, ISO-SPIN AND NEUTRON-PROTON FACTORIZATIONS

A central nuclear interaction expanded in terms of the total spin state (singlet S or triplet T) of the two-nucleon system and its relative angular momentum [even (E) or odd (O)] can be expressed in terms of exchange and spin dependence by means of the transformation below.

$$t_{(S=0,\ T=0)} = \frac{1}{16}\,(3\,t_{SE} + 3\,t_{TE} + t_{SO} + 9\,t_{TO})$$

$$t_{(S=0,\ T=1)} = \frac{1}{16}\,(t_{SE} - 3\,t_{TE} - t_{SO} + 3\,t_{TO})$$

$$t_{(S=1,\ T=0)} = \frac{1}{16}\,(-3\,t_{SE} + t_{TE} - t_{SO} + 3\,t_{TO})$$

$$t_{(S=1,\ T=1)} = \frac{1}{16}\,(-t_{SE} - t_{TE} + t_{SO} + t_{TO})$$

DWBA 70 uses neutron-proton representation for the nuclear force. The corresponding combinations of the t_{ST}'s for this representation are

$$t_{pp}(S=0) = t_{nn}(S=0) = t_{00} + t_{01}$$

$$t_{pp}(S=1) = t_{nn}(S=1) = t_{10} + t_{11}$$

$$t_{pn}(S=0) = t_{00} - t_{01}$$

$$t_{pn}(S=1) = t_{10} - t_{11}$$

The tensor and spin-orbit potential act only in triplet or S = 1 states. Thus there are only triplet odd